Università degli Studi di Padova

Sede amministrativa: Padova
Dipartimento di Fisica "G. Galilei"

Scuola di Dottorato di Ricerca
in Fisica

Ciclo XXIV

Tesi di Dottorato:

Measurement of the Inclusive Cross Section $\sigma(pp \to b\bar{b}X \to \mu\mu\mathbf{X}')$ at $\sqrt{s} = 7$ TeV with the CMS Experiment at the LHC

Direttore della Scuola

prof. Andrea Vitturi

Supervisore

prof. Franco Simonetto

Co-Supervisori

dott. Tommaso Dorigo
dott. Martino Margoni

Dottorando

Luca Perrozzi

"There are known knowns;
there are things we know we know.
We also know there are known unknowns;
that is to say we know there are some things we do not know.
But there are also unknown unknowns
- there are things we do not know we don't know. [...]
So when we do the best we can and we pull all this information together,
and we then say well that's basically what we see as the situation,
that is really only the known knowns and the known unknowns.
And each year, we discover a few more of those unknown unknowns. [...]
There's another way to phrase that
and is that the absence of evidence is not evidence of absence."

D. Rumsfeld, US Secretary of Defence,
to justify Iraq invasion.

"The main dangers lie in the unknown knowns."

S. Žižek, Psychoanalytic philosopher,
to remember Rumsfeld the Abu Ghraib scandals.

"The LHC should, though, if all goes according to plan,
show up one very well known unknown by creating tiny black holes.
These will not, as some have suggested, consume the Earth."

The Economist, 19 days before the LHC 2008 accident.
A striking example of unknown unknowns...

Abstract

Beauty quarks are produced with a large cross section at a previously unreached center-of-mass energy at the Large Hadron Collider (LHC), enabling precision measurements to improve our understanding of heavy flavor physics. This thesis presents the measurement of the inclusive cross section $\sigma(pp \to b\bar{b}X \to \mu\mu X')$. Di-muon events are selected in the pseudo-rapidity range $|\eta| < 2.1$, and transverse momentum $p_T > 4$ GeV or $p_T > 6$ GeV. The amount of signal events is determined with a fit to the di-muon transverse impact parameter distribution. The analysis is applied to data recorded by the CMS detector during proton-proton collisions at $\sqrt{s} = 7$ TeV centre-of-mass energies in the second half of year 2010, corresponding to an integrated luminosity of $\mathcal{L} = 27.9$ pb. The b-quark production cross section is determined and compared to leading-order and next-to-leading-order QCD predictions.

Abstract

Nel collisore adronico LHC i quark beauty sono prodotti con un'elevata sezione d'urto ad una energia nel centro di massa mai raggiunta finora, consentendo misure di precisione in grado di migliorare la nostra comprensione della fisica del sapore. Il presente lavoro di tesi riporta uno studio della misura della produzione inclusiva dei quark b tramite il processo ($pp \to b\bar{b}X \to \mu\mu X'$). Eventi di di-muoni sono selezionati nell'intervallo di pseudo-rapidità $|\eta| < 2.1$ ed impulso trasverso $p_T > 4$ GeV or $p_T > 6$ GeV. La frazione di eventi di segnale e' determinata mediante un'interpolazione della distribuzione di parametro d'impatto trasverso. L'analisi e' applicata ai dati raccolti dal rivelatore CMS durante la fase di presa dati di collisioni ad energia di $\sqrt{s} = 7$ TeV nel centro di massa, avvenuta nella seconda metà del 2010, corrispondenti ad una luminosità integrata di $\mathcal{L} = 27.9$ pb. La sezione d'urto di produzione dei b-quark è misurata e confrontata cno le predizioni QCD al *leading-order* e *next-to-leading-order*.

Contents

Introduction

This thesis presents a study of the production of beauty quarks at the LHC with the CMS experiment. The production of heavy quarks is expected to be accurately described by perturbative QCD. A lot of progress has been made in understanding the b-quark production process [1], so that the measurements are meanwhile in reasonable agreement with the theoretical predictions in most regions of the phase space. Nonetheless, there is a great interest in verifying these results at the higher center-of-mass energy of the LHC, since the theoretical uncertainties are still sizeable. The investigation of events containing beauty quarks probes the predictions of the theory of strong interactions at the energy scale provided by the LHC. Furthermore, the production of b quarks is a major source of background for many searches to be performed at the LHC and therefore needs to be well understood.

Due to the large b-quark production cross section, high statistics data samples are available soon after the LHC startup. This makes the CMS experiment an excellent facility for the study of heavy flavor physics. Even though the CMS detector is primarily designed for high transverse momentum physics, it is very well suited for heavy flavor physics thanks to the muon system capable to identify low transverse momentum muons and the excellent tracking detectors.

A measurement of the beauty quark production cross section based on the semileptonic decay of b quarks into muons is performed in this thesis using the process ($pp \to b\bar{b}X \to \mu\mu X'$). Because of the relatively long lifetime of the b-quark, muons from semileptonic b-decays have larger transverse impact parameter (d_{xy}) than muons from the decay of lighter quarks. The contribution of $b\bar{b}$-events to the measured distribution is determined by performing a fit based on simulated template distributions for signal and background events. The method of discriminating signal from background events by means of d_{xy} has been used for the first time in 1950 by Carlson, Hooper, and King to determine the lifetime of π^0 in cosmic ray showers [2]. Since then it has become a well-established technique for the identification of beauty quarks: the d_{xy} method has been further applied for measuring the b-quark lifetime and production cross section at electron-positron [3, 4, 5], electron-proton [6], and hadron-hadron colliders [7].

The thesis is organized as follows: in the first Chapter an overview of the Standard Model of Particle Physics is given, while a detailed description of the experimental facility at the

LHC and the CMS detector is presented in Chapter 2. The theoretical framework for the physics analysis is introduced in Chapter 3. This includes a review of the main ideas of Quantum Chromodynamics and its application to hadronic collisions, an introduction to the physics of heavy quarks, an overview of the Monte Carlo event generators used in the analysis and considerations on the reliability of the theoretical predictions. Chapter 4 reviews briefly the status of previous inclusive b-quark cross section measurements. Chapter 5 is devoted to the study of the inclusive b-quark production cross section at CMS in the channel $pp \to b\bar{b}X \to \mu\mu X'$, which constitutes the main result of this thesis. It is based on the collision data recorded by the CMS experiment during the first months of high-energy collision data-taking in the second half of year 2010. A detailed study of the main systematic effects of the measurements presented in Chapter 6. Finally, the comparison of the result with theoretical predictions is performed in Chapter 7, while conclusions are outlined in Chapter 8.

Throughout this thesis, natural units are used in which $c = \hbar = 1$.

Chapter 1

Physics at the LHC

This Chapter presents a review of the state-of-the-art in theoretical particle physics, together with some of the open points the LHC has been designed to shed light on. A good awareness of the measurements it is designed to achieve as well as the background environment it is expected to operate within is needed, in fact, to better understand the needs of a challenging experiment such as CMS. Finally, the constraints on the design of the CMS experiment are presented on a qualitative basis, together with a summary of the work presented herein.

1.1 Introduction to the Standard Model

The Standard Model of particle physics (SM) [8, 9, 10, 11, 12, 13, 14] is the theory describing the elementary particles and their interactions. It was conceived after more than 50 years of theoretical works and is based on the fundamental concepts of quantum field theory and on the experimental observations.
Special relativity and quantum mechanics form the basis for quantum field theory and the SM. Particles are represented by relativistic fields obeying to specific propagation equations. Quantitatively a field theory introduces creation and annihilation operators, analogue to quantum mechanical ones, to take into account the possible creation and annihilation of particles.

Using the quantum field theory formalism and both gauge invariance and symmetries, Quantum-Electro-Dynamics (QED) was developed in the 1940s [15]. In 1954 Yang and Mills proposed a "non-Abelian" gauge theory to describe weak interactions [16]. Within this theory, fermions interact by exchanging integer-spin particles called gauge bosons. By combining this theory with the Higgs, Brout and Englert model which let vector bosons acquire mass, Glashow [8], Salam [9], and Weinberg [10] proposed an unified theory for the electro-weak interactions (1967). The gauge bosons for the weak interactions are the Z and $W^{\pm}$ particles, which were discovered at CERN by the UA1 [17, 18] and UA2 [19, 20] experiments.

In 1964, the existence of three quarks (u, d, s) had been proposed. The lack of neutral flavour changing current led to the introduction of a fourth quark (GIM mechanism) [21], the c quark being then discovered in 1974. Discovery of asymptotic freedom (1973) allowed the description of the strong force in terms of a non-Abelian gauge theory, while that of color charge carried by the quark gave birth to the Quantum-Chromo-Dynamics (QCD). Furthermore, CP violation in $K_0 - \bar{K}_0$ oscillation was observed, leading to the hypothesis of the existence of at least another quark generation, the b and t quarks being discovered in 1974 and 1995 respectively, the latter by the CDF and DØ experiments at the Tevatron [22, 23].

first generation	$\begin{pmatrix} \nu_e \\ e^- \end{pmatrix}_L$	e_R^-	$\begin{pmatrix} u \\ d \end{pmatrix}_L$	u_R	d_R
second generation	$\begin{pmatrix} \nu_\mu \\ \mu^- \end{pmatrix}_L$	μ_R^-	$\begin{pmatrix} c \\ s \end{pmatrix}_L$	c_R	s_R
third generation	$\begin{pmatrix} \nu_\tau \\ \mu^- \end{pmatrix}_L$	τ_R^-	$\begin{pmatrix} t \\ b \end{pmatrix}_L$	t_R	b_R

Table 1.1: Elementary fermions in the Standard Model.

The SM predicts three particle generations (table 1.1), each containing one pair of leptons and one of quarks. It describes three fundamental interactions: the electromagnetic interaction through the photon, the weak interaction through the Z and $W^\pm$ bosons and the strong interaction through the gluons. Nevertheless the SM remains an incomplete theory, since it does not include the last fundamental interactions: gravitation. The gravitational interaction amplitude is however negligible given the elementary particle mass scale and the collider energies (for example the gravitational attraction between an electron and a proton is 40 orders of magnitude smaller than their electromagnetic interaction).
In the following, the notion of field and the principles of the gauge theories will be firstly presented in Section 1.2 with the help of a simple case, QED. The SM will be then introduced in Section 1.3 and some possible extensions will be briefly discussed in Section 1.5.

1.2 Introduction to Gauge Theories

In quantum field theories, particles are described by quantized relativistic fields. At first these theories are generally developed at classical level with the use of Lagrangian formalism. Symmetry principles are then used to describe the different interactions as well as the conserved quantities by means of the gauge invariance and the Noether theorem. Theory is quantized for example by using the canonical quantization of Feynman's integral paths. At this point it must be determined if the theory is renormalizable, i.e. if it does not lead to infinite number of not-renormalizable parameters.

1.2.1 Fields and Symmetries

Noether theorem indicates that for every continuous symmetry a conserved physical quantity exists. Two distinct examples of symmetries can be found:

- external symmetries linked to the space-time properties, described by transformations of the Poincaré group: Lorentz transformation, rotations (conserving angular momentum) and space-time translations (conserving energy and momentum),
- internal symmetries, peculiar of the considered field, corresponding to gauge symmetries.

Invariance under the Poincaré group assures that the theory is relativistic and isotropic. Gauge symmetries are used to describe particle interactions.

Particles are described by quantized fields whose nature depends on the spin. Matter constituents have spin 1/2 and can be represented by two-component spinors, χ_L and χ_R, which correspond to right and left chiralities and are linked to each other by parity transformation. They are grouped in $quadri-spinor$ (χ_L, χ_R) or Dirac spinor. Force carriers have spin 1 and are represented by vector fields. Each particle type has its own free Lagrangian where the equations of motion describe their propagation.

1.2.2 Gauge Theory

In quantum mechanics, the phase of a wave function can be treated as an arbitrary rotation. Since this phase is not measurable, quantum mechanics has a *gauge invariance* or *gauge symmetry* for a phase changing transformation. In case this phase is constant, the gauge symmetry is global. In case the phase depends on the space-time, the gauge symmetry is local. In case of global gauge, theories are generally trivially invariant. Local gauges cases are more complex, since imposing the Lagrangian invariance under a local gauge transformation allows to "generate" the interactions and to introduce vectorial fields which mediate forces within the field theory formalism.

In particle physics, these gauge fields correspond to the gauge bosons. Local gauge transformation in the Standard Model are described by group transformation described by unitary matrix with unit determinant and dimensions $n \times n$ called $SU(n)$. Given unitary matrices $U(\theta^a)$ with parameters θ^a (with $a = 1, ..., d$) and a theory which implies a multiplet field ϕ_i (with $i = 1, ..., n$), the theory is symmetric under transformation:

$$\phi_i(x) \rightarrow \phi_i'(x) = U(\theta^a)_{ij}\phi_j(x), \tag{1.1}$$

if the equations of motion are unchanged by this transformation. This defines the Lagrangian invariance of the theory:

$$\mathcal{L}(\phi, \partial_\mu\phi) = \mathcal{L}(\phi', \partial_\mu\phi') = \mathcal{L}(U\phi, \partial_\mu U\phi) \tag{1.2}$$

An unitary matrix U can be expressed as a function of an Hermitian matrix H: $U = e^{iH}$. In case of an infinitesimal transformation it is possible to obtain:

$$U(\theta) = 1 + i\theta^a H^a + \mathcal{O}((\theta^a)^2) \tag{1.3}$$

and the field transformation $\phi_i(x)$ is written as

$$\phi_i'(x) = \phi_i(x) + i\theta^a H_{ij}^a \phi_j(x) + \mathcal{O}((\theta^a)^2) \tag{1.4}$$

where the θ^a are small. Hermitian matrices H^a are A matricial representation of the transformation group generators and constitute a Lie algebra:

$$[H^a, H^b] = iC^{abc}H_c. \tag{1.5}$$

Constants C^{abc} are called group transformation's structure constants. In case they are vanishing, the gauge theory is defined to be Abelian (the H^a matrices commute).
For example, we could consider the Dirac equation for a free electron under the local Abelian gauge symmetry $U(1)$ which simply corresponds to a complex phase $e^{i\theta(x)}$. The Dirac Lagrangian for a free electron can be written as

$$\mathcal{L}_D = \bar{\psi}(x)(i\gamma^\mu\partial_\mu - m)\psi(x), \tag{1.6}$$

where $\psi(x)$ and $\bar{\psi}(x)$ represent electron and positron respectively and m is the electron mass. The Lagrangian density 1.6 is trivially invariant under global symmetry $U(1)$:

$$\psi(x) \to \psi(x)' = e^{-i\theta}\psi(x), \tag{1.7}$$

$$\bar{\psi}(x) \to \bar{\psi}(x)' = e^{i\theta}\psi(x). \tag{1.8}$$

The corresponding local symmetry is:

$$\psi(x) \to \psi(x)' = e^{-i\theta(x)}\psi(x), \tag{1.9}$$

$$\bar{\psi}(x) \to \bar{\psi}(x)' = e^{i\theta(x)}\psi(x). \tag{1.10}$$

The Lagrangian mass term is invariant under local transformation, therefore the term containing derivative becomes:

$$\bar{\psi}(x)i\gamma^\mu\partial_\mu\psi(x) \to \bar{\psi}(x)i\gamma^\mu\partial_\mu + \bar{\psi}(x)\gamma^\mu(\partial_\mu\theta(x))\psi(x). \tag{1.11}$$

To balance this extra term, it is possible to introduce a "*gauge field*" $A_\mu(x)$ which under gauge $U(1)$ transforms as:

$$A_\mu(x) \to A_\mu(x)' = A_\mu(x) + \frac{1}{q}\partial_\mu\theta(x), \tag{1.12}$$

where q is the electron charge. Starting from this vector field, one can define a covariant derivative with the following transformation property:

$$D_\mu \psi(x) \rightarrow e^{-i\theta(x)} D_\mu \psi(x). \tag{1.13}$$

The covariant derivative is defined as:

$$D_\mu \psi(x) = (\partial_\mu + iqA_\mu(x))\psi(x). \tag{1.14}$$

With the introduction of the covariant derivative and the vector field $A_\mu(x)$, Lagrangian 1.6 becomes invariant under local gauge transformation $U(1)$. Adding a kinematic term, equally invariant under the gauge transformation, it is possible to give the gauge field a physical meaning. This kinetic term can be written as $F^{\mu\nu}F_{\mu\nu}$ where $F^{\mu\nu}$ is the Maxwell tensor defined as:

$$F_{\mu\nu} = \partial_\mu A_\nu(x) - \partial_\nu A_\mu(x). \tag{1.15}$$

Finally, the Lagrangian density 1.6 becomes:

$$\mathcal{L}_D^{QED} = \bar{\psi}(x)(i\gamma^\mu D_\mu - m)\psi(x) - \frac{1}{4}F^{\mu\nu}F_{\mu\nu} \tag{1.16}$$

$$= \bar{\psi}(x)(i\gamma^\mu \partial_\mu - m)\psi(x) - q\bar{\psi}\gamma^\mu A_\mu(x)\psi(x) - \frac{1}{4}F^{\mu\nu}F_{\mu\nu}. \tag{1.17}$$

The $\mathcal{L}_D^{QED}$ Lagrangian describes the so called quantum electrodynamics (QED). The first term of this Lagrangian corresponds to the fermion propagation and mass term while the second is the coupling between a fermion and a gauge boson: the photon. The last term describes the free photon propagation. The photon does not have a mass term $mA^\mu A_\mu$ which would break the gauge invariance.

1.2.3 Feynman Diagrams and Perturbative Expansion

A theory like the one described above needs to be quantized. The *path integral* quantization scheme allows the computation of a process by means of an integral summation procedure after perturbative expansion in terms of the coupling constant. For each term of this sum a certain number of *Feynman diagrams* can be introduced, in which functions describing free particles (the propagators) are represented as straight (waving) lines and each interaction vertex as an interconnection between the lines, as sketched in Fig. 1.1. The first order perturbative expansion of the $e^+e^- \rightarrow \mu^+\mu^-$ process can be used as example within the QED frame. When treated inclusively, the only relevant information is that the initial state must contain an electron-positron pair while the final state a muon-antimuon pair. Calculations for this process can be then expressed in form of Feynman diagram summation, as presented in Fig. 1.2. The first diagram is called *tree level diagram* and corresponds to the first order of the perturbative expansion. It has a quadratic dependence on the coupling constant (e^2) and is referred to as *Leading Order* (LO). The following diagrams are called *Next-to-Leading Order* (NLO) and correspond to the second order of the perturbative expansion, having a quartic dependence on the coupling constant (e^4).

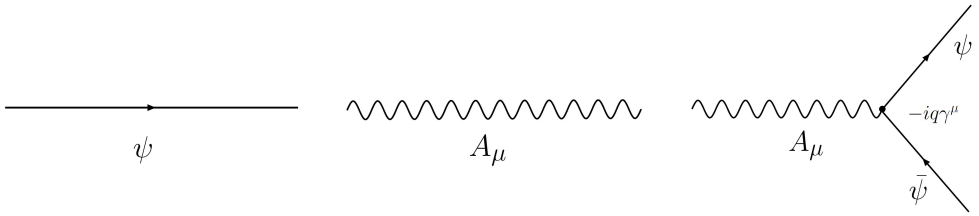

Figure 1.1: Feynman diagrams describing the particles (left), the propagators (middle) and the interaction vertex (right). ψ represents the matter fields and A_μ the gauge fields.

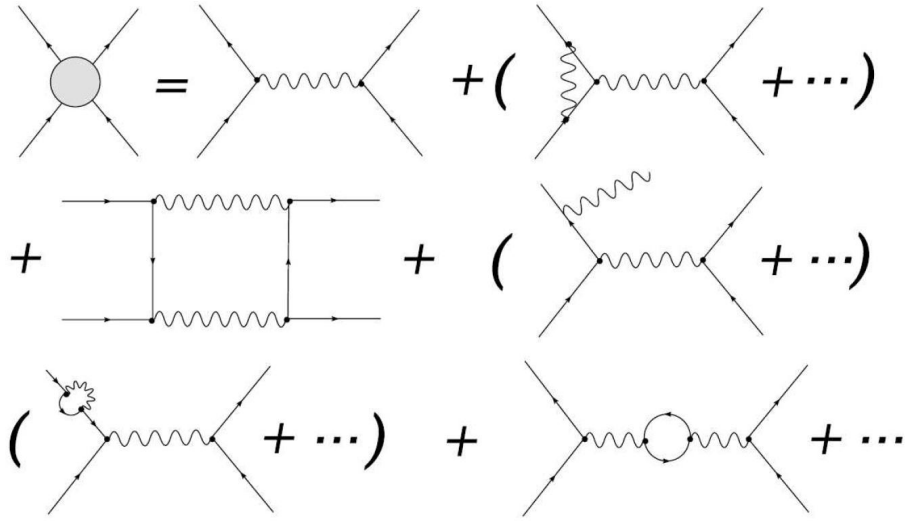

Figure 1.2: Sketch of the perturbative expansion in terms of Feynman diagrams for the process $e^+e^- \to \mu^+\mu^-$ at *Next-to-Leading Order*. In parenthesis only an example of the same diagram is represented.

1.2.4 Renormalization

Coupling constant power expansions take place in the propagators of both fermions (*self interaction*) and bosons (*vacuum polarization*). These terms introduce ultra-violet divergences in the physical quantities calculations, which are treated with the *renormalization* method. Renormalization is a procedure that allows one to balance the infinite contributions leading to renormalized fields, masses and constants. The idea is to define at first a theory with "bare" quantities (fields and constants). After renormalization, divergences coming from *self interaction* and bosons *vacuum polarization* are absorbed by the renormalized quantities. The presence of real emission diagrams balance the remaining infra-red divergences. The quantities become therefore finite and physical. Due to the renormalization procedure, the coupling constants and the particle masses "run" with the energy scale.

1.3 The Standard Model of Particle Physics

1.3.1 The Strong Force

In the sixties Gell-Mann and Zweig [24] suggested the existence of three quarks (u, d, s) as pointlike constituents of all observed hadrons: mesons, formed by a quark-antiquark pair, and the baryons, formed by combination of three quarks. The discovery of the Δ^{++}, Δ^{-} and Ω^{-} baryons, formed respectively by 3 quarks u, d and s suggested the existence of a new quantum number, the color. In fact, the quarks inside Δ^{++}, Δ^{-} and Ω^{-} particles (all with spin 3/2) are in the same quantum state, thus contradicting the Pauli exclusion principle. States like these could therefore exist only if a different quantum number existed for each constituent quark: the red, green and blue color charge (defined by convention) and their corresponding anti-colors. In quantum chromodynamics (QCD) quark bound states are only possible if the global hadron color is "white", i.e. null. For example a meson can't contain a blue colored quark if it does not contain an anti-blue colored antiquark. Baryons are composed by three different color quarks.

SU(3) Symmetry and Color Charge Quantum chromodynamics is a gauge theory based on the $SU(3)$ group, constituted by $n^2 - 1 = 8$ matrices associated to the color charge conservation. The $SU(3)$ Lie group algebra is a non-Abelian group defined as $[T_a, T_b] = if_{abc}T^c$ where f_{abc} are the structure constants of Lie algebra and the group generators are the T hermitian matrices, proportional to the Gell-Mann matrices. The gauge bosons corresponding to the Lagrangian's gauge invariance under a $SU(3)$ group transformation are called gluons. They are 8 (because there are 8 generators for the $SU(3)$ group), each carrying two colored charges. They can therefore self-interact, while this is not possible for the photons in the $U(1)$ case that do not carry electric charge.

Quantum Chromodynamics Quarks belong to the triplet representation of the color group $SU(3)_c$. As for the QED, the Lagrangian after the introduction of the gauge symmetry $SU(3)_c$ and the corresponding covariant derivative can be written as:

$$\mathcal{L}_D^{QCD} = \bar{\psi}(x)(i\gamma^\mu D_\mu - m)\psi(x) - \frac{1}{4}G_a^{\mu\nu}G_{\mu\nu}^a \tag{1.18}$$

$$= \bar{\psi}(x)(i\gamma^\mu \partial_\mu - m)\psi(x) - g_s\bar{\psi}\gamma^\mu T_a\psi(x)G_\mu^a(x) - \frac{1}{4}G_a^{\mu\nu}G_{\mu\nu}^a. \tag{1.19}$$

where the $G_{\mu\nu}^a$ are the gluon fields and g_s the strong coupling constant. The covariant derivative is defined as:

$$D_\mu = \partial_\mu + ig_s\lambda_a G_\mu^a \tag{1.20}$$

and the $G_{\mu\nu}^a$ tensors are defined as:

$$G_{\mu\nu}^a = \partial_\mu G_\nu^a - \partial_\nu G_\mu^a - gC^{abc}G_\mu^b G_\nu^c. \tag{1.21}$$

As for the QED, the first term of the Lagrangian density 1.19 correspond to the fermion propagation term and the second corresponds to the fermion-gluon coupling. The last term is related to the free gluons and is different with respect to QED. In fact it still includes the gluon propagation term but it describes also a gluon self-coupling due to the non-Abelian nature of the gauge symmetry $SU(3)_c$.

The Strong Coupling Constant Due to the renormalization process, the coupling constants depend on the energy. The evolution of the strong coupling constant as a function of the transferred energy Q and of the energy scale μ is given by the formula

$$\alpha_s(Q^2) = \frac{\alpha_s(\mu^2)}{1 + \frac{\alpha_s(\mu^2)}{4\pi}b_0 \ln\frac{Q^2}{\mu^2}}\ , \tag{1.22}$$

with $\alpha_s = \frac{g_s}{4\pi}$ and $b_0 = -\frac{2}{3}N_f + \frac{11}{3}N_c$, where N_f is the number of flavours (six) and N_c the number of colors (three) in the Standard Model. Due to its heavy mass, however, the top quark does not really enter the α_s calculations at the SM scale (set to $\sim$ 100 GeV by the vector boson masses). The number of "active" flavours is therefore 5. It is possible to deduce from the equation 1.22 the short and long distance behaviour of the strong interaction.

- At short distance (for high Q^2 values), α_s tends to 0. The force intensity therefore decreases with decreasing distance between the quarks. Two quarks infinitely close are therefore free, and this situation is defined as "asymptotic freedom".

- On the contrary, when the distance between two quarks is high (for low values of Q^2), the coupling constant α_s takes very high values and the theory is deprived of its perturbative character. The strong interaction amplitude at that point becomes so large that the quarks cannot escape as isolated particles. This phenomenon is called "confinement". A considerable energy is needed to "stretch" two quarks. When the injected energy is sufficient, a new quark-antiquark pair and two new hadrons are produced. This process, which creates hadron cascades, is called fragmentation and gives origin to the hadronic showers which are observed in the detector as jets.

QCD production at the LHC The tree level diagrams for the quark-antiquark production are reported in Fig. 1.3 for a proton-proton initial state. The effective production

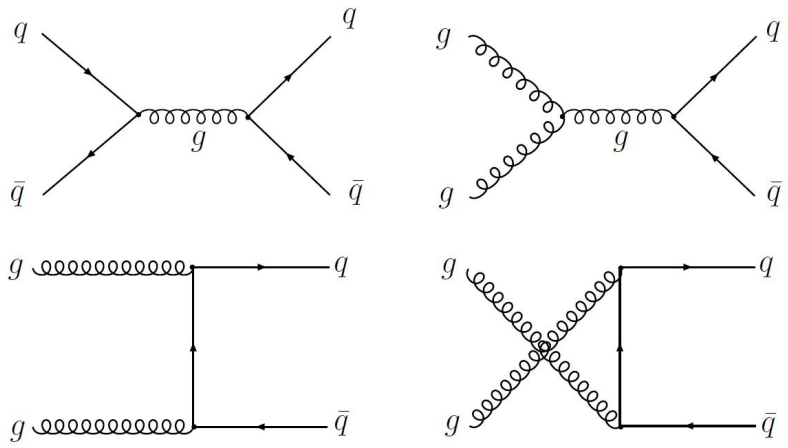

Figure 1.3: Quark-antiquark pair production diagram examples at tree level in proton-proton collisions: quark-quark annihilation (top left) and gluon fusion.

cross section for QCD processes is very high at the LHC energy scale, constituting a severe hadronic background for most searches of New Physics.
Heavy Flavor production at the LHC will be discussed further in Chapter 3.

1.3.2 The ElectroWeak Model

In Section 1.2 it has been showed how a gauge theory can be used to describe the electromagnetic interactions. Within the SM, this interaction is unified with the weak nuclear interaction. Parity violation in weak interaction was firstly proposed by T.D. Lee and C.N. Yang [25]. This hypothesis was confirmed experimentally by C.S. Wu and her collaborators in 1957 [26]. Fermions of different chiralities have different weak interactions, where the chiralities eigenstates are defined as:

$$\psi_L(x) = \frac{1-\gamma^5}{2}\psi(x) \quad \text{and} \quad \psi_R(x) = \frac{1+\gamma^5}{2}\psi(x). \tag{1.23}$$

The charged-current weak interaction in the SM maximally violates the parity, involving only left chirality fermions (or anti-fermions of right chirality). Following the left chirality projection $(1-\gamma^5)$, the weak interaction is said to have a V(vector) $-$ A(vector axial) nature. It is possible then to introduce a new local gauge symmetry associated to a conserved quantity: the weak isospin, based on the $SU(2)$ symmetry. Particles with left chirality are grouped into isospin doublets while those with right chirality are singlets, as reported in table 1.1. Each doublet has an isospin $T = 1/2$ and usually each field corresponds to an isospin projector $T_3 = \pm 1/2$. Right-handed fields behave like singlets under this symmetry, having therefore a null isospin.

The electroweak theory is built by introducing a supplementary conserved quantity which links electric charge and isospin: the "*ipercharge*", defined as:

$$Y = 2(Q - T_3). \tag{1.24}$$

Gauge theory of electroweak interactions is therefore constructed on the Lagrangian invariance under a local transformation of the $SU(2)_L \times U(1)_Y$ where L is referred to the left-handed character of the electroweak interaction and Y in the hypercharge (Glashow [8], Salam [9] and Weinberg [10]). The $SU(2)_L$ group is associated to three generators T_a (which represent the Pauli matrices) corresponding to three supplementary gauge bosons W_μ^a (with $a = 1, 2, 3$). The boson associated to the $U(1)_Y$ symmetry is denoted as B_μ. The electroweak Lagrangian is thus composed of different terms corresponding to the quark and leptons doublets and singlets. Taking for example the third quark family, which is described by a left-handed doublet and two right-handed singlets, one has:

$$Q_L = \begin{pmatrix} t \\ b \end{pmatrix}_L \quad b_R, t_R. \tag{1.25}$$

The corresponding terms of the electroweak Lagrangian are written as:

$$\begin{aligned} \mathcal{L}_{EW} = \bar{Q}_L(i\gamma^\mu D_\mu)Q_L + \bar{t}_R(i\gamma^\mu D_\mu)t_R + \bar{b}_R(i\gamma^\mu D_\mu)b_R \\ - \frac{1}{4}W^a_{\mu\nu}W_a^{\mu\nu} - \frac{1}{4}B_{\mu\nu}B^{\mu\nu} \end{aligned} \tag{1.26}$$

with

$$D_\mu = \partial_\mu + igT_aW_\mu^a + i\frac{g'}{2}YB_\mu, \tag{1.27}$$

where g and g' are the $SU(2)_L$ and $U(1)_Y$ coupling constants. The $W_a^{\mu\nu}$ and $B_{\mu\nu}$ are defined analogously as for the QED (equation 1.17) and QCD (equation 1.19) case.
After the symmetry breaking, the $W_a^{\mu\nu}$ and $B_{\mu\nu}$ fields neither describe physical fields nor gauge bosons. The physical fields A_μ (corresponding to the photon), Z_μ, W_μ^+ and W_μ^-, corresponding to the Z and $W^\pm$, are described as linear combination of the $W_a^{\mu\nu}$ and $B_{\mu\nu}$ fields:

$$A_\mu = \cos\theta_W B_\mu + \sin\theta_W W_\mu^3, \tag{1.28}$$

$$Z_\mu = -\sin\theta_W B_\mu + \cos\theta_W W_\mu^3, \tag{1.29}$$

$$W_\mu^\pm = \frac{W_\mu^1 \mp iW_\mu^2}{\sqrt{2}}, \tag{1.30}$$

where θ_W is the Weinberg electroweak mixing angle. The coupling constants g and g' are linked to θ_W and to the electromagnetic coupling constant e through the relation:

$$\tan\theta_W = \frac{g'}{g} \quad \text{and} \quad g'\cos\theta_W = e. \tag{1.31}$$

Since the electroweak Lagrangian mass terms for the gauge bosons violate the gauge invariance, the bosons need to be massless. While the photon is in fact massless, the short range feature of the Weak Interactions and the experimental measurements show that Z and $W^{\pm}$ are effectively massive, their mass having been measured with high precision at LEP [27] and Tevatron [28]:

$$m_Z = 91.1876 \pm 0.0021 \text{ GeV}, \tag{1.32}$$

$$m_W = 80.425 \pm 0.038 \text{ GeV}. \tag{1.33}$$

The mathematical mechanism which allows the introduction of gauge boson masses is based on the *"spontaneous electroweak symmetry breaking"* in presence of a scalar field: the Higgs field.

1.4 Symmetry breaking and the Higgs Model

A spontaneous breaking mechanism for the electroweak symmetry has been proposed by Higgs [29, 30, 31], Brout and Englert [32] to generate massive W ans Z gauge bosons. This mechanism is usually referred to as the Higgs mechanism. It consists in the introduction of a scalar complex iso-spinor field with zero electric charge into the electroweak Lagrangian:

$$\phi = \frac{1}{\sqrt{2}} \begin{pmatrix} \varphi_1 + i\varphi_2 \\ \varphi_3 + i\varphi_4 \end{pmatrix}. \tag{1.34}$$

In addition to the dynamical Higgs field term, a supplementary potential is introduced: the Higgs potential. The corresponding Higgs Lagrangian is written as:

$$\mathcal{L}_{Higgs} = D_\mu \phi D^\mu \phi^\dagger - V(\phi) \tag{1.35}$$

$$= D_\mu \phi D^\mu \phi^\dagger + \mu^2 \phi^\dagger \phi - \lambda (\phi^\dagger \phi)^2. \tag{1.36}$$

In case of $\mu^2 < 0$ and $\lambda > 0$, the Lagrangian 1.36 describes a massive scalar field and the vacuum state corresponds to the $\phi = 0$ case. On the contrary, if $\mu^2 > 0$ and $\lambda > 0$, an infinite set of degenerate minima exists for the potential. These minima are reached (leaving out a phase) in case of:

$$\phi^\dagger \phi = \frac{\mu^2}{2\lambda} = \frac{v^2}{2}, \tag{1.37}$$

where $v = \sqrt{\mu^2/\lambda}$. This potential of the Higgs form is illustrated in Fig. 1.4. We can therefore break the symmetry by choosing a fundamental state such as

$$\phi = \frac{1}{\sqrt{2}} \begin{pmatrix} 0 \\ v/\sqrt{2} \end{pmatrix}. \tag{1.38}$$

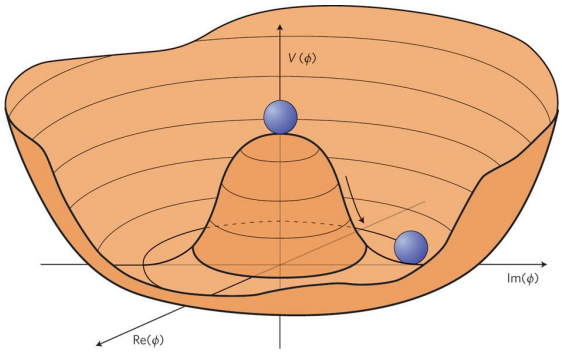

Figure 1.4: Sketch illustrating the Higgs potential and the symmetry breaking mechanism. Figure from [33].

Starting from this fundamental state with small perturbations, it is possible to expand the ϕ field in Taylor series close to the minimum $\phi(0)$:

$$\phi = \frac{1}{\sqrt{2}} \begin{pmatrix} 0 \\ v + H(x) \end{pmatrix}. \tag{1.39}$$

where $H(x)$ is a real function. The Goldstone theorem [34, 35, 36, 37] states that if a internal global symmetry is spontaneously broken, physical bosons (called *Goldstone bosons*) are created. In this case we refer to them as $\eta_a(x)$. In case of local symmetries, with the help of a gauge transformation, these terms are absorbed into the longitudinal polarization state of the massive vector bosons Z, W. The only remaining is the Higgs field $H(x)$. The coupling terms between the Higgs boson and the gauge bosons coming from the covariant derivative inside the Higgs Lagrangian 1.36 and the terms proportional to v correspond to the usual mass terms $m_W^2 W_\mu^+ W^{-\mu}$ and $m_Z^2 Z_\mu Z^\mu$. The masses of particles are therefore defined as effective masses coming from the Higgs potential. It is worth to remark that as the Higgs boson does not carry electrical charge, it does not couple with the photon, which stays massless.
The $W^\pm$, Z and the Higgs boson are defined as:

$$m_W = \frac{gv}{2} \tag{1.40}$$

$$m_Z = \frac{v}{2}\sqrt{g^2 + g'^2} \tag{1.41}$$

$$m_H = v\sqrt{2\lambda}. \tag{1.42}$$

The vacuum expectation value of the Higgs field is linked to the Fermi constant by the equation:

$$\frac{G_F}{\sqrt{2}} = \frac{1}{2v^2}, \tag{1.43}$$

which gives as result $v \approx 246$ GeV.
Fermion masses are defined by their coupling to the Higgs boson. These coupling terms are

called Yukawa couplings:

$$\mathcal{L} = -g_Y(\bar{f}_L \phi f_R + \bar{f}_R \phi \dagger f_L), \tag{1.44}$$

where f_L is a left-handed fermion doublet and f_R is a right-handed singlet. The g_Y are the Yukawa coupling constants for quarks and leptons and are free parameters of the theory, as well as the other coupling constants and the Higgs expectation vacuum value. It must be noted that neutrinos in the Standard Model are massless and do not have the right-handed singlet, therefore a Yukawa constant does not exist for these fermions.
Moreover, the quark mass eigenstates are not proper states of the flavor basis. The flavor interaction eigenstates are instead linear combinations of the mass eigenstates. A unitary mixing matrix is therefore introduced in the theory, corresponding to the base change from the interaction eigenstates to the mass eigenstates one. This matrix is called Cabibbo-Kobayashi-Maskawa or *CKM* matrix [38, 39]:

$$\begin{pmatrix} d' \\ s' \\ b' \end{pmatrix} = \begin{pmatrix} V_{ud} & V_{us} & V_{ub} \\ V_{cd} & V_{cs} & V_{cb} \\ V_{td} & V_{ts} & V_{tb} \end{pmatrix} \begin{pmatrix} d \\ s \\ b \end{pmatrix} \tag{1.45}$$

where the *down* quark vector on the left side of the equation correspond to the interaction eigenstates and the vector to the right side of the CKM matrix are the mass eigenstates. It must be noted that the diagonal elements of this matrix have values close to 1, which favors the flavour exchange within the same generation.

1.5 Beyond the Standard Model

The Standard Model has been tested at LEP and Tevatron with remarkable precision. For several reasons which will be briefly discussed hereafter, the Standard Model remains however incomplete. It is just an effective theory, valid at the energy scale accessible at the moment, corresponding to the low energy approximation of a more general theory whose effects should be observed at higher energies. Relevant missing elements of the SM are:

- **The Gravitation:** the gravitational interaction isn't considered within the SM, it is too weak (for instance between an electron and a proton there are roughly 40 orders of magnitude difference with the electromagnetic interaction) and is neglected. Nevertheless, at energies close to the Plank scale ($M_P = 2.4 \times 10^{18}$ GeV), this interaction is no longer negligible. The difficulties arise when trying to build a quantum theory of the gravitation. Such a theory is no longer renormalizable, is therefore impossible to remove the divergences inside the Feynman diagrams and the theory hasn't any predictive power.

- **Neutrino masses:** The observation of the neutrino oscillations proves that these particles are massive too, while within the SM they are considered massless [40, 41].

- **Dark matter:** there are several indirect evidences (like galaxy dynamics and gravitational lenses) that most of the gravitational matter is not constituted of visible matter [42]. For example a new kind of stable heavy particles, mostly gravitationally interacting (WIMP), has been advocated as the Dark matter source.

- **Dark energy:** the study of type Ia supernovae shows that the universe is accelerating while expanding. The reason of this expansion hasn't be determined yet, but it constitutes roughly 70% of the energy inside the universe. The known hadronic matter, described by the SM, represents just 5% of the global energy of the Universe.

The SM has furthermore some arbitrary elements:

1. **Radiative corrections to the Higgs mass, hierarchy problem:** at extremely high energies (Planck mass scale), quantum corrections to the Higgs boson mass can be relevant. It is necessary to make a $fine\text{-}tuning$ of the parameter Λ, which represents the scale of possible new physics, to let Higgs mass remain finite. This choice is however neither "natural" nor satisfactory.

2. **Number of free parameters:** the SM has 19 free parameter in total: the 3 coupling constants (strong, weak, electromagnetic), 9 charged fermion masses, 4 CKM matrix parameters, θ_{QCD} and 2 Higgs model parameters. This number raises to 25 is we include the neutrino masses and mixing angles. These parameters are not predicted from the theory and must be inferred from experimental observations.

3. **Number of generations:** The fact that exactly 3 particle generations exist is not explained by the SM.

4. **Mass hierarchy:** the mass differences between particles and particle generations are not explained. In particular, the top quark mass is significantly higher than other fermions and the W and Z bosons.

Due to these arguments, it seems natural to consider the SM as a low-energy effective theory of a wider theory. Numerous possible extensions to explain the physics beyond the SM are being widely tested at the Tevatron and the LHC. One of the most promising is $Supersymmetry$. The basic idea is to regulate the hierarchy problem by introducing new bosons and fermions such as to compensate the divergent terms in the radiative correction calculations. A new symmetry is therefore introduced (the $Supersymmetry$) which allows to transform a fermion into a boson and vice versa [43]. Thus for every SM fermion a boson exists. Since such particles haven't been observed as of today, the Supersymmetric particle masses must be of the order of TeV, at somewhat higher scale than those belonging to the SM. Furthermore, it is possible to adjust SUSY parameters so that Supersymmetry predicts the existence of a neutrally charged particle, weakly interacting and highly massive, which could be a good candidate to explain the dark matter. Finally, the coupling constants converge toward a common value at high energy. Other models (such as extra-dimensions, Technicolor and grand unified theories) solve a certain number of SM problems as well. As Supersymmetry, they predict new particles which could be discovered at the LHC.

Chapter 2

The CERN Large Hadron Collider and the Compact Muon Solenoid Experiment

The Large Hadron Collider (LHC) [44] is an accelerator located at the European Laboratory for Particle Physics Research (CERN) in Geneva. It has been conceived to collide proton beams at a center-of-mass energy of $\sqrt{s} = 14$ TeV and a nominal instantaneous luminosity of $\mathcal{L} = 10^{34}$ cm^{-2} s^{-1}, representing a seven-fold increase in energy and a hundred-fold increase in integrated luminosity over the previous hadron collider experiments. Its main purpose is to search for rare processes like the production of Higgs or new particles with mass of 1 TeV and beyond. Two experiments have been installed around the LHC to pursue these results: ATLAS [45] and CMS [46]. Furthermore, the LHCb [47] experiment studies the properties of charm and beauty hadrons produced with large cross sections in asymmetric collisions at the LHC, and the ALICE [48] experiment will analize the data from relativistic heavy ion collisions to study the hadronic matter in extreme temperature and density conditions (i.e. high quark-gluon density).

2.1 The Large Hadron Collider

The LHC has been installed in the same tunnel which hosted the e^+e^- collider LEP (Large Electron Positron). Accelerated electrons and positrons suffer large energy loss due to the synchrotron radiation, which is proportional to $E^4/(Rm^4)$, where E is the electron energy, m its mass and R the accelerator radius. To obtain energies of the order of TeV, at the fixed accelerator radius, only massive charged particles could have been used: protons and heavy nuclei. The energy loss is reduced by a factor $(2000)^4$ for a given fixed energy E.
Another important aspect of the LHC is the collision rate. To produce a sufficient number of rare processes, the collision rate needs to be very high. Beam protons are collected in packets called bunches. The collision rate is proportional to the instantaneous luminosity

of the accelerator, defined as:

$$\mathcal{L} = \frac{f k n_p^2}{4\pi\sigma_x\sigma_y}, \tag{2.1}$$

where f is the bunch revolution frequency, k the number of bunches, n_p the number of protons per bunch and σ_x, σ_y their transverse dispersion along the x and y axis. At the nominal 14 TeV LHC conditions ($\mathcal{L} = 10^{34} cm^{-2} s^{-1}$) the parameter values are: $k = 2808$, $n_p = 1.5 \times 10^{11}$ and $\sigma_x\sigma_y = 16.6$ μm (with $\sigma_z = 7.6$ cm along the beam). The integrated luminosity is defined as $L = \int \mathcal{L} dt$. For comparison we can consider the Tevatron accelerator at Fermilab, which produced proton-antiproton collisions since 1992. Its energy was 1.8 TeV up to 1998 and 1.96 TeV since 2001. To increase $\mathcal{L}$ by two orders of magnitude, protons are injected in both LHC beams instead of antiprotons. The latters, in fact, are obtained by steering proton beams onto a nickel target and represent only a small fraction of the wide range of secondary particles produced in this interactions.

The LHC is constituted by 1232 super-conducting dipole magnets each 15 m long, delivering a 8.3 T magnetic field to let the beams circulate inside their trajectories along the 27 km circumference. Two vacuum pipes are utilized to let beams circulate in opposite directions. A scheme representing the transverse dipole magnet section is represented in Fig. 2.1. More than 8000 other magnets are utilized for the beam injection, their collima-

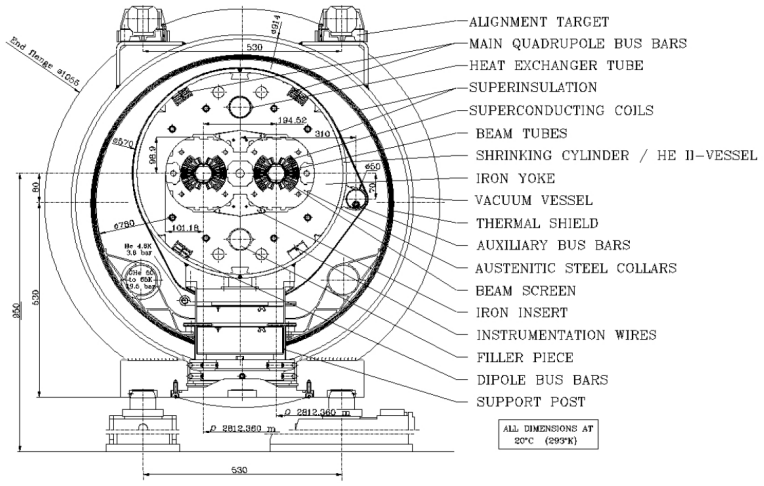

Figure 2.1: LHC dipole magnet section scheme. Figure from [44].

tion, trajectory correction, crossing. All the magnets are kept cool by superfluid helium at 1.9 K temperature.
The beams are accelerated from 450 GeV (the injection energy from the SPS) to 7 TeV with 16 Radio Frequency cavities (8 per beam) which raise the beam energy by 16 MeV each round with an electric field of 5 MV/m oscillating at 400 MHz frequency.
Before the injection into the LHC, the beams are produced and accelerated by different

components of the CERN accelerator complex. Being produced from ionized hydrogen atoms, protons are accelerated by the linear accelerator LINAC, Booster and the Proton Synchrotron (PS) up to 26 GeV energy, the bunches being separated by 25 ns each. The beams are then injected into the Super Proton Synchrotron (SPS) where they are accelerated up to 450 GeV. They are then finally transferred to the LHC and accelerated up to 7 TeV energy per beam. The CERN accelerator complex is illustrated in Fig. 2.2.

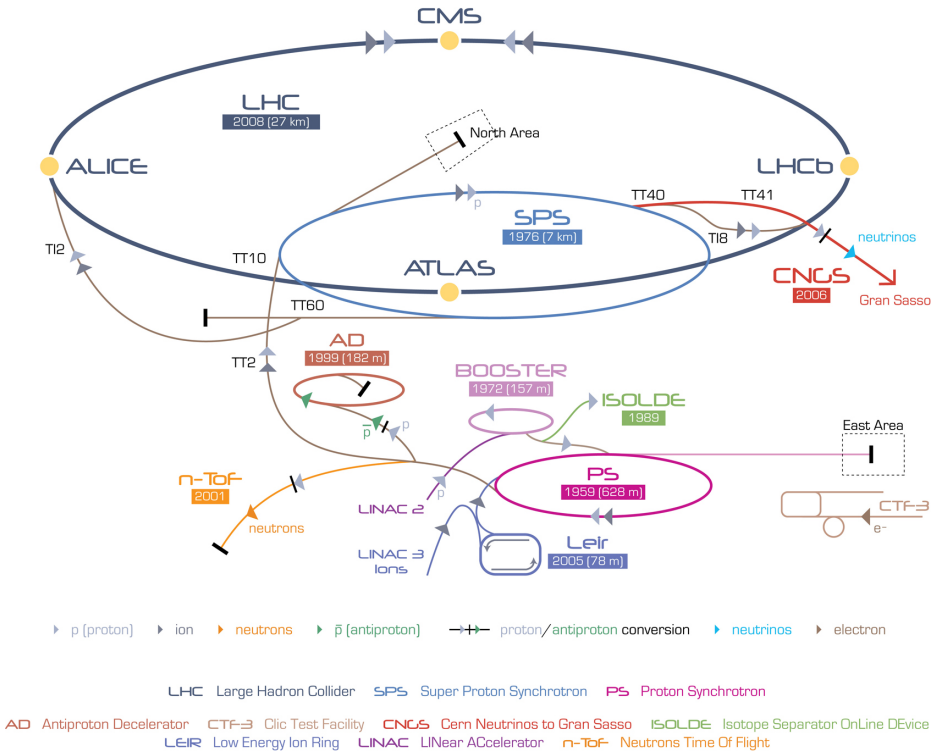

Figure 2.2: Scheme representing the CERN accelerator complex.

The LHC started its operations in December 2009 with center of mass energy $\sqrt{s} = 0.9$ TeV. The center of mass energy was set to $\sqrt{s} = 7$ TeV in 2010, and the performance during 2010 and 2011 raised impressively. In 2010 the peak luminosity reached $\mathcal{L} = 2 \times 10^{32} cm^{-2} s^{-1}$ (200 $\mu b^{-1} s^{-1}$, with 368 bunches) and during 2011 increased by a factor 10 in up to $\mathcal{L} = 3.5 \times 10^{33} cm^{-2} s^{-1}$ (3.5 $nb^{-1} s^{-1}$, with 1380 bunches). The integrated luminosity in 2010 has been $\mathcal{L} = 40$ pb^{-1}, while in 2011 it increased by a factor 100 up to ~ 5 fb^{-1}, as graphically summarized in Fig. 2.3.

2.2 Constraints on the Design of the CMS Experiment

The baseline for CMS detector performance is strongly constrained by the measurements it is aimed to [50, 51], which can be briefly summarized as:

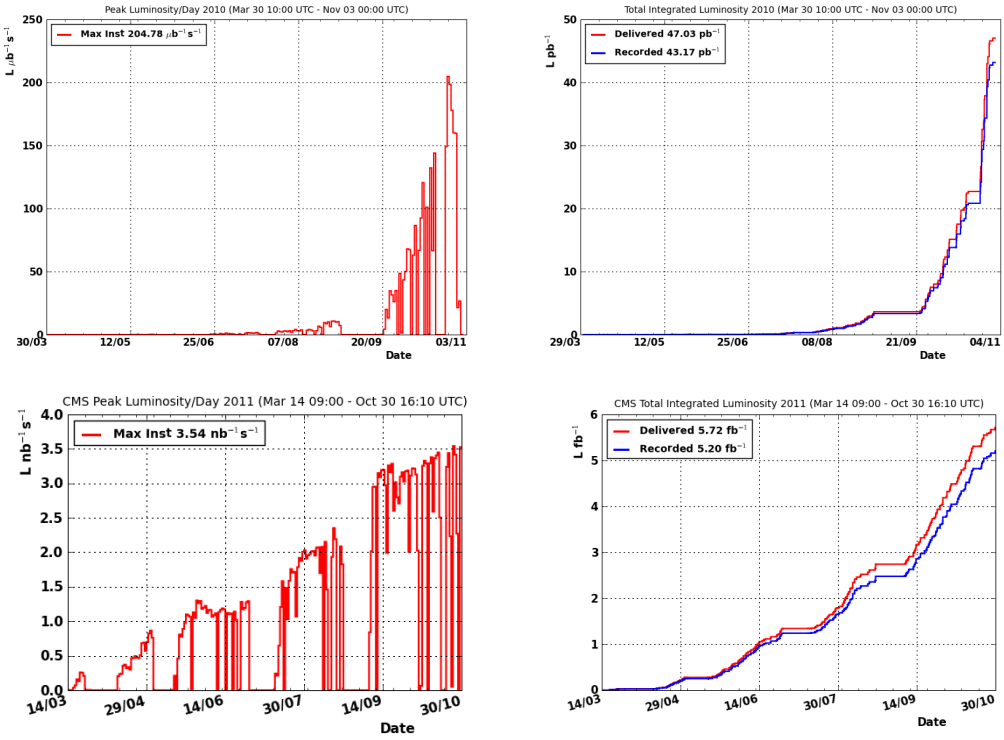

Figure 2.3: LHC performance in 2010 (top) and 2011 (bottom). Left: LHC peak luminosity; right: LHC integrated luminosity. Figures from [49].

- search for SM and MSSM Higgs boson decaying into photons, b quarks, τ leptons, W and Z bosons,
- search for additional heavy neutral gauge bosons predicted in many superstring-inspired theories or Great Unification theories and decaying to muon pairs,
- search for $B_0 \to \mu^+\mu^-$ decays,
- study for new quarks and leptoquarks,
- search for new physics in dijet events,
- search for SUSY at low masses in multijet plus large $\not\!\!E_T$ events[1] and other signatures,
- study of the violation of the CP symmetry in the decay of the B_s^0 meson into $J/\psi\phi \to \mu^+\mu^+K^+K^-$,
- study of QCD and jet physics at the TeV scale,
- study of top quark and EW physics.

CMS has been therefore designed as a multipurpose experiment, with particular focus on muon ($H \to ZZ \to 4\mu$), photon ($H \to \gamma\gamma$), and displaced tracks reconstruction. Superb performance have been achieved overall, in particular in:

1. primary and secondary vertex localization
2. charged particle momentum resolution and reconstruction efficiency in the tracking volume
3. electromagnetic energy resolution
4. isolation of leptons and photons at high luminosities
5. measurement of the direction of photons, rejection of $\pi^0 \to \gamma\gamma$
6. diphoton and dielectron mass resolution $\sim 1\%$ at 100 GeV
7. measurement of the missing transverse energy $\not\!\!E_T$ and dijet mass resolution
8. muon identification over a wide range of momenta
9. dimuon mass resolution $\sim 1\%$ at 100 GeV
10. unambiguously determining the charge of muons with p_T up to 1 TeV
11. triggering and offline tagging of τ leptons and b jets

[1] Missing transverse energy $\not\!\!E_T$ is the amount of energy which must be added to balance the modulus of the vector sum of the projections of the track momenta and calorimeter clusters in the plane perpendicular to beam axis.

2.3 The CMS Experiment

The Compact Muon Solenoid [46] is a general purpose detector housed at interaction region 5 of the CERN Large Hadron Collider. It is designed around a 4 T solenoidal magnetic field provided by the largest superconducting solenoid ever built. The structure of CMS is shown in Fig. 2.4, where particular emphasis is put on the volumes of the different subsystems: the Silicon Pixel Detector, the Silicon Strip Tracker, the Electromagnetic and Hadronic Calorimeters, and Muon Detectors.

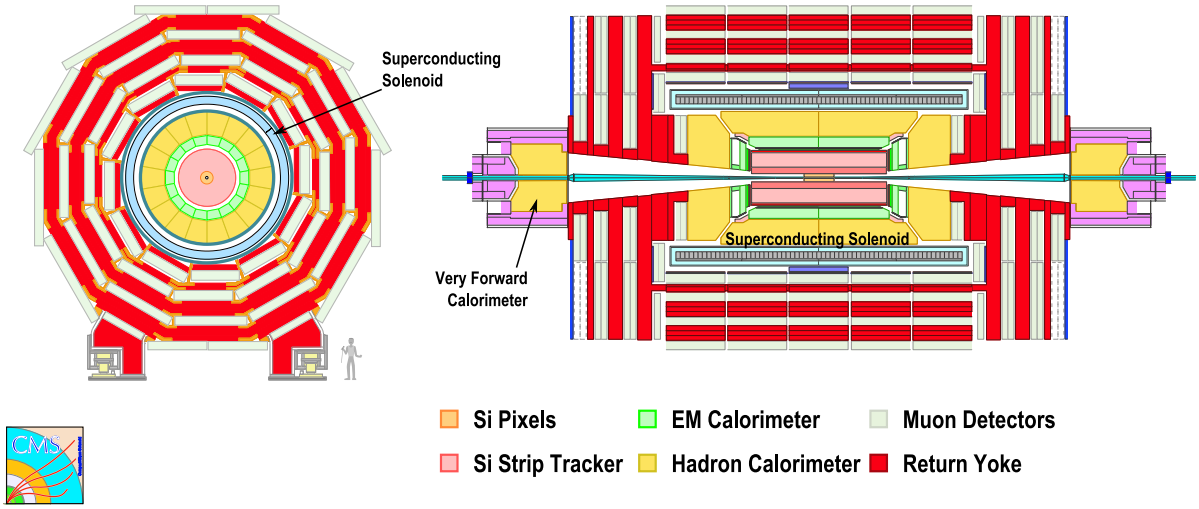

Figure 2.4: Transverse (left) and longitudinal (right) cross sections of the Compact Muon Solenoid detector showing the volumes of the different detector subsystems. The transverse cross section is drawn for the central barrel, coaxial with the beam line, while complementary end-caps are shown in the longitudinal view. Figures from [46].

The reference frame used to describe the CMS detector and the collected events has its origin in the geometrical center of the solenoid. It is embedded with different types of global coordinates measured with respect to the origin[2]:

- Cartesian coordinate system – $\hat{x}$ axis points towards the center of the LHC, $\hat{y}$ points upwards, perpendicular to the LHC plane, while $\hat{z}$ completes the right-handed reference, pointing along the beamline towards the Jura mountains

- polar coordinate system – directions are defined with an azimuthal angle $\tan\phi = y/x$ and a polar angle $\tan\theta = \rho/z$, where $\rho^2 = x^2 + y^2$

[2]Global coordinates are measured in the CMS reference frame while local coordinates are measured in the reference frame of a specific sub-detector or sensitive element.

- from polar angle the rapidity y and pseudorapidity η is obtained

$$y = \frac{1}{2} \ln \left(\frac{E + p_z}{E - p_z} \right) \tag{2.2}$$

$$\eta = -\ln \left(\tan \frac{\theta}{2} \right) = \lim_{m \to 0} y(|\mathbf{p}|, m) = \frac{1}{2} \ln \left(\frac{|\mathbf{p}| + p_z}{|\mathbf{p}| - p_z} \right) \tag{2.3}$$

2.3.1 Magnet

The whole CMS detector is designed around a ~ 4 T superconducting solenoid [52] 12.5 m long and with inner radius of 3 m. The solenoid thickness is 3.9 radiation lengths and it can store up to 2.6 GJ of energy.

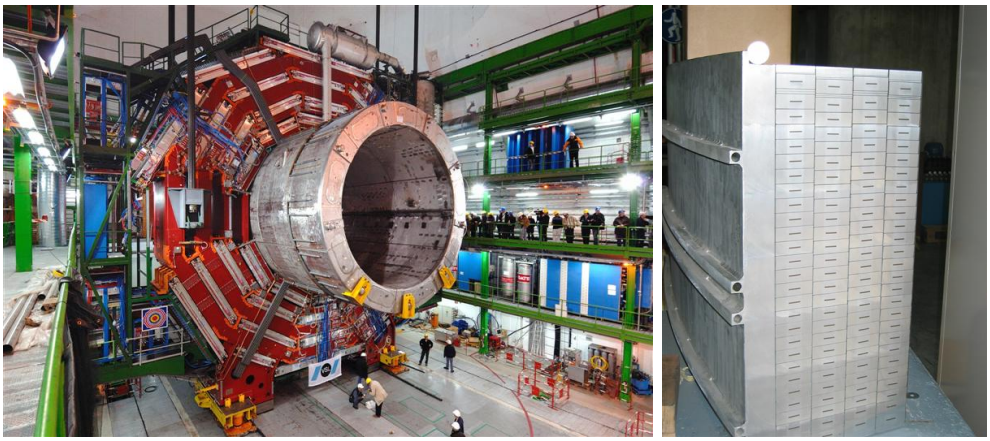

Figure 2.5: Left: CMS superconducting solenoid during assembly: the barrel return yokes are painted red. Muon detectors are already mounted and visible between return yoke layers. Right: cross section of the CMS magnet cables. Figures from [53].

The field is closed by a 10 000 t iron return yoke made of five barrels and two end-caps, composed of three layers each. The yoke is instrumented with four layers of muon stations. The coil is cooled down to 4.8 K by a helium refrigeration plant, while insulation is given by two pumping stations providing vacuum on the 40 m^3 of the cryostat volume.
The magnet was designed in order to reach precise measurement of muon momenta. A high magnetic field is required to keep a compact spectrometer without stringent demands on the spatial resolution and the alignment of muon chambers. A solenoidal field was chosen because it keeps the bending in the transverse plane, where an accuracy better than 20 μm is achieved in vertex position measurements. The size of the solenoid allows efficient muon detection and measurement up to a pseudorapidity of 2.4. The inner radius is large enough to accommodate both the Silicon Tracking System and the calorimeters. The magnet is currently operated at 3.8 T.

2.3.2 Tracking System

The core of CMS is a Silicon Tracking System [54, 55] with 2.5 m diameter and 5.8 m length, designed to provide a precise and efficient measurement of the trajectories of charged particles emerging from LHC collisions and reconstruction of secondary vertices.
The CMS Tracking System is composed of both silicon Pixel and Strip Detectors, as shown in Fig. 2.6. The Pixel Detector consists of 1440 pixel modules arranged in three barrel layers and two disks in each end-cap as in Fig. 2.7. The Strip detector consists of an inner tracker with four barrel layers and three end-cap disks and an outer tracker with six barrel layers and nine end-cap disks, housing a total amount of 15,148 strip modules of both single-sided and double-sided types. Its active silicon surface of about 200 m^2 makes the CMS tracker the largest silicon tracker ever built.

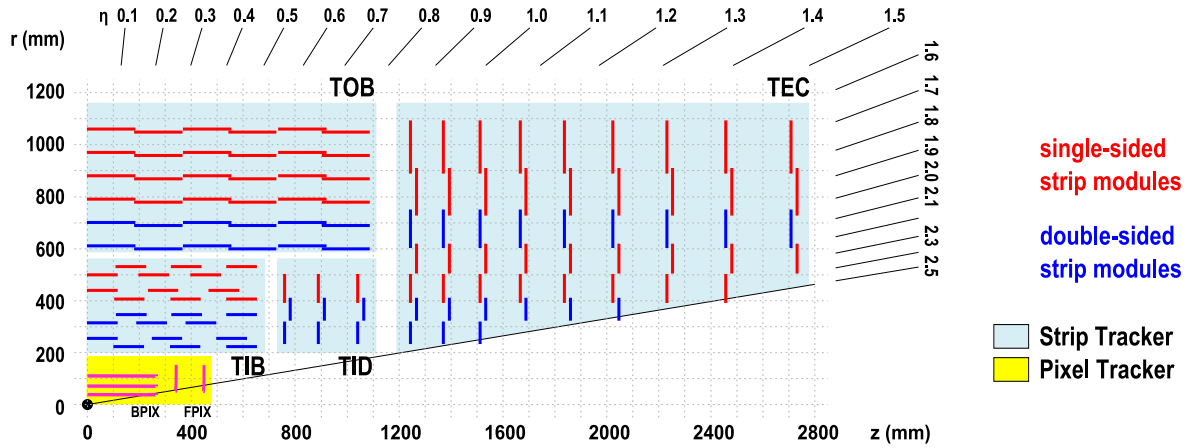

Figure 2.6: Layout of the CMS silicon tracker showing the relative position of hybrid pixels, single-sided strips and double-sided strips. Figure from [46].

The LHC physics programme requires high reliability, efficiency and precision in reconstructing the trajectories of charged particles with transverse momentum larger than 1 GeV in the pseudorapidity range $|\eta| < 2.5$. Heavy quark flavours can be produced in many of the interesting channels and a precise measurement of secondary vertices is therefore needed. The tracker completes the functionalities of ECAL and Muon System to identify electrons and muons. Also hadronic decays of tau leptons need robust tracking to be identified in both the one-prong and three-prongs topologies. Tracker information is heavily used in the High Level Trigger of CMS to help reducing the event collection rate from the 40 MHz of bunch crossing to the 100 Hz of mass storage.

Silicon Pixel Detector

The large number of particles produced in 25 piled-up events, at nominal LHC luminosity, results into a hit rate density of 1 MHz/mm^2 at 4 cm from the beamline, decreasing down

to 3 kHz/mm^2 at a radius of 115 cm. Pixel detectors are used at radii below 10 cm to keep the occupancy below 1%. The chosen size for pixels, 0.100×0.150 mm^2 in the transverse and longitudinal directions respectively, leads to an occupancy of the order of 10^{-4}. The layout of the Pixel Detector consists of a barrel region (BPIX), with three barrels at radii of 4.4, 7.3 and 10.2 cm, complemented by two disks on each side (FPIX), at 34.5 and 46.5 cm from the nominal interaction point. This layout provides about 66 million pixels covering a total area of about 1 m^2 and measuring three high precision points on each charged particle trajectory up to $|\eta| = 2.5$. Detectors in FPIX disks are tilted by 20° in a turbine-like geometry to induce charge sharing and achieve a spatial resolution of about 20 μm.

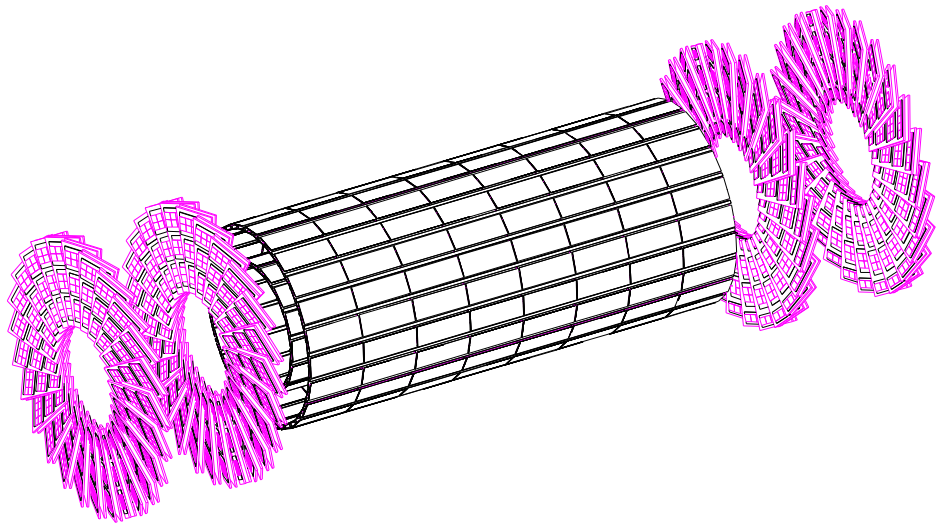

Figure 2.7: Layout of the current CMS Pixel Detector. Figure from [54].

Silicon Strip Tracker

In the inner Strip Tracker, which is housed between radii of 20 and 55 cm, the reduced particle flux allows a typical cell size of 0.080×100 mm^2, resulting in a 2% occupancy per strip at design luminosity. In the outer region, the strip pitch is increased to 0.180×250 mm^2 together with the sensor thickness which scales from 0.320 mm to 0.500 mm. This choice compensates the larger capacitance of the strip and the corresponding larger noise with the possibility to achieve a larger depletion of the sensitive volume and a higher charge signal.

The Tracker Inner Barrel and Disks (TIB and TID) deliver up to 4 r-ϕ measurements on a trajectory using 0.320 mm thick silicon strip sensors with strips parallel to the beamline. The strip pitch is 0.080 mm in the first two layers and 0.120 mm in the other two layers, while in the TID the mean pitch varies from 0.100 mm to 0.141 mm. Single point resolution in the TIB is 0.023 mm with the finer pitch and 0.035 mm with the coarser one. The Tracker

Outer Barrel (TOB) surrounds the TIB/TID and provides up to 6 r-ϕ measurements on a trajectory using 0.500 mm thick sensors. The strip pitch varies from 0.183 mm in the four innermost layers to 0.122 mm in the outermost two layers, corresponding to a resolution of 0.053 mm and 0.035 mm respectively. Tracker End-Caps (TEC) enclose the previous sub-detectors at 124 cm $< |z| <$ 282 cm with 9 disks carrying 7 rings of microstrips, 4 of them are 0.320 mm thick while the remaining 3 are 0.500 mm thick. TEC strips are radially oriented and their pitch varies from 0.097 mm to 0.184 mm.

As shown in Fig. 2.6, the first two layers and rings of TIB, TID and TOB, as well as three out of the TEC rings, carry strips on both sides with a stereo angle of 100 milliradians to measure the other coordinate: z in barrels and r in rings. This layout ensures 9 hits in the silicon Strip Tracker in the full acceptance range $|\eta| < 2.4$, and at least four of them are two-dimensional. The total area of Strip Tracker is about 198 m^2 read out by 9.3 million channels.

Trajectory Reconstruction

Due to the magnetic field charged particles travel through the tracking detectors on a helical trajectory which is described by 5 parameters: the curvature κ, the track azimuthal angle ϕ and polar angle η, the signed transverse impact parameter d_0 and the longitudinal impact parameter z_0. The transverse (longitudinal) impact parameter of a track is defined as the transverse (longitudinal) distance of closest approach of the track to the primary vertex, as explained in Section 3.5. The main standard algorithm used in CMS for track reconstruction is the Combinatorial Track Finder (CFT) algorithm [56] which uses the reconstructed positions of the passage of charged particles in the silicon detectors to determine the track parameters. The CFT algorithm proceeds in three stages: track seeding, track finding and track fitting. Track candidates are best seeded from hits in the pixel detector because of the low occupancy, the high efficiency and the unambiguous two-dimensional position information. The track finding stage is based on a standard Kalman filter pattern recognition approach [57] which starts with the seed parameters. The trajectory is extrapolated to the next tracker layer and compatible hits are assigned to the track on the basis of the χ^2 between the predicted and measured positions. At each stage the Kalman filter updates the track parameters with the new hits. In order to take into account possible inefficiencies one further candidate is created without including any hit information.

The tracks are assigned a quality based on the χ^2 and the number of missing hits and only the best quality tracks are kept for further propagation. Ambiguities between tracks are resolved during and after track finding. In case two tracks share more than 50% of their hits, the lower quality track is discarded. For each trajectory the finding stage results in an estimate of the track parameters. However, since the full information is only available at the last hit and constraints applied during trajectory building can bias the estimate of the track parameters, all valid tracks are refitted with a standard Kalman filter and a second filter (smoother) running from the exterior towards the beam line. The expected performance

of the track reconstruction is shown in Fig. 2.9 for muons, pions and hadrons. The track reconstruction efficiency for high energy muons is about 99% and drops at $|\eta| > 2.1$ due to the reduced coverage of the forward pixel detector. For pions and hadrons the efficiency is in general lower because of interactions with the material in the tracker.
The material budget is shown in Fig. 2.8 as a function of both pseudorapidity and different contributions of sub-detectors and services.

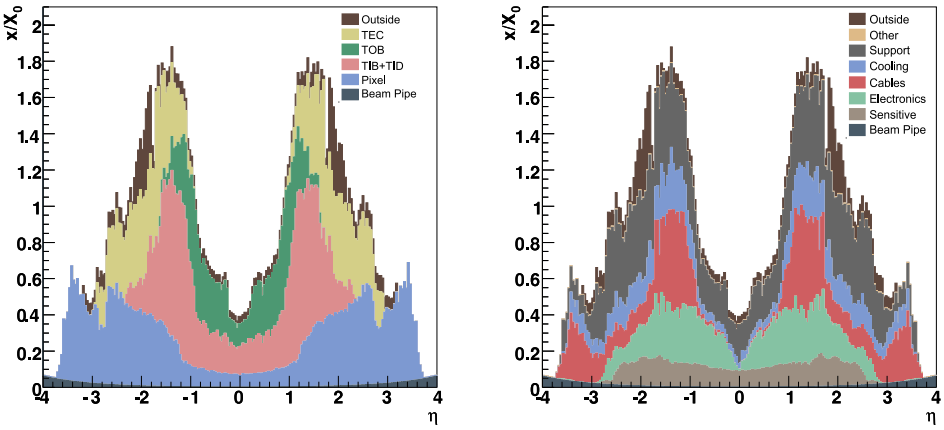

Figure 2.8: Material budget of the current CMS Tracker in units of radiation length X_0 as a function of the pseudorapidity, showing the different contribution of sub-detectors (left) and functionalities (right). Figures from [46].

The performance of the Silicon Tracker in terms of track reconstruction efficiency and resolution, of vertex and momentum measurement, are shown in Fig. 2.9 and 2.10 respectively. The first one, in particular, shows the difference in reconstruction efficiency for muons and pions, due to the larger interaction cross section of pions, which cannot be assumed to be minimum-ionizing particles and therefore are much more degraded by the amount of material.

Vertex Reconstruction The reconstruction of interaction Vertices allows CMS to reject tracks coming from pile-up events. The primary vertex reconstruction is a two-step process. Firstly the reconstructed tracks are grouped in vertex candidates and their z coordinates at the beam closest approach point are evaluated, retaining only tracks with impact parameter less than 3 cm. Vertices are then reconstructed through a recursive method for parameter estimation through a Kalman filter [58] algorithm. For a given event, the primary vertices are ordered according to the total transverse momentum of the associated tracks, $\sum p_T$. The vertex reconstruction efficiency is very close to 100% and the position resolution is of the order of $\mathcal{O}(10)$ μm in all directions.

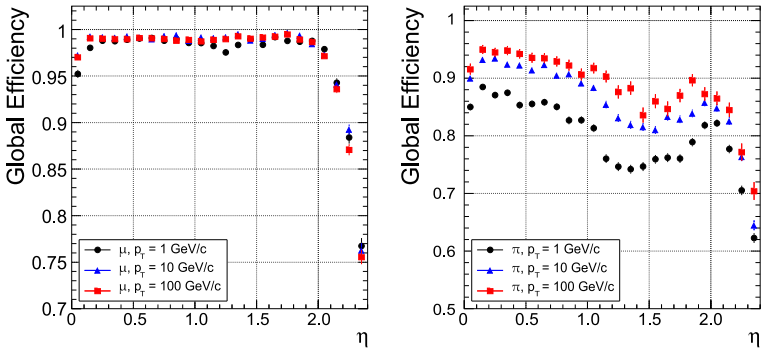

Figure 2.9: Global track reconstruction efficiency as a function of track pseudorapidity for muons (left) and pions (right) of transverse momenta of 1, 10 and 100 GeV. Figures from [46].

It is also possible to reconstruct the secondary vertices, for example those from b-quark decays. The secondary vertex reconstruction uses tracks associated to jets applying further selection cuts: the transverse impact parameter of the tracks must be greater than 100 μm to avoid tracks coming from the primary vertex and below 2 cm to avoid tracks from pileup events.

2.3.3 Muon Spectrometer

Detection of muons at CMS exploits different technologies and is performed by a "Muon System" rather than a single detector [59]. While electromagnetic and hadronic backgrounds are mainly contained inside the calorimeters, muons are able to travel through the solenoid with minimal energy loss inside the detector. Muons can provide strong indication of interesting signal events and are natural candidates for triggering purposes. The CMS Muon System was designed to cope with three major functions: robust and fast identification of muons, good resolution of momentum measurement and triggering.
The Muon System is composed of three types of gaseous detectors, located inside the empty volumes of the iron yoke, and therefore arranged in barrel and end-cap sections. The coverage of Muon System is shown in Fig. 2.11.

In the barrel region the neutron-induced background is small and the muon rate is low; moreover, the field is uniform and contained in the yoke. For these reasons, standard drift chambers with rectangular cells are used. The barrel drift tubes (DT) cover the $|\eta| < 1.2$ region and are organized in four stations housed among the yoke layers. The first three stations contain 12 chambers, arranged in two layers providing measurement in the transverse plane and one layer measuring along z, each of them containing four chambers. The fourth station provides measurement only in the transverse plane. To eliminate dead spots in the efficiency and any left-right ambiguity, cells in consecutive layers are shifted by half

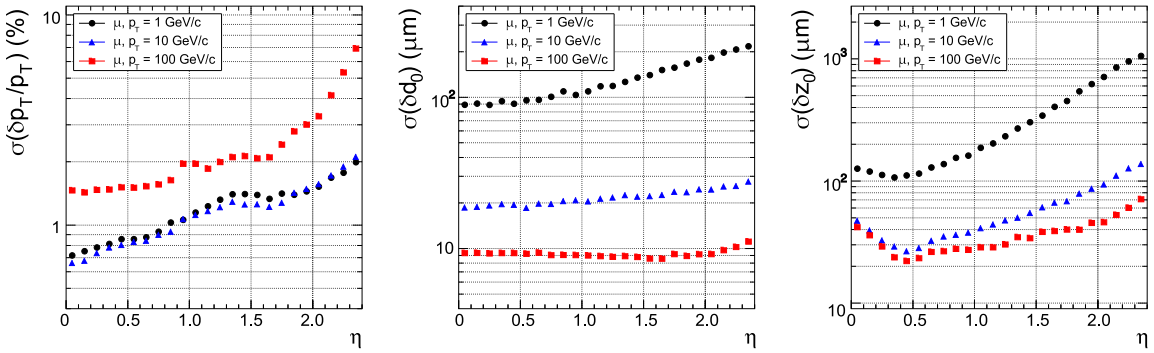

Figure 2.10: Resolution of several track parameters as a function of track pseudorapidity for single muons with transverse momenta of 1, 10 and 100 GeV: transverse momentum (left), transverse impact parameter (middle) and longitudinal impact parameter (right). Figures from [46].

of their width.

Both the muon rates and backgrounds are high in the forward region, where the magnetic field is large and non uniform. The choice for muon detectors fell upon cathode strip chambers (CSC) because of their fast response time, fine segmentation and radiation tolerance. Each end-cap is equipped with four stations of CSC's. The CSC's cover the $0.9 < |\eta| < 2.4$ pseudorapidity range. The cathode strips are oriented radially and provide precise measurement in the bending plane, the anode wires run approximately perpendicular to the strips and are read out to measure the pseudorapidity and the beam-crossing time of a muon. The muon reconstruction efficiency is typically 95-99% except for the regions between two barrel DT wheels or at the transition between DT's and CSC's, where the efficiency drops.

Both the DT's and CSC's can trigger on muons with a Level 1 p_T resolution of 15% and 25%, respectively. Additional trigger-dedicated muon detectors were added to help in measuring the correct beam-crossing time. These are Resistive Plate Chambers (RPC), gaseous detector operated in the avalanche mode, which can provide independent and fast trigger with high segmentation and sharp p_T threshold over a large portion of the pseudorapidity range. The overall p_T resolution on muons is shown in Fig. 2.12, with emphasis on the different contribution from the Muon System and the Silicon Tracker.

Muon Reconstruction

Muon detection and reconstruction play a key role in the CMS physics program, both for the discovery of New Physics and for precision measurements of SM processes. CMS has been designed for a robust detection of muons over the entire kinematic range of the LHC and in a condition of very high background. The muon system allows an efficient and pure

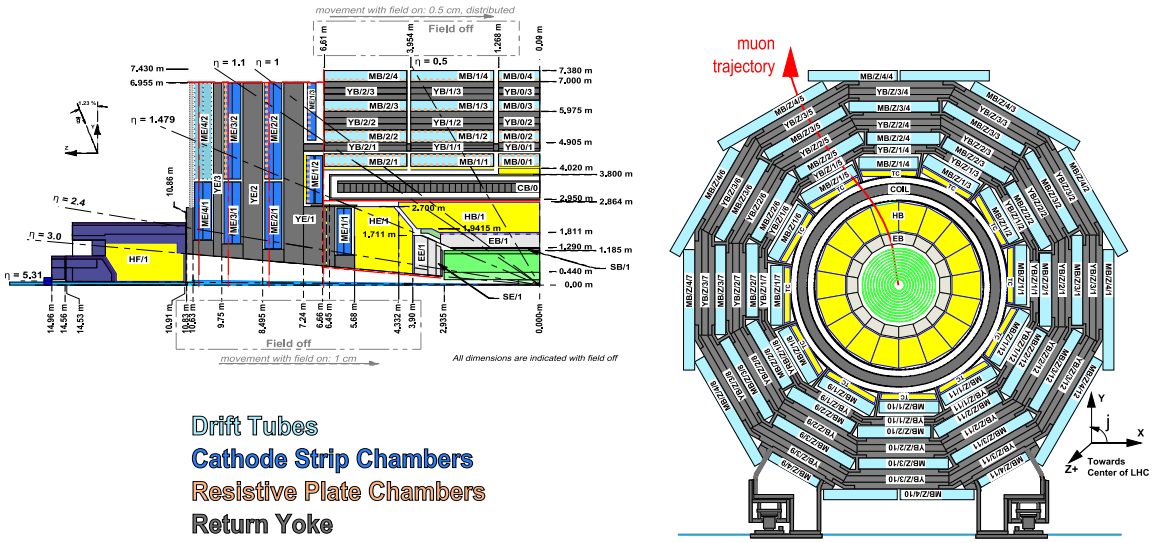

Figure 2.11: Transverse and longitudinal cross sections of the CMS detector showing the Muon System with particular emphasis on the different technologies used for detectors; the ME/4/2 CSC layers in the end-cap were included in the design but are not currently installed. Figures from [46].

identification of muons, while the inner tracker provides a very precise measurement of their properties. An excellent muon momentum resolution is made possible by the high-field solenoidal magnet. The steel flux return yoke provides additional bending power in the spectrometer, and serves as hadron absorber to facilitate the muon identification. Several muon reconstruction strategies are available in CMS, in order to fulfill the specific needs of different analyses. The muon reconstruction consists of three main stages:

1. local reconstruction: in each muon chamber, the raw data from the detector read-out are reconstructed as individual points in space; in CSC and DT chambers, such points are then fitted to track stubs (*segments*);

2. stand-alone reconstruction: points and segments in the muon spectrometer are collected and fitted to tracks, referred to as "stand-alone muon tracks";

3. global reconstruction: stand-alone tracks are matched to compatible tracks in the inner tracker and a global fit is performed using the whole set of available measurements: the resulting tracks are called "global muon tracks".

Muon identification represents a complementary approach with respect to global reconstruction: it starts from the inner tracker tracks and flags them as muons by searching for matching segments in the muon spectrometer. The muon candidates produced with this strategy are referred to as "tracker muons".
After the completion of both algorithms, the reconstructed stand-alone, global and tracker

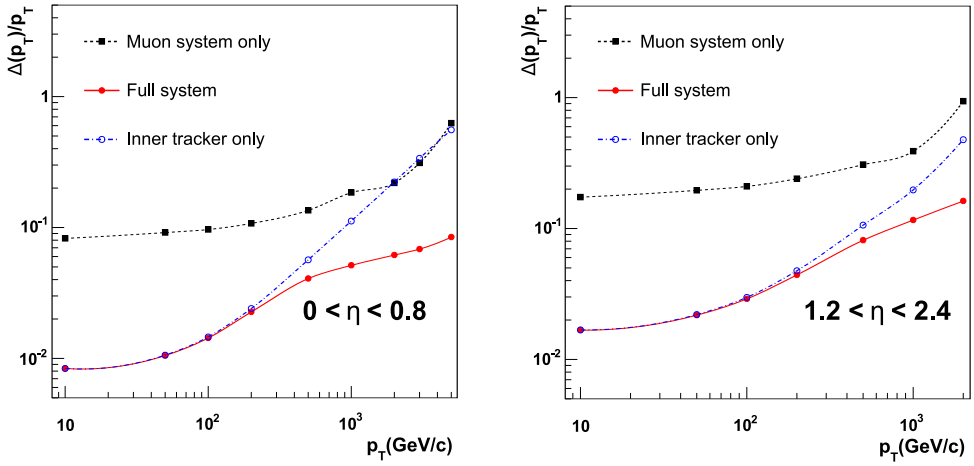

Figure 2.12: Resolution on p_T measurement of muons with the Muon System, the Silicon Tracker or both, in the barrel (left) and end-caps (right). Figures from [46].

muons are merged into a single software object, with the addition of further information, like the energy collected in the matching calorimeter towers. This information can be used for further identification, in order to achieve a balance between efficiency and purity of the muon sample.

2.3.4 Calorimetry

Identification of electrons, photons, and hadrons relies on accurate calorimetry, which is a destructive measurement of the energy of a particle. As in most of the particle physics experiments, a distinction is made between electromagnetic calorimetry and hadron calorimetry. Electromagnetic calorimetry is based on the production of EM showers inside a high-Z absorber, while hadron calorimetry measures the effects of inelastic scattering off heavy nuclei of hadrons, including production of photons from neutral pions and muons, and neutrinos from weak decays. Calorimetry must be precise and hermetic also to measure any imbalance of momenta in the transverse plane which can signal the presence of undetected particles such as high-p_T neutrinos.

The electromagnetic calorimeter of CMS, ECAL, is a homogeneous calorimeter, where the absorber material is the same as the sensitive one [60]. ECAL is composed of 61,200 lead tungstate ($PbWO_4$) crystals in the barrel region and 7,324 crystals in the end-caps, as shown in Fig. 2.13. The crystal cross-section is 22×22 mm^2 at the front face, while the length is 230 mm. End-caps are equipped with a preshower detector. $PbWO_4$ was chosen because of its high density, 8.28 g/cm^3, short radiation length, 0.89 cm, small Molière radius, 2.2 cm. This way, the calorimeter can be kept compact with fine granularity, while scintillation and optical properties of $PbWO_4$ make it fast and radiation tolerant.

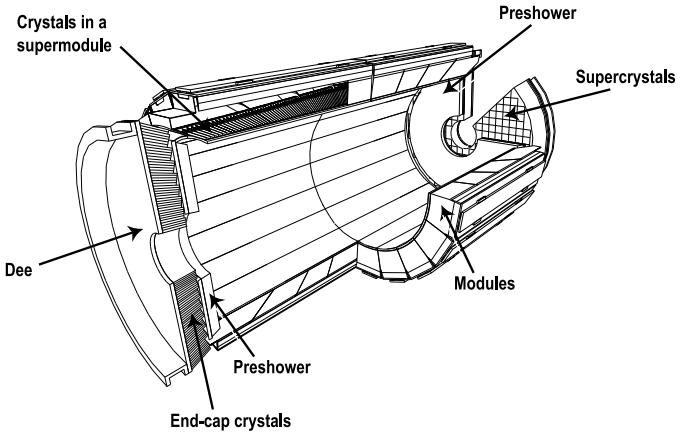

Figure 2.13: Cut-away view of the CMS ECAL showing the hierarchical structure of crystals arranged in supercystals and modules and the orientation of crystals whose major axis is always directed to the origin of the reference frame. Figure from [60].

Signal transmission exploits total internal reflection. Scintillation light detection relies on two different technologies. Avalanche photodiodes (APD) are used in the barrel region, mounted in pairs on each crystals, while vacuum phototriodes (VPT) are used in the end-caps. The preshower detector is a sampling calorimeter composed of lead radiators and silicon strips detectors, and it is used to identify neutral pions in the forward region. The nominal energy resolution, measured with electron beams having momenta between 20 and 250 GeV, is

$$\left(\frac{\sigma_E}{E}\right)^2 = \left(\frac{2.8\%}{\sqrt{E}}\right)^2 + \left(\frac{0.12}{E}\right)^2 + (0.30\%)^2 \tag{2.4}$$

where the different contributions are respectively: the stochastic one, due to fluctuations in the lateral shower containment and in the energy released in the preshower, that due to electronics, digitization and pile-up, and the constant term, due to intercalibration errors, energy leakage from the back of the crystal and non-uniformity in light collection.

The hadron calorimeter of CMS, HCAL, is a sampling calorimeter employed for the measurement of hadron jets and neutrinos or exotic particles resulting in apparent missing transverse energy [61]. A longitudinal view of HCAL is shown in Fig. 2.14. The hadron calorimeter size is constrained in the barrel region, $|\eta| < 1.3$, by the maximum radius of ECAL and the inner radius of the solenoid coil. Because of this, the total amount of the absorber material is limited and an outer calorimeter layer is located outside of the solenoid to collect the tail of the showers. The pseudorapidity coverage is extended in the $3 < |\eta| < 5.2$ by forward Cherenkov-based calorimeters. The barrel part, HB, consists of 36 wedges, segmented into 4 azimuthal sectors each, and made out of flat brass absorber layers, enclosed between two steel plates and bolted together without any dead material on the full radial extent. There are 17 active plastic scintillator tiles interspersed between the

stainless steel and brass absorber plates, segmented in pseudorapidity to provides an overall granularity of $\Delta\phi \times \Delta\eta = 0.087 \times 0.087$. The same segmentation is maintained in end-cap calorimeters, HE, up to $|\eta| < 1.6$, while it becomes two times larger in the complementary region. The maximum material amount in both HB and HE corresponds to approximately 10 interaction lengths λ_I. The energy resolution on single electron and hadron jets is shown in Fig. 2.15.

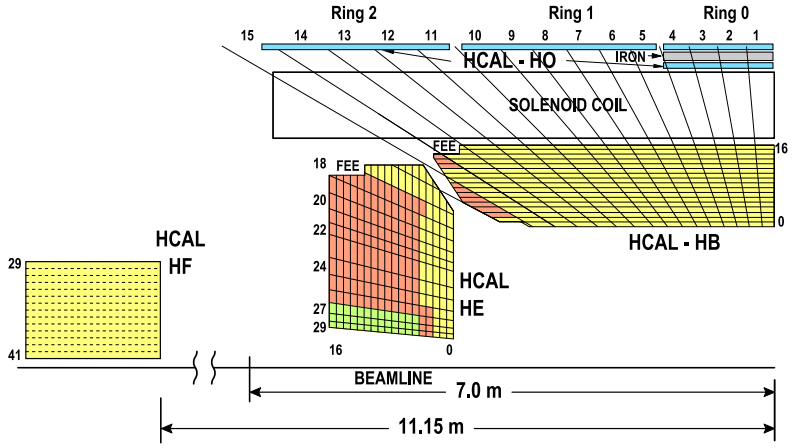

Figure 2.14: Cross section of the CMS HCAL showing the tower segmentation. Figure from [61].

2.3.5 Trigger and Data Acquisition

High bunch crossing rates and design luminosity at LHC correspond to approximately 20-25 superimposed events every 25 ns, for a total of 10^9 events per second. The large amount of data associated to them is impossible to store and process, therefore a dramatic rate reduction has to be achieved. This is obtained with two steps: the Level 1 Trigger [62] and the High Level Trigger, HLT [63].

The Level 1 Trigger is based on custom and programmable electronics, while HLT is a software system implemented on a $\sim$ 1000 commercial processors farm. The maximum allowed output rate for Level 1 Trigger is 100 kHz, which should be even kept lower, about 30 kHz, for safe operation. Level 1 Trigger uses rough information from coarse segmentation of calorimeters and Muon Detectors and holds the high-resolution data in a pipeline until acceptance/rejection decision is made. HLT exploits the full amount of collected data for each bunch crossing accepted by Level 1 Trigger and is capable of complex calculations such as the off-line ones. HLT algorithms are those expected to undergo major changes in time, particularly with increasing luminosity. Configuration and operation of the trigger

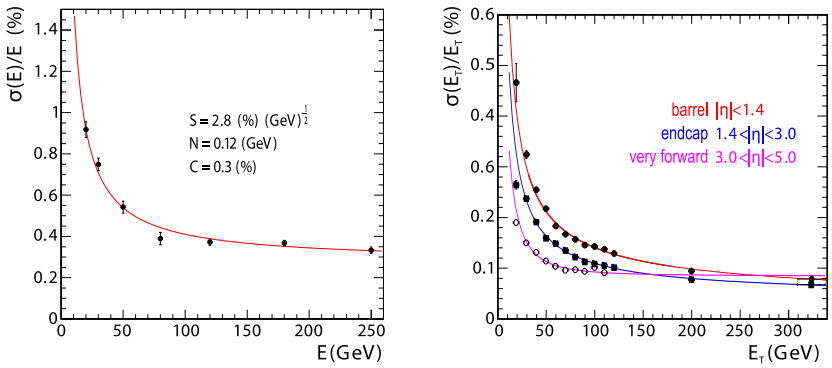

Figure 2.15: Left: ECAL energy resolution as a function of the electron energy as measured from a beam test. The energy was measured in a 3×3 crystals array with the electron impacting the central one. The stochastic, noise and constant terms are given. Right: the jet transverse energy resolution as a function of the transverse energy for barrel jets, end-cap jets and very forward jets reconstructed with an iterative cone algorithm with cone radius $R = 0.5$. Figures from [46].

components are handled by a software system called Trigger Supervisor.

The Level 1 Trigger relies on local, regional and global components. The Global Calorimeter and Global Muon Triggers determine the highest-rank calorimeter and muon objects across the entire experiment and transfer them to the Global Trigger, the top entity of the Level 1 hierarchy. The latter takes the decision to reject an event or to accept it for further evaluation by the HLT. The total allowed latency time for the Level 1 Trigger is 3.2 μs. A schematic representation of the Level 1 Trigger data flow is presented in Fig. 2.16.

Muon Trigger

All Muon Detectors – DT, CSC and RPC – contribute to the Trigger. Barrel DT's provide Local Trigger in the form of track segments in ϕ and hit patterns in η. End-cap CSC's provide 3-dimensional track segments. Both CSC's and DT's provide also timing information to identify the bunch crossing corresponding to candidate muons. The Local DT Trigger is implemented in custom electronics. BTI's, Bunch and Track Identifiers, search for coincidences of aligned hits in the four equidistant planes of staggered drift tubes in each chamber superlayer. From the associated hits, track segments defined by position and angular direction are determined. TRACO's, Track Correlators, attempt to correlate track segments measured in DT ϕ superlayers, enhancing the angular resolution and producing a quality hierarchy.

The requirement of robustness implies redundancy, which introduces, however, a certain amount of noise or duplicate tracks giving rise to false Triggers. Therefore the BTI's, the TRACO's and the different parts of the Local Trigger contain complex noise and ghost re-

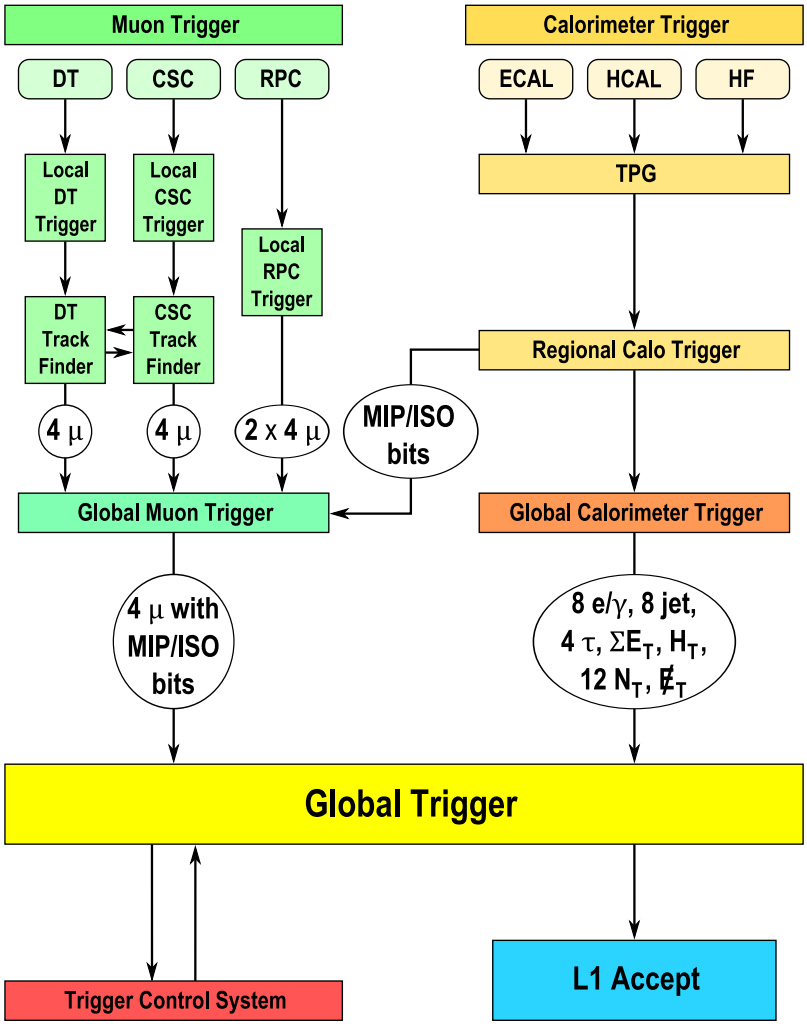

Figure 2.16: Schematic representation of the Level 1 Trigger data flow.

duction mechanisms. The position, transverse momentum and quality of tracks are coded and transmitted to the DT regional Trigger, called the Drift Tube Trigger Track Finder (DTTF), through high-speed optical links.

The Global Muon Trigger combines the information from DT's, CSC's and RPC's, achieving an improved momentum resolution and efficiency compared to the stand-alone systems. It also reduces the Trigger rate and suppresses backgrounds by making use of the complementarity and redundancy of the three Muon Systems. The Global Muon Trigger also exploits MIP/ISO bits from the Regional Calorimeter Trigger. A muon is considered isolated if its energy deposit in the calorimeter region from which it emerged is below a defined threshold. DT and CSC candidates are first matched with barrel and forward RPC candidates based on their spatial coordinates. If a match is possible, the kinematic parameters are merged. Several merging options are possible and can be selected individually for all track

parameters, taking into account the strengths of the individual Muon Systems. Muons are back-extrapolated through the calorimeter regions to the vertex, in order to retrieve the corresponding MIP and ISO bits, which are then added to the GMT output and can be taken into account by the Global Trigger. Finally, the muons are sorted by transverse momentum and quality to deliver four final candidates to the GT. The Muon Trigger is designed to cover up to $|\eta| < 2.4$.

Global Trigger

The Global Trigger takes the decision to accept or reject an event at Level 1, based on candidate e/γ, muons, jets, a s well as global quantities such as the sums of transverse energies (defined as $E_T = E \sin\theta$), the missing transverse energy vector $\not{E}_T$, the scalar transverse energy sum of all jets above a chosen threshold (usually identified by the symbol H_T), and several threshold-dependent jet multiplicities. Objects representing particles and jets are ranked and sorted. Up to four objects are available and characterized by their p_T or E_T, direction and quality. Charge, MIP and ISO bits are also available for muons. The Global Trigger has five basic stages implemented in FPGAs: input, logic, decision, distribution and read-out. If the Level 1 Accept decision is positive, the event is sent to the Data Acquisition stage.

High Level Trigger and Data Acquisition

The CMS Trigger and DAQ system is designed to collect and analyze the detector information at the LHC bunch crossing frequency of 40 MHz. The rate of events to be recorded for offline processing and analysis is of the order of a few 10^2 Hz. The first level Trigger is designed to reduce the incoming average data rate to a maximum of 100 kHz, by processing fast Trigger information coming from the Calorimeters and the Muon System, and selecting events with interesting signatures. Therefore, the DAQ system must sustain a maximum input rate of 100 kHz, and must provide enough computing power for a software filter system, the High Level Trigger (HLT), to reduce the rate of stored events by a factor of 1000. In CMS all events that pass the Level 1 Trigger are sent to a computer farm (Event Filter) that performs physics selections, using faster versions of the offline reconstruction software, to filter events and achieve the required output rate. The various sub-detector front-end systems store data continuously in 40-MHz pipelined buffers. Upon arrival of a synchronous Level 1 Trigger Accept via the Timing, Trigger and Control System (TTCS) the corresponding data are extracted from the front-end buffers and pushed into the DAQ system by the Front-End Drivers (FED's). The event builder assembles the event fragments belonging to the same Level 1 Trigger from all FED's into a complete event, and transmits it to one Filter Unit (FU) in the Event Filter for further processing. The DAQ system includes back-pressure from the filter farm through the event builder to the FED's. During operation, Trigger thresholds and pre-scales will be optimized in order to fully utilize the available DAQ and HLT throughput capacity.

2.3.6 Detector Performance with Early Data

The CMS detector was initially commissioned with test beams data and muons from cosmic rays [64] before the LHC startup. Commissioning was refined with the early LHC data. The key aspects were calibration and alignment of sub-detectors, validation of reconstruction algorithms, comparison of detector response (reconstructed physics objects) with simulation predictions, validation and tuning of trigger algorithms and menus.

At the end of 2010 *pp* collisions, the maximum instantaneous luminosity reached $\mathcal{L} = 2{\times}10^{32}$ cm^{-2} s^{-1}. In this conditions CMS could no longer rely on a Minimum Bias trigger, since the rate was too high. Several L1 and HLT trigger configurations were developed to maintain a total rate to the HLT of about 65 kHz and a sustainable output rate of about 400 Hz. To control the rates, the thresholds were raised, conditions were tightened, and prescales adjusted. Several sets of prescales were tuned to collect as much data as possible, keeping the thresholds as low as possible for physics studies.
A charged particle reconstruction is one of primary aspects to understand the event content. The CMS tracker performance measured in collision conditions are very close to their nominal values [65, 66]. The validation of tracking reconstruction algorithms includes studies of resolution and efficiency of track and primary vertices finding, multiple interaction extraction, determination of beam line position and width.
The left plot in Fig. 2.17 shows the Primary Vertex (PV) reconstruction efficiency as a function of the number of tracks associated to the PV. The reconstruction efficiency is almost 100% for PVs consisting of at least three associated charged tracks. The resolution of the reconstructed PV, as a function of the number of tracks, is shown in the middle and right plot in Fig. 2.17. For a PV with more than 10 tracks of average $p_T > 1.2$ GeV the reconstructed resolution is close to 20 μm.

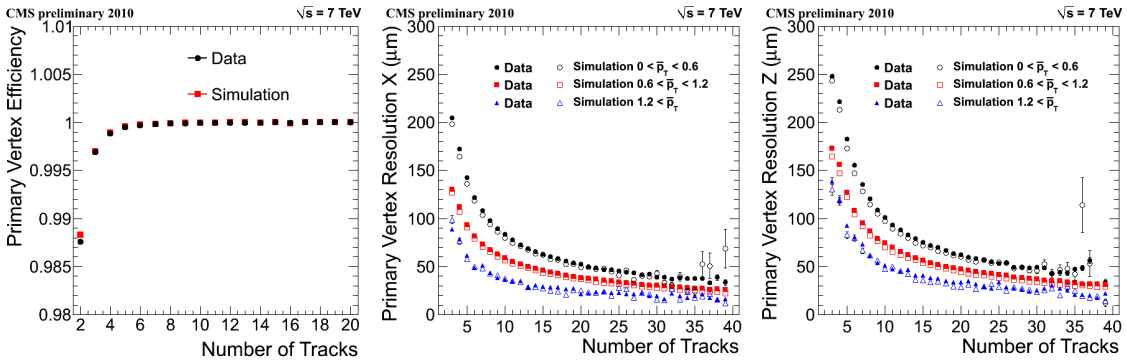

Figure 2.17: Left: The primary vertex reconstruction efficiency as a function of the number of associated tracks. Middle and right: The primary vertex resolution in x and z as a function of the number of associated tracks for different average transverse momentum p_T. Figures from [66].

The impact parameter resolution is measured by removing tracks that belong to the PV

and re-reconstructing both the removed track and the PV [66]. The resulting measured resolution is shown in Fig. 2.18. The measured resolution in data agrees very well with the simulation. The transverse (longitudinal) resolution is $\sim$ 30 ($\sim$ 60) μm for a track with $p_T \sim 6$ GeV. The hadron-track reconstruction efficiencies are found to be consistent between

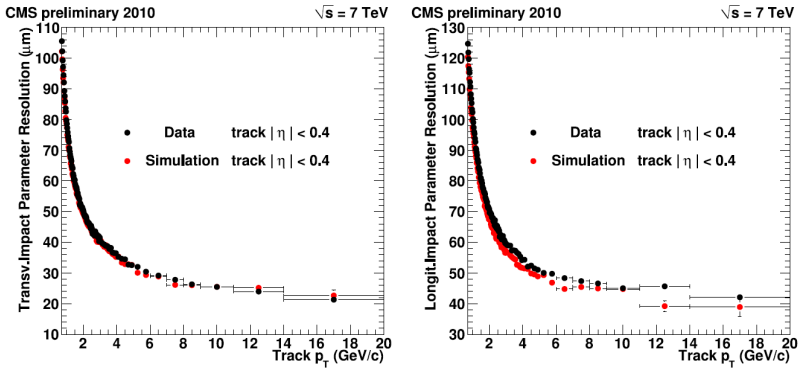

Figure 2.18: The measured resolution of the track transverse (left) and longitudinal (right) impact parameter as a function of track p_T. Figures from [66].

data and simulation within their uncertainty of about 4% [67]. Particle identification is possible up to a momentum of roughly 1 GeV using the energy loss in the silicon-strip tracker. The left plot in Fig. 2.19 shows the observed energy loss as a function of the track momentum, projected are the fitted lines of the kaon, proton and deuteron mass hypothesis. As a complementary thesis activity, aimed to understand the background from kaon misidentification to muons, the decay $\phi \to K^+K^-$ has been studied selecting two charged kaons with dE/dx The invariant mass distribution is shown in Fig. 2.19 for the kaon candidates, as well as for candidates failing the kaon identification.

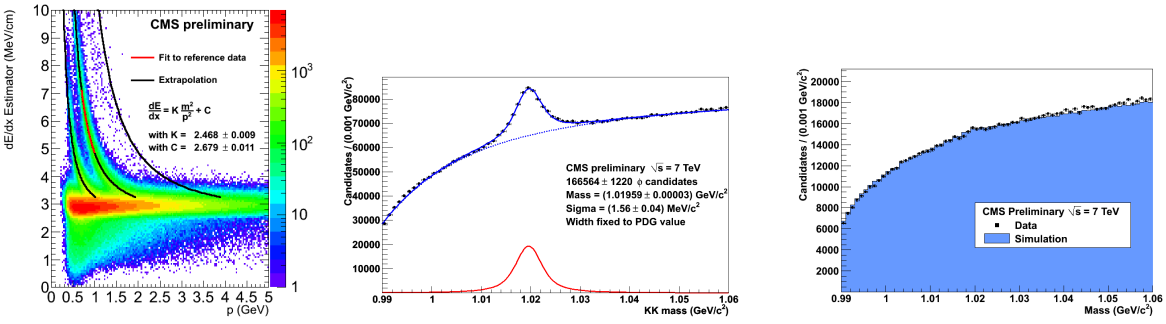

Figure 2.19: Left: The distribution of the measured dE/dx versus the momentum of the track. Center: Fit to the invariant mass distribution of kaon candidates selected with dE/dx obtained in data for the $\phi \to K^+K^-$ decay. Right: Mass distribution of kaon candidate pairs in simulation (blue area) and in data (points), when at least one track fails the dE/dx requirement. Figures from [65].

An excellent muon reconstruction is one of design points of the CMS experiment. The period of an early commissioning with proton beams was dominated by validation of local reconstruction inside muon stations, alignment, calibration and data synchronisation. It has been followed by studies of muon identification and reconstruction [68]. This includes analysis of reconstruction algorithms by comparison with generator expectations, validation of muon isolation algorithms, analysis of muon deposit in calorimeters, cosmic backgrounds, hadron decays in-flight, punch through probability and muon trigger performance. In all cases the agreement with simulation predictions was met. As a part of the thesis activity, the misidentification of muons due to hadronic punch-through and decays in flight in the muon systems was determined by exploiting the $\phi \to K^+K^-$ decays (as reported above) together with $K^0_s \to \pi^+\pi^-$, $\Lambda \to p\pi^-$ [68]. The misidentification probabilities for "Global Muons" are presented in Fig. 2.20. They are less than 2‰ in good agreement with the MC expectation.

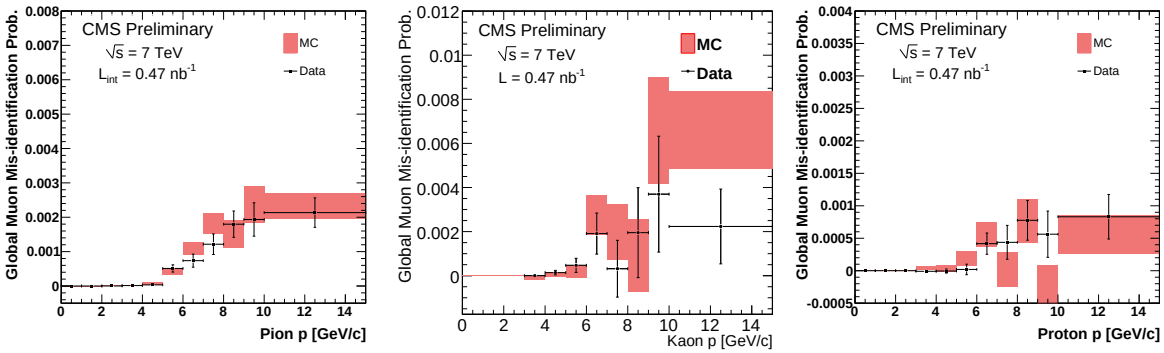

Figure 2.20: The fraction of pions (left), kaons (middle) and protons (right) that are misidentified as global muons as a function of momentum. The uncertainties that are indicated by error bars (data) and the grey boxes (simulation) are statistical only. Figures from [68].

An illustration of the excellent performance of the tracker and the muon system is the distribution of the invariant mass for pairs of opposite charge muons, shown in Fig. 2.21. One can note the fine-structure of Υ family. The relative momentum resolution is measured using the J/ψ-mass line-shape [69] and is presented in Fig. 2.22.

The precise measurement of electromagnetic cascades is a vital aspect for the search of the Higgs boson in the $\gamma\gamma$ final state as well as many exotic channels involving photons or electrons. Thus, the early 2010 data were used to improve calorimeter commissioning and analyse reconstruction performance [70, 71]. This includes validation of crystal transparency, thermal stability and timing alignment, efficiency and calibration measurements. The invariant mass of photons from π^0 decays and dielectrons from Z decays provide clear illustrations of the of calorimeter performance. They are shown in Fig. 2.23. A good agreement with Monte-Carlo prediction is visible.
Jet reconstruction is another benchmark for CMS. Jets are among the main physics objects to verify predictions of the Standard Model in the LHC energy regime. For the

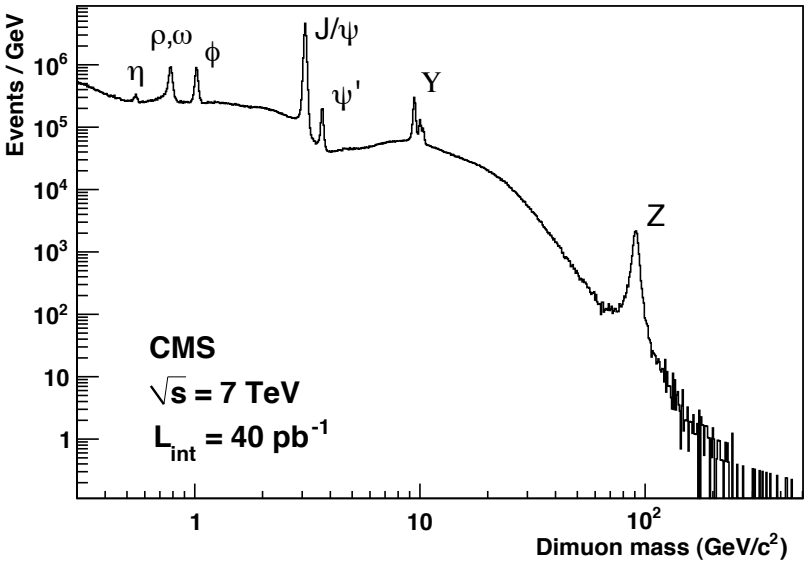

Figure 2.21: Invariant mass distributions of opposite sign dimuon pairs with η, (ρ, ω), ϕ, J/ψ, ψ', $\Upsilon(1S, 2S, 3S)$, and Z mass peaks visible.

jet reconstruction CMS has adopted the anti-k_T clustering algorithm [72] combined with the Particle-Flow method [73]. The CMS Particle-Flow event reconstruction attempts to identify and reconstruct individually all particles produced in collisions, using information from all CMS detectors. This information is used at the level of jet clusterization allowing for more precise jet reconstruction.

An important part of CMS commissioning is study of jet energy response and resolution [74, 75, 76]. Since the energy measured in the detector differs from the particle jet energy, a factorized procedure for the jet energy calibration was developed. There are three types of corrections applied. The energy offset correction is supposed to remove contributions from calorimeter electronic noise and pile-up. The relative correction compensates non-uniform pseudorapidity response of the calorimeter. The absolute correction removes variation in jet response as a function of jet transverse momentum (p_T). In order to determine jet energy corrections CMS is using Monte-Carlo truth information and physics processes for validation and in-situ calibration (resulting currently in small additional correction). The di-jet p_T balance is used for validation of relative corrected jet energy response while photon plus jet balance method provides measurement of the absolute energy scale. The Jet Energy correction vs. η is better than 1% and the Jet Energy scale uncertainty is $3 - 5\%$ over the whole p_T range.

The Particle-Flow method applied to the reconstruction of missing transverse energy and jets is used in most of physics analyses in CMS. Early CMS results obtained in the measurement of b-quark jets, illustrating not only quality of preparation of CMS for data taking but also a high quality of CMS simulation, will be presented in Section 4.1.

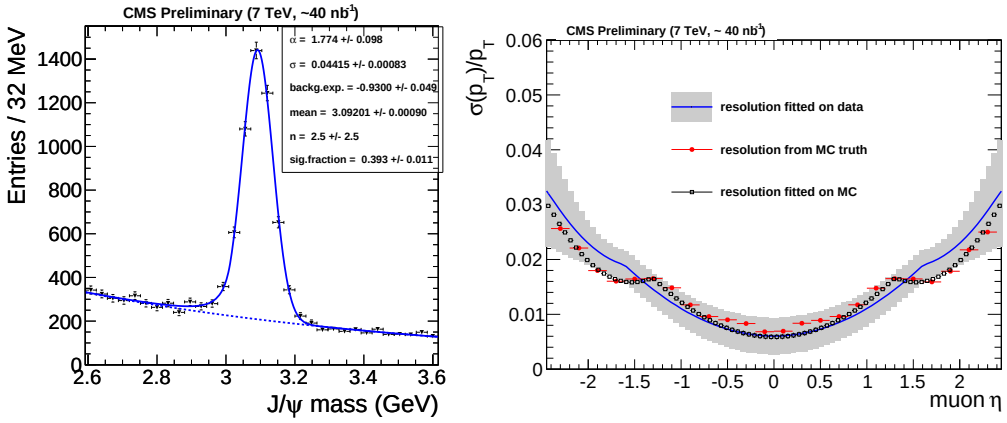

Figure 2.22: Left: J/ψ mass distribution as measured with ~ 40 nb^{-1} of integrated luminosity. Right: resolution on transverse momentum using J/ψ as measured with the same of integrated luminosity (black line) compared to the Monte Carlo prediction computed from Monte Carlo truth (red points) and from the fit (black squares). The gray band surrounding the data line represents the fit error. Figures from [69].

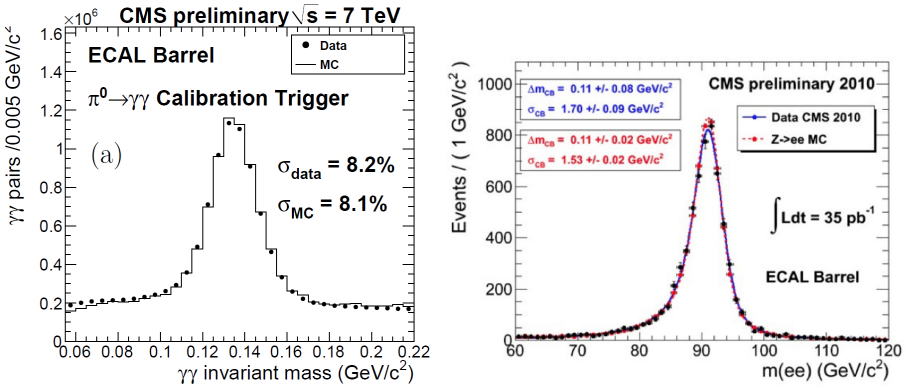

Figure 2.23: Performance of electromagnetic calorimeter. Left: Invariant mass distribution for photon pairs (barrel only). The plot was obtained after collecting only 18.7 nb^{-1} of data [71]. Right: Invariant mass distribution for $Z \to ee$ events in the ECAL Barrel detector. The distribution expected from simulation, corresponding to the same number of events is also shown.

2.3.7 Physics with Early Data: the Bose Einstein Correlation case

Early LHC data were also used to perform physics analysis, demonstrating the CMS detector reliability and understanding of its capabilities since the data-taking startup. During this thesis work, a study of the Bose-Einstein correlation (BEC) was pursued. It has been first measured in pp collisions at the LHC energies $\sqrt{s} = 0.9$ and 2.36 TeV [77], with data collected during the 2009 run. Later it was measured also with larger statistics from the

2010 run, at energies of $\sqrt{s} = 0.9$ TeV and at 7 TeV [78].

BEC measurement use interferometry of identical bosons, which is a powerful tool to investigate the space-time structure of sources emitting particles produced at different center-of-mass energies and from different initial systems. The effect manifests itself as a constructive interference at low values of the relative momentum of the pair, which can be expressed in a Lorentz-invariant form as $Q = \sqrt{-(p_1 - p_2)^2} = \sqrt{M^2 - 4m_\pi^2}$, where M is the invariant mass of the two particles, assumed to be pions with mass m_π. Experimentally, the BEC function is constructed as the ratio

$$R(Q) = (\mathrm{d}N/\mathrm{d}Q)/(\mathrm{d}N_{\mathrm{ref}}/\mathrm{d}Q) \tag{2.5}$$

of the Q distributions for pairs of identical bosons in the same event, and for pairs of particles in a reference sample not containing the BEC effect. In the measurements discussed here a mixed reference sample was used, which is the most commonly adopted in femtoscopic analyses. Such sample was constructed by pairing equally charged particles from different events that have similar charged-particle multiplicities in the same pseudorapidity regions.

Charged particles are required to have $|\eta| < 2.4$ and $p_T > 200$ MeV, ensuring that particles emitted from the interaction region cross all three barrel layers of the pixel detector and thus have good two-track separation. To achieve a high purity of the primary track selection, the trajectories are required to be reconstructed in fits with more than five degrees of freedom (N_{dof}) and $\chi^2/N_{\mathrm{dof}} < 5.0$.The transverse impact parameter with respect to the collision point is required to satisfy $|d_{xy}| < 0.15$ cm. to be less than 0.15 cm. The innermost measured point of the track must be within 20 cm of the beam axis, in order to reduce contamination from electrons and positrons from photon conversions in the detector material and secondary particles from decay of long-lived hadrons. (K^0_S, Λ, etc.).

The results briefly summarized here correspond to the $\sqrt{s} = 0.9$ and 7 TeV data taken during low-intensity runs, with 51.7 million tracks selected in the total of 2.7 million events. All pairs of same-sign charged particles with Q between 0.02 and 2 GeV are used for the measurement. The Q resolution in the signal region is better than 10 MeV. The effect of Coulomb interactions between charged particles is pairwise corrected using the Gamow factor [79]. The correlation function represented by the ratio $R(Q)$ is frequently fitted by superimposing the parameterization

$$R(Qr) = C\,[1 + \lambda\Omega(Qr)] \cdot (1 + \delta Q). \tag{2.6}$$

When space-time and momentum correlations in the system formed in the collisions are not significant, $\Omega(Qr)$ is given by the modulus square of a Fourier transform of the space-time region emitting bosons with overlapping wave functions, characterized by an effective size r. A Gaussian function, $\Omega(Qr) = e^{-(Qr)^2}$, or an exponential form, $\Omega(Qr) = e^{-Qr}$, are commonly adopted. Some deviations from the idealized picture are taken into account in Eq. 2.6 by the intercept parameter λ, reflecting the BEC strength for incoherent boson

emission from independent sources, the δ factor, for accounting for long-range momentum correlations, and C is a normalization factor. Furthermore, for reducing possible biases in the construction of the reference sample, a double ratio

$$\mathcal{R}(Q) = \frac{R}{R_{\rm MC}} = \left(\frac{{\rm d}N/{\rm d}Q}{{\rm d}N_{\rm ref}/{\rm d}Q}\right) \Big/ \left(\frac{{\rm d}N_{\rm MC}/{\rm d}Q}{{\rm d}N_{\rm MC,\,ref}/{\rm d}Q}\right) \tag{2.7}$$

is defined, where the subscripts "MC" and "MC,ref" refer to the corresponding distributions from the Monte Carlo simulations, generated without BEC effects, obtained using PYTHIA. More details can be found in Refs. [77, 78].

The double ratio is shown in Fig. 2.24(a) for $Q > 0.02$ GeV, with the correlation function fitted with the exponential parametrization, $\Omega(Qr) = e^{-Qr}$, in $\mathcal{R}(Q) = R(Qr)$ from Eq. 2.6. The fitted values correspond to $r({\rm fm}) = 1.89 \pm 0.02({\rm stat}) \pm 0.19({\rm syst})$, and $\lambda = 0.618 \pm 0.009({\rm stat}) \pm 0.039({\rm syst})$, which are strongly correlated, with correlation coefficients of about 86%. The Gaussian parameterizations, $\Omega(Qr) = e^{-(Qr)^2}$, used in several experiments was also analysed, but provided values of $\chi^2/N_{\rm dof} > 9$.

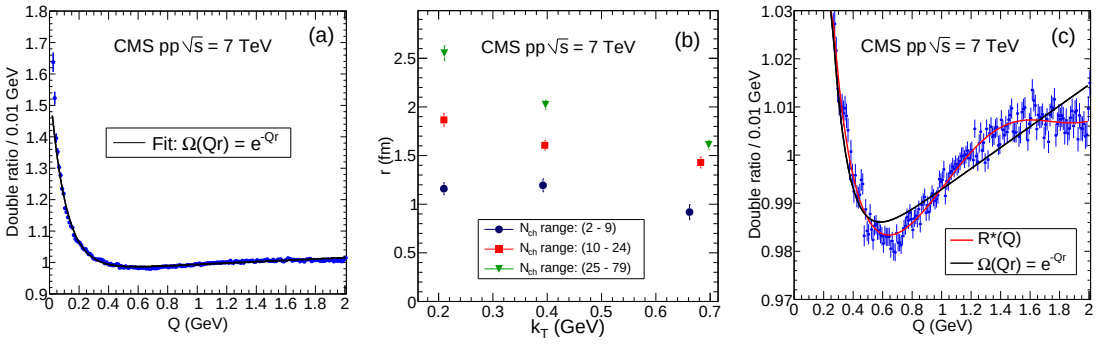

Figure 2.24: Data points for the double ratio are shown in (a), together with the fit given by the exponential parameterization in Eq. 2.6. Part (b) shows the behavior of the r parameter obtained with this $\Omega(Qr) = e^{-Qr}$ form as a function of k_T for three bins in $N_{\rm ch}$. The plot in (c) shows the anticorrelation structure in the double ratio [note the zoomed ordinate axis with respect to the plot of part (a)]. The uncertainties in the plots are statistical only. Figures from [78].

In Fig. 2.24(b) results for the r parameter fitted with $\Omega(Qr) = e^{-Qr}$ in Eq. 2.6 is shown as a function of the average transverse momentum of the pair, $k_T = (k_{1_T} + k_{2_T})/2$, for three different bins of charged multiplicity, $N_{\rm ch}$. The points are presented at the position corresponding to the mean value of k_T in the considered interval of $N_{\rm ch}$. The effective radius, r, is observed to steadily increase with $N_{\rm ch}$. It can be seen that r is approximately independent of k_T in the smaller multiplicity range, but clearly decreases with increase k_T for larger charged multiplicity events. A dependence on $k_{\rm T}$ has been observed at the SPS,at the Tevatron and at RHIC [80],where it is associated with the system collective behavior.

Similar results in pp collisions are seen by ALICE Collaboration[81].

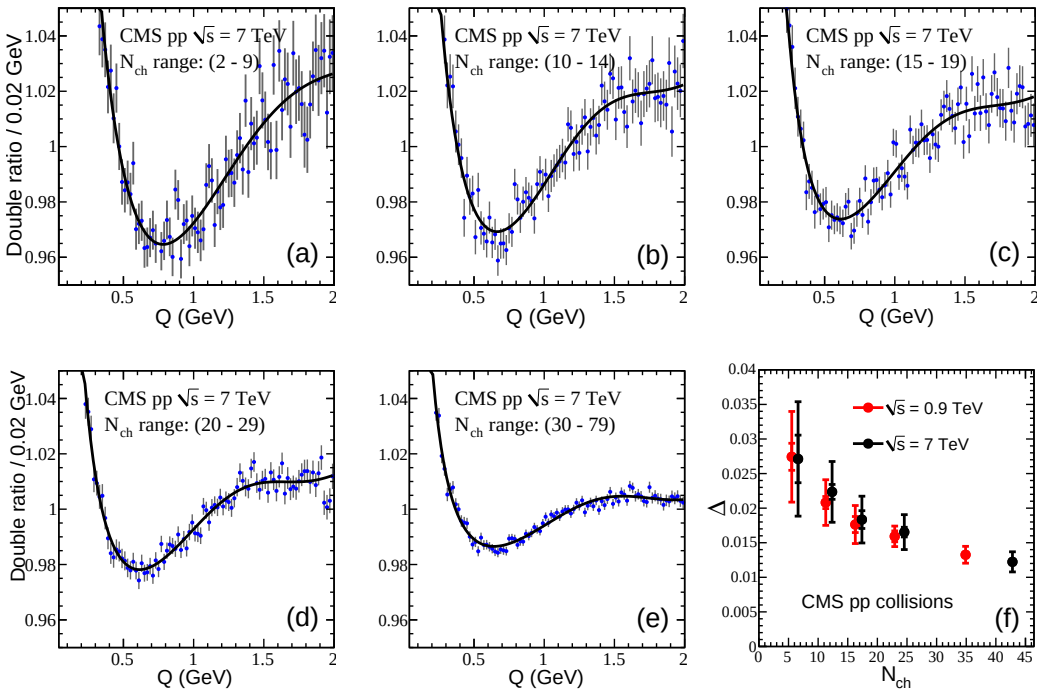

Figure 2.25: A decrease in the anticorrelation structure (dip) for increasing charged multiplicity is shown in parts (a) to (e). In (f), the dip's depth is shown in terms of the parameter $\Delta = C(1+\delta Q) - R^*(Q)$, at the minimum. Figures from [78].

Although the parameterization $\mathcal{R}(Qr)$ with the exponential form, $\Omega(Qr) = e^{-Qr}$, in Eq. 2.6 could describe the overall behavior of the data, it resulted in $\chi^2/N_{\rm dof} = 739/194$ for the $\sqrt{s} = 7$ TeV data and $\chi^2/N_{\rm dof} = 485/194$ for the $\sqrt{s} = 0.9$ TeV data (more details in Ref. [78]). This poor quality fit is originated in an anticorrelation (dip with $\mathcal{R} < 1$) observed in the double ratio at both energies, and with any choice of reference sample and MC simulation. This shown in Fig. 2.24(c), corresponding to the plot in Fig. 2.24(a) with a zoomed ordinate axis. The fit with $\Omega(Qr) = e^{-Qr}$ shows a deviation from the data trend around the minimum ($Q \sim 0.7$ GeV) and for $Q \geq 1.8$ GeV. The other curve in Fig. 2.24(c) was generated by a parameterization of the correlation function proposed in [82] for describing point-like interactions, such as in e^+e^- collisions (such a structure was observed in e^+e^- collisions at LEP [83]), i.e.,

$$R^*(Q) = \mathcal{R}(Qr) = C\left[1 + \lambda(\cos\left[(r_0 Q)^2 + \tan(\alpha\pi/4)(Qr_\alpha)^\alpha\right] e^{-(Qr_\alpha)^\alpha})\right] \cdot (1+\delta Q). \quad (2.8)$$

This parameterization describes the time evolution of the source by means of a one-sided asymmetric Lévy distribution. The parameter r_0 is related to the proper time of the onset of particle emission, r_α is a scale parameter, and α corresponds to the Lévy index of

stability. Fits obtained with Eq. 2.8 are of good quality, with $\chi^2/N_{\rm dof} = 215/192$ and $\chi^2/N_{\rm dof} = 213/192$ at 7 TeV and 0.9 TeV, respectively.
The depth in this anticorrelation region was investigated as a function of $N_{\rm ch}$, and is found to decrease consistently with this variable as can be seen from the plots in parts Fig. 2.25(a)-(e). The depth of the dip was also quantified as the difference, Δ, between the baseline curve defined as $C \cdot (1 + \delta Q)$ and the value of $\mathcal{R}(Q)$ defined by Eq. 2.8 as $R^*(Q)$, at its minimum. It is shown in Fig. 2.25(f) as a function of $N_{\rm ch}$, for both $\sqrt{s} = 0.9$ TeV and 7 TeV. This detailed observation is made possible by the large data samples studied, and constitutes the first evidence of this effect in proton-proton collisions.

Chapter 3

Heavy Flavour Physics

Heavy quark production is an important research domain at the LHC, since these particles are abundantly produced at previously unreached center-of-mass energy enabling precision measurements to improve our understanding of heavy flavor physics. In the following the term *heavy* will be effectively referred both to charm (c) and beauty (b) quarks, since the up, down and strange quark (u, d, s) masses are significantly lower and the top quark (t) has an extremely short lifetime such that is not able to hadronize before to decay.
Heavy quark production is interesting per se as it presents a key process for the study of the theory of strong interactions, Quantum Chromodynamics (QCD). Furthermore, a well-established understanding of heavy quark production is needed for many searches at the LHC.

In this Chapter the theoretical concepts relevant to describe the physics of heavy quarks at the LHC are summarized. The main ideas of QCD are resumed, before their application to high-energy hadron-hadron collisions is discussed. This includes the factorization ansatz, the evolution of the parton distribution functions, the partonic processes important for beauty quark production and the phenomenological treatment of heavy quark fragmentation. A further section is dedicated to the description of the decay of b-hadrons via the weak interaction. The Monte Carlo event generators which are used to produce theoretical predictions within the QCD framework are presented in the last section. Finally, the reliability of the inclusive b cross section calculations is discussed.

3.1 QCD

A scale dependent (running) coupling $\alpha_s(Q^2)$ and a renormalization scale μ have been introduced in the first Chapter in the QCD framework. The running of the coupling is needed to remove ultraviolet divergences appearing in the calculation. A summary of measurements of $\alpha_s(Q^2)$ as a function of the respective energy scale Q is presented in Fig. 3.1. At the scale set by the mass of the Z boson the average value of the strong coupling constant is $\alpha_s(M_Z) = 0.1184 \pm 0.0007$ [84]. The renormalization scale is used to set the validity limit

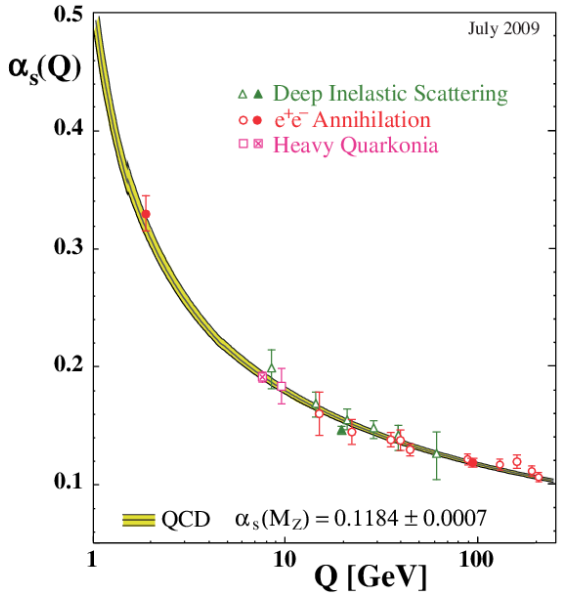

Figure 3.1: Summary of measurements of α_s as a function of the respective energy scale [84].

of the perturbative approach, is usually defined as Λ_{QCD} and experimentally is found to be of the order of 200 MeV [85]. At energy scales below Λ_{QCD} the strong coupling rises to infinity, resulting in the confinement of quarks and gluons inside color-singlet hadrons. The use of a perturbative approach is instead legitimate at scales $Q^2 \gg \Lambda_{QCD}$.

Quarks and gluons are not seen in experiments, instead they are transformed into observable hadrons in a process called fragmentation, which cannot be computed in a perturbative way. Nonetheless perturbative calculations are proven to be successful in the prediction of inclusive hadronic cross sections at sufficiently large energy scales. The reason is that the hadronization occurs at a significantly later time scale ($t \sim \frac{1}{\Lambda_{QCD}}$) than the production process ($t \sim \frac{1}{Q}$) and therefore does not alter the probability of the primary process to happen. This is the basis of the factorization approach described below.

3.2 Hadronic Collisions at High Q^2

Due to the asymptotic freedom in QCD, the interaction between quarks and gluons becomes arbitrarily weak at short distances. Consequently hadrons behave as collections of free parton at large transferred momenta and their interaction can therefore be described using a parton model.

3.2.1 Event kinematics

A generic hard scattering process of two hadrons (h_1, h_2) with four-momenta P_1 and P_2, respectively, is illustrated in Fig. 3.2. The scattering process is caused by the interaction

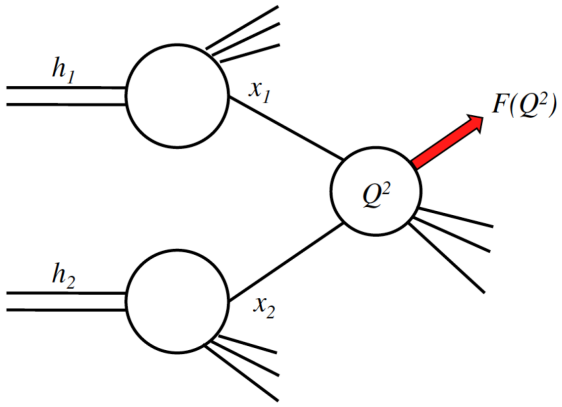

Figure 3.2: Scattering process of two hadrons h_1 and h_2 in the parton model. Two partons with momentum fractions x_1 and x_2 undergo an hard interaction at the scale Q^2.

of two parton constituents of the initial hadrons with four-momentum $p_1 = x_1 P_1$ and $p_2 = x_2 P_2$. Since the center-of-mass of the partonic interaction is normally boosted with respect to the laboratory frame, it is useful to classify the final state according to variables that are invariant under longitudinal boosts. The squared center-of-mass energy of the hadronic system is:

$$s = (P_1 + P_2)^2. \tag{3.1}$$

In the massless limit, the virtuality of the process is defined as:

$$Q^2 = \hat{s} = x_1 x_2 s. \tag{3.2}$$

The momentum imbalance of the partons participating to the hard interaction is reflected in the rapidity distribution of the outgoing particles. The transverse momentum of the outgoing partons in the center-of-mass frame of the colliding partons is denoted by $\hat{p}_T$ and is of particular interest for the Monte Carlo event generators, as will be discussed in the next Sections.

3.2.2 Factorization

Soft processes resulting in the production of low momentum hadrons are the most common events in proton-proton collision at the LHC. Although these processes are QCD related, they cannot be calculated by pQCD. Perturbative approaches only lead to reliable results if a hard scale is present in the interaction. In the case of heavy flavor physics, the hard scale is provided by the mass of the heavy quark, its transverse momentum or the virtuality of the

process. Most of the processes calculated by pQCD feature infrared divergences emerging from real gluon emission. Singularities arise either if a gluon is emitted in the direction of the outgoing parton (collinear divergences) or if a low momentum gluon is emitted (soft divergence).

Similar to the ultraviolet divergences which are removed by introducing the renormalization scale μ_R, the infrared divergences can be absorbed when imposing the factorization scale μ_F. The factorization scale can be thought of as the scale which separates the short- and the long-distance Physics. The short-distance part covers the hard process calculable in pQCD, while the long-distance part includes the collinear and soft divergences which are not accessible to perturbative calculations. The factorization ansatz is validated by the factorization theorem [86, 87, 88]. According to the factorization theorem the cross section for a hard scattering originating from an interaction of two hadrons with four-momenta P_1 and P_2 can be written as

$$\sigma(P_1, P_2) = \sum_{i,j} \int dx_1 dx_2 f_i^{h_1}(x_1, \mu_F^2) f_j^{h_2}(x_2, \mu_F^2) \hat{\sigma}_{i,j}(x_1 P_1, x_2 P_2, \alpha_s(\mu_R), Q^2; \mu_F^2, \mu_R^2), \quad (3.3)$$

where:

- $f_i^h(x, \mu_F^2)$ is the parton distribution function (PDF) for the parton i in the hadron h,
- x_1 is the momentum fraction of the hadron h_1 carried by the parton i,
- x_2 is the momentum fraction of the hadron h_2 carried by the parton j,
- $\hat{\sigma}_{i,j}$ is the short-distance scattering cross section of partons i and j,
- μ_R is the renormalization scale, and
- μ_F is the factorization scale.

The parton distribution functions $f_i^h(x, \mu_F^2)$ describe the probability of extracting a parton i from a hadron h with momentum fraction x. Hence, the factorization theorem implies that the probability of extracting the parton can be treated independently from the parton undergoing an interaction. This assumption was successfully verified in deep inelastic lepton-hadron scattering (DIS) which is characterized by a large virtuality ($Q^2 \gg \Lambda_{QCD}$). In the DIS regime, the factorization theorem is proven to be valid to all orders in perturbation theory [88]. Nonetheless it is not obvious that the factorization theorem can be adapted to hadron-hadron collisions since gluons from the hadron remnant might interact and spoil the factorization. Explicit calculations have shown that factorization breaking effects are present but are suppressed by powers of Λ_{QCD}/Q^2 in the high energy limit [89]. The partonic short-distance cross section $\hat{\sigma}_{i,j}$ can be computed in pQCD as

$$\hat{\sigma}_{i,j} = \alpha_s^k \sum_n \left(\frac{\alpha_s}{\pi}\right)^n c_{ij}^{(n)} \quad (3.4)$$

were the coefficients $c^{(n)}$ are functions of the kinematic variables and the factorization scale. Different hard processes will contribute with different leading powers k to the partonic cross section.

3.2.3 Evolution of Parton Distribution Functions

As discussed in the previous section the long-distance, non-perturbative part of the cross section is absorbed in scale dependent PDFs which cannot be calculated by pQCD. Nevertheless, the dependence on the factorization μ_F is described by perturbative calculation. The pQCD parton evolution equations predict the evolution of the PDFs to any scale $Q^2 > Q_0^2$ once $f_i^h(x, Q_0^2)$ is known at a starting scale Q_0^2. The scale dependence of the PDFs is a consequence of gluon radiation and gluon splitting effects, which are incorporated in the DGLAP evolution equations [90, 91, 92, 93] for the quark ($q_i(x, Q^2)$) and gluon ($g(x, Q^2)$) PDFs:

$$\frac{dq_i(x,Q^2)}{d\log Q^2} = \int_x^1 \frac{dy}{y}\left(q_i(y,Q^2)P_{qq}\left(\alpha_s(Q^2),\frac{x}{y}\right) + g(y,Q^2)P_{qg}\left(\alpha_s(Q^2),\frac{x}{y}\right)\right) \quad (3.5)$$

$$\frac{dg(x,Q^2)}{d\log Q^2} = \int_x^1 \frac{dy}{y}\left(\sum_i q_i(y,Q^2)P_{gq}\left(\alpha_s(Q^2),\frac{x}{y}\right) + g(y,Q^2)P_{gg}\left(\alpha_s(Q^2),\frac{x}{y}\right)\right) \quad (3.6)$$

where the sum $i = 1, ..., 2n_f$ runs over quarks and antiquarks of all flavors. The functions $P_{ab}(\alpha_s(Q^2), z)$ are called splitting functions and represent the probability to find a parton a in a parton b at the scale Q^2 with a momentum fraction z. The splitting functions are calculable using a perturbative expansion in α_s. The diagrams contributing to the leading order splitting functions are shown in Fig. 3.3.

In practice the PDFs used for calculations in the LHC energy regime are obtained by evolving the PDFs measured in fixed target experiments and in electron-proton scattering at HERA. The standard procedure is to first parametrize the x dependence of the PDFs at a fixed input scale Q_0^2 and then extrapolate the function to the desired scale Q^2 according to the DGLAP equations. Several groups have performed PDF fits to the data obtained in DIS experiments, for example the CTEQ [94], MRST [95], MSTW [96] and NNPDF [97, 98] groups. The quark and gluon distribution functions measured at HERA at $Q^2 = 10$ GeV are shown in Fig. 3.4.

3.3 Heavy Quark Production

The leading-order (LO) process for the production of a heavy quark Q with mass m_Q in hadronic collisions is flavor creation, i.e. quark-antiquark annihilation and gluon-gluon fusion

$$q\bar{q} \to Q\bar{Q} \quad \text{and} \quad gg \to Q\bar{Q}. \quad (3.7)$$

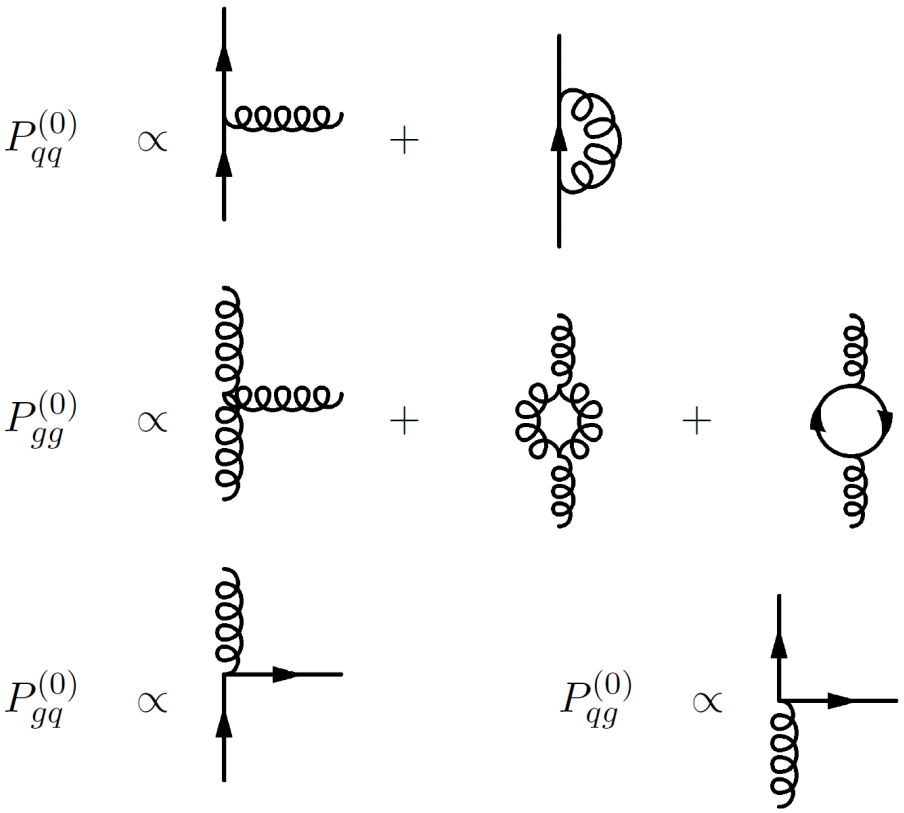

Figure 3.3: Feynman diagrams contributing to the leading order splitting functions.

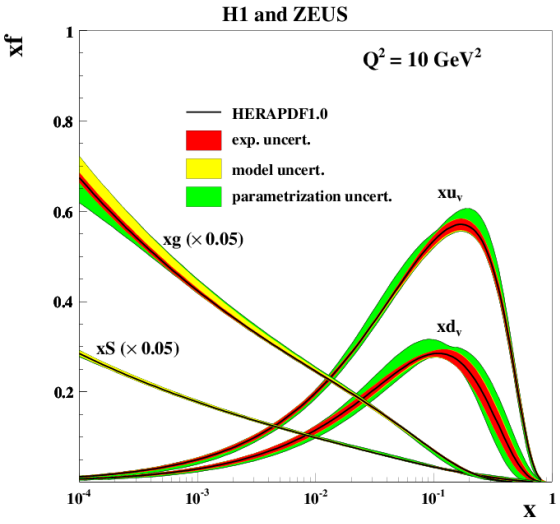

Figure 3.4: The proton parton distribution functions measured at HERA at $Q^2 = 10$ GeV, for valence quarks xu_v and xd_v, sea quarks xS, and gluons xg. The gluon and sea distributions are scaled down by a factor 20 [99].

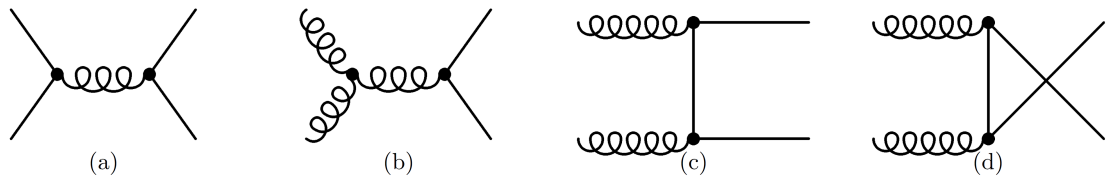

Figure 3.5: Leading order diagrams for heavy-quark pair production: (a) quark-antiquark annihilation $q\bar{q} \to Q\bar{Q}$, (b)-(d) gluon-gluon fusion $gg \to Q\bar{Q}$.

The corresponding diagrams are shown in Fig. 3.5.
When evaluating these diagrams and integrating over the two-body phase space the total partonic cross section at LO in perturbation theory can be obtained [100, 101, 102]. The large energy limit of the partonic cross section is

$$\hat{\sigma}(q\bar{q} \to Q\bar{Q}) \simeq \frac{1}{\hat{s}}\hat{\sigma}(gg \to Q\bar{Q}) \simeq \frac{1}{\hat{s}}\left(\frac{1}{\beta}\log\left(\frac{1+\beta}{1-\beta}\right) - 2\right) \tag{3.8}$$

where $\hat{s}$ is the center-of-mass energy available in the partonic system and $\beta \equiv \sqrt{1 - \frac{4m_Q^2}{\hat{s}}}$ is the velocity of the heavy quark. The quark annihilation process vanishes more quickly at high $\hat{s}$ thus gluon-gluon fusion is the dominant process for heavy quark production at the LHC. In flavor creation processes, the final states involving the heavy quarks are observed back-to-back with little combined transverse momentum.

At next-to-leading order (NLO), contributions of real and virtual emission diagrams have to be taken into account. In addition, heavy quarks can be produced in flavor excitation processes and gluon splitting events (Fig. 3.6).

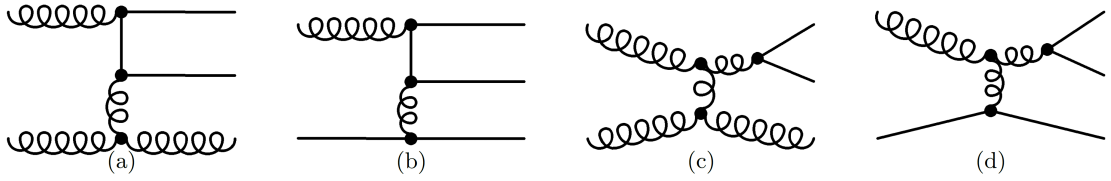

Figure 3.6: Next-to-leading order diagrams for heavy-quark pair production: (a),(b) flavor excitation; (c),(d) gluon splitting.

Calculations have been performed in [103, 104]. In the flavor excitation process, the heavy quark is considered to be already present in the incoming hadron. It is excited by the exchange of a gluon with the other hadron and appears on mass-shell in the final state. Since the heavy quark is not a valence quark it must originate from a pair production process $g \to Q\bar{Q}$. In most PDF parametrizations the heavy-flavor contributions are assumed to vanish for $Q^2 < m_Q^2$, the hard scattering in flavor excitation processes must therefore have a virtuality above m_Q^2. The heavy quark final states do not need to be back-to-back as the third parton can carry away some transverse momentum. In gluon splitting events the

heavy quark occurs in $g \to Q\bar{Q}$ events in the initial- or final-state shower. The resulting heavy flavored final state can carry a large combined transverse momentum and thus be concentrated within a small cone of angular separation.

Some correlated variables between simulated b-quark pairs produced from proton collisions at 10 TeV [105] are shown in Fig. 3.7, divided by production process. They are the opening angle $\Delta\phi$ between the quarks in the transverse plane perpendicular to the proton beam line, the opening angle between the quarks with respect to the beam line $\Delta\eta$, and the momentum asymmetry in the transverse plane $\delta p_T = \frac{|p_{T_1} - p_{T_2}|}{p_{T_1} + p_{T_2}}$.

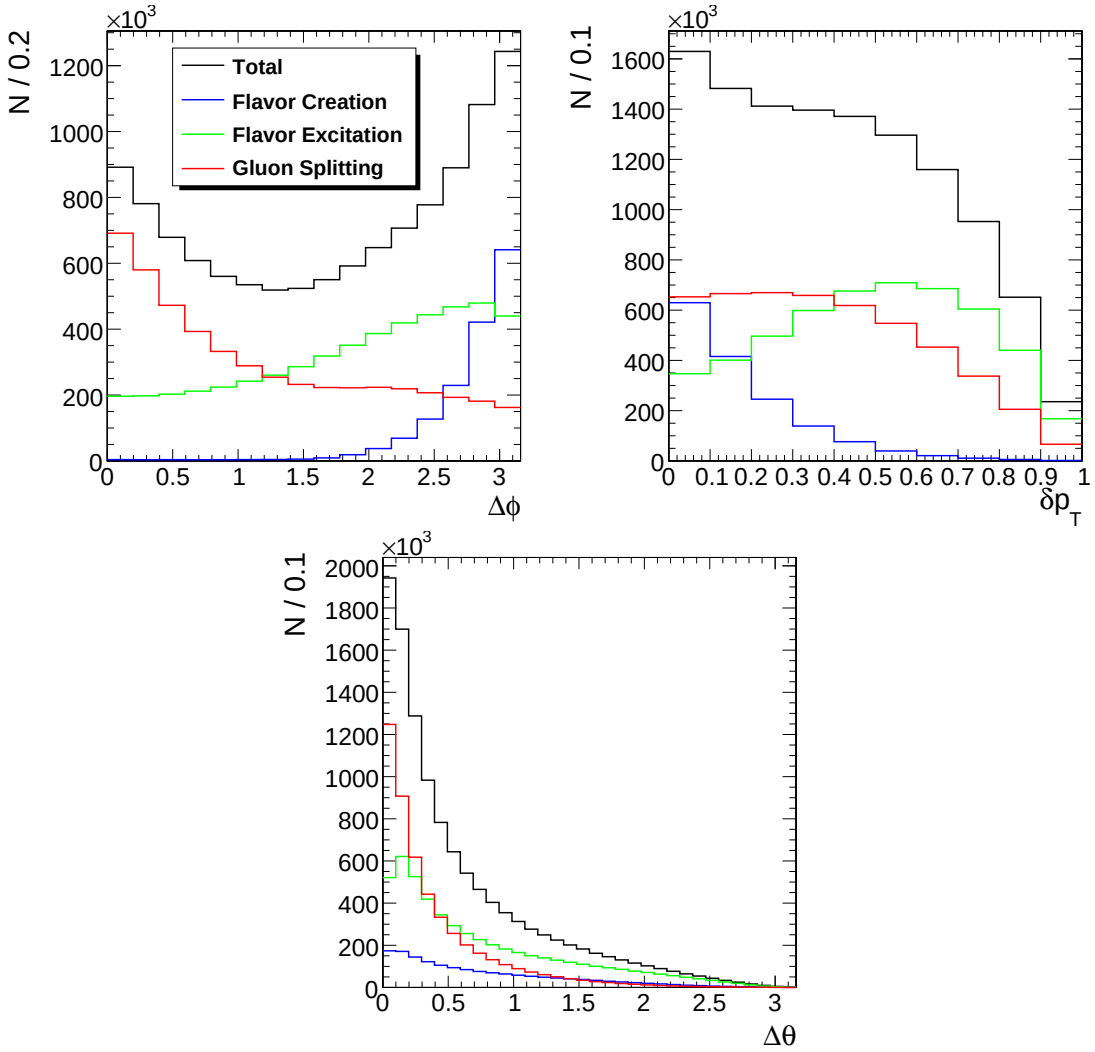

Figure 3.7: Correlated variables between simulated b-quark pairs produced from proton collisions at 10 TeV are also shown for the different mechanisms [105]: $\Delta\phi$ (top left), $\Delta\eta$ (top right), and the quark momentum asymmetry in the transverse plane δp_T (bottom).

3.4 The Fragmentation of Heavy Quarks

The heavy quarks produced in the hard interaction are not visible in the detector due to color confinement. Instead the quarks fragment into color-singlet hadrons which then conglomerate in a collimated particle jet. As discussed in Section 3.1, the fragmentation process happens on a larger time scale compared to the hard process and thus can be treated independently.

Since the value of the coupling α_s rises strongly at large distances, the fragmentation process cannot be calculated from first principles in pQCD and phenomenological models have to be applied. The probability to produce a hadron h from a heavy quark Q can be split in a short- and a long-range part [106]:

$$D_Q^h(z, \mu_F) = \int_z^1 D_Q(x, \mu_F) D_Q^h(\frac{z}{x}) dx. \tag{3.9}$$

The short-distance, perturbative part $D_Q(x, \mu_F)$ models the evolution of a quark produced off-shell at the scale μ_F via gluon emissions to a quark on its mass shell. This is what is usually implemented in the parton shower algorithms of the Monte Carlo simulation programs. A parton shower develops through successive splitting until the perturbative approach becomes unreliable (Λ_{QCD}). The parton shower represents an approximative perturbative treatment of QCD dynamics based on the DGLAP evolution equations. It improves the fixed order pQCD calculation by taking into account soft and collinear enhanced terms to all orders. The set of partons in the low-momentum-transfer, long-distance regime produced in the parton shower is transformed into hadrons with the aid of phenomenological fragmentation functions $D_Q^h(z)$.

At present different models of the hadronization process exist among which the string and cluster fragmentation models are of interest for the analysis presented here. Under the assumption of factorization, the fragmentation functions do not depend on the hard scattering process. Hence, the fragmentation functions are universal and the models tuned for e^+e^- and ep collision data can also be applied to the LHC data. The string fragmentation model assumes linear confinement. In a physical picture, a color flux tube stretches between the $q\bar{q}$ pair as it starts to move apart. The potential energy stored in the string increases and the string may break by the production of a new quark pair $q_1\bar{q}_1$, so that the system splits into two color-singlet systems $q\bar{q}_1$ and $q_1\bar{q}$. If the invariant mass of either of these string pieces is large enough, further breaking might occur. Gluons are supposed to produce kinks on the strings which modifies the angular distribution of the hadrons inside the jet. The fragmentation function $D_Q^h(z)$ determines the energy and the longitudinal momentum of the hadrons.

The most widely used formula for modeling the fragmentation of heavy quarks is the Peterson fragmentation function [107]. The probability that the hadron receives a mo-

mentum fraction z from the quark is given by:

$$D_Q^h(z,\mu_F) \propto \frac{1}{z\left(1-\frac{1}{z}-\frac{\varepsilon_Q}{1-z}\right)^2}, \tag{3.10}$$

where ε_Q is a free parameter that has to be measured in experiments. It is expected to scale between flavors like $\varepsilon_Q \propto 1/m_Q^2$. The values of the Peterson parameter for charm and beauty quarks extracted from electron-positron collision data are listed in table 3.1.

	$\sqrt{s}[GeV]$	LO (α_s)	NLO (α_s)
ε_c	10.5	0.058	0.035
ε_c	91.2	0.078	0.040
ε_b	91.2	0.0069	0.0033

Table 3.1: Peterson parameter for charm and beauty quarks extracted from electron-positron collision data at a center of mass energy $\sqrt{s}$. The parameters have been determined at LO and NLO [106].

Although the Peterson function is widely used, several alternatives have also been proposed. The model of Collins and Spiller [108] gives

$$D_Q^h(z,\mu_F) \propto \left(\frac{1-z}{z}+\frac{(2-z)\tilde{\varepsilon}}{(1-z)}\right)(1+z^2)\left(1-\frac{1}{z}-\frac{\tilde{\varepsilon}}{1-z}\right)^{-2}, \tag{3.11}$$

with $\tilde{\varepsilon}$ as an adjustable model parameter.
Kartvelishvili *et al.* [109] give the functional form

$$D_Q^h(z,\mu_F) \propto z^\alpha(1-z) \tag{3.12}$$

with α as a free model parameter.
The Lund symmetric model [110] gives

$$D_Q^h(z,\mu_F) \propto \frac{1}{z}(1-z)^a \exp\left(-\frac{bM_T^2}{z}\right) \tag{3.13}$$

with a and b as free parameters and M_T^2 the square of the transverse mass of the heavy-light quark system[1].

The fragmentation functions obtained for the c- and b-quark with the Peterson model, as well as those obtained for the b-quark with the different models, are reported in Fig. 3.8. The harder fragmentation of b quarks is explained by their large mass. When binding a light quark to the heavy b-quark, the resulting hadron decelerates only slightly so that the b-quark and the hadron have almost the same momentum. In case of cluster fragmentation models

[1]Experimentally, the product bM_T^2 is taken as a free parameter

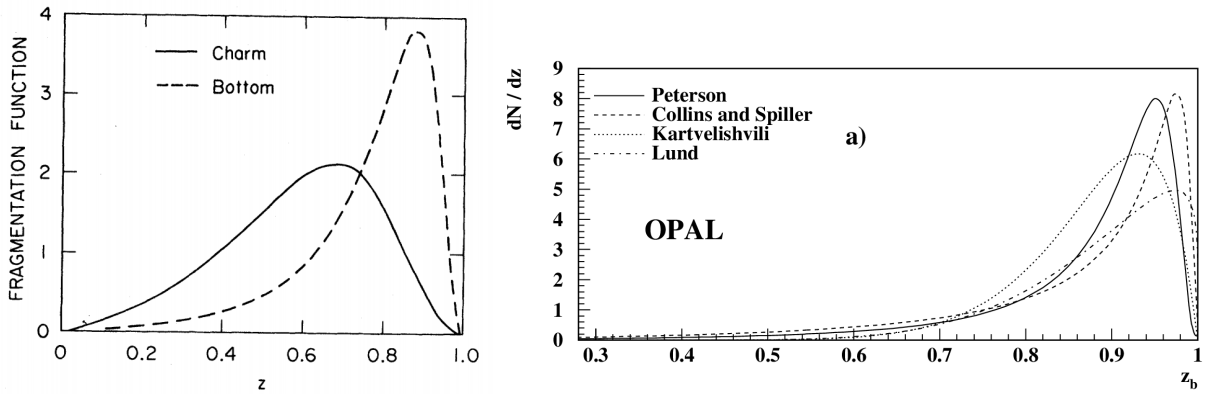

Figure 3.8: Left: Fragmentation functions for the c- and b-quark with the Peterson model, using $\varepsilon_c = 0.15$ and $\varepsilon_b = 0.15(m_c/m_b)^2 = 0.016$ [107]. Right: example of normalized fragmentation functions for the b-quark with model parameters as determined from fits to the LEP data by the OPAL collaboration [111].

color-singlet clusters of partons form after the perturbative phase of jet development and then decay into the observed hadrons. The clusters originate from gluon splitting in quark pairs and subsequent recombination with neighboring quarks and antiquarks. Afterward, the clusters are assumed to decay isotropically in their rest frame into pairs of hadrons, where the branching ratios are determined by the density of states.

3.5 Semileptonic Decays of Heavy Quarks

The presence of hadrons containing heavy quarks is deduced by the observation of their decay products. In a first approximation of b-flavored hadron decays, only the beauty quark participates in the transition while the other quark acts as a spectator quark. The b-quark can decay via the weak interaction into a W boson and c- or a u-quark. The charged current couplings for the flavor-changing transition between quarks are described in terms of the CKM matrix. The universality of the weak decay is reflected in the unitarity of the CKM matrix. Hence, the CKM matrix can be parametrized by three mixing angles and one irreducible phase which accounts for the CP-violation intrinsic to the weak decay in the Standard Model. The decay width is proportional to the squared CKM matrix element. Measurements of semileptonic decays of B mesons have shown that the matrix elements relevant for the weak decay of the b-quark are very small compared to other elements: $|V_{cb}| = 0.0412 \pm 0.0011$ and $|V_{ub}| = 0.00393 \pm 0.00036$ [112]. Consequently, the b-quark decay is highly suppressed and the b quark has a relatively large lifetime of $\tau \sim 10^{-12}$ s. Since $|V_{cb}|$ is about an order of magnitude larger than $|V_{ub}|$ the preferred decay is $b \to cW^-$ with a branching ratio larger than 95%.

The lifetime τ of a b-hadron is related to the average decay length as measured in the

laboratory, l, by:

$$l = \frac{p_B}{m_B} c\tau = \beta\gamma c\tau, \tag{3.14}$$

where p_B, m_B and $\beta\gamma$ are the particle's momentum, mass and boost, respectively. The distance of closest approach of the extrapolated muon track to the interaction point is defined as impact parameter d:

$$d = l \sin\delta = \beta\gamma c\tau \sin\delta, \tag{3.15}$$

where δ is the angle between the direction of the secondary track and the direction of the parent particle. Objects originating from a secondary vertex are generally characterized by a large transverse impact parameter (Fig. 3.9).

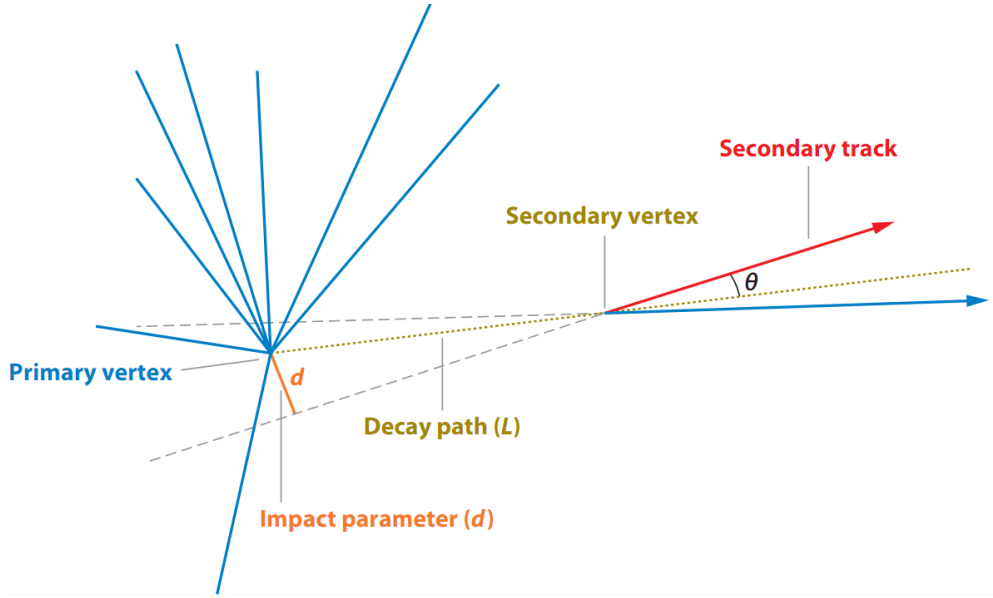

Figure 3.9: Illustration of the transverse impact parameter d of the decay products of a long-lived particle. The decay particles emerging from the secondary vertex are characterized by a large transverse impact parameter compared to that of the particles emerging from the primary vertex. Figure from [113].

The transverse impact parameter is then defined as

$$d_{xy} = d \sin\theta = \beta\gamma c\tau \sin\delta \sin\theta, \tag{3.16}$$

where θ is the polar angle between the hadron direction and the beam axis.
Properties of b-hadrons are listed in Table 3.2. Their mean decay length is $c\tau = 466$ μm. This transforms into an average observable decay length of $L = \beta\gamma c\tau = 3 - 5$ mm in the rest frame at the LHC which can be observed as a displaced (or secondary) vertex in the detector. In CMS a lifetime based tag of b-hadrons is possible thanks to the pixel detector

	quark content	mass m [MeV]	lifetime τ [ps]	decay length $c\tau$ [μm]	fraction
B^0	$d\bar{b}$	5279.50 ± 0.30	1.518 ± 0.007	455.1	0.403 ± 0.009
B^+	$u\bar{b}$	5279.17 ± 0.29	1.641 ± 0.008	492.0	0.403 ± 0.009
B_s^0	$s\bar{b}$	5366.3 ± 0.6	1.477 ± 0.022	442.8	0.103 ± 0.009
Λ_b^0	ubd	5620.2 ± 1.6	1.425 ± 0.032	427.2	0.090 ± 0.015
D^0	$c\bar{u}$	1864.80 ± 0.14	0.415 ± 0.004	124.4	0.557 ± 0.053
D^+	$c\bar{d}$	1869.57 ± 0.16	1.057 ± 0.015	316.9	0.233 ± 0.027
D_s^+	$c\bar{s}$	1968.45 ± 0.33	0.467 ± 0.017	140.0	0.103 ± 0.029
Λ_c^0	udc	2286.2 ± 1.6	0.206 ± 0.012	61.8	0.08 ± 0.05

Table 3.2: Properties of b-hadrons. The table shows the quark content, the mass, the lifetime and the decay length [27, 112, 114].

which achieves a track impact parameter resolution of $\mathcal{O}(20)$ μm. For comparison, also the properties of c-hadrons are listed in Table 3.2.
The W boson originating from the weak decay of the b-quark decays either hadronically or leptonically. Within this analysis the semileptonic decay of b quarks into muons is studied since the muon provides a clean signature which is relatively easy to detect experimentally. The decay $W^- \to \mu^- \bar{\nu}_\mu$ has a branching ratio of about 10%. In addition, about 10% of the subsequent charm decays also have a muon and a neutrino in the final state. The Feynman diagrams of the semileptonic decay of a b-hadron with a muon in the final state are illustrated in Fig. 3.10.

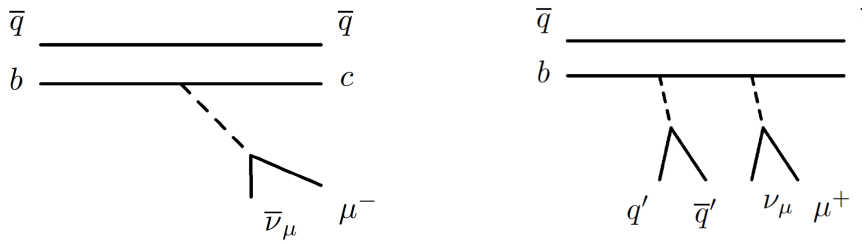

Figure 3.10: Weak decay of b-hadrons with a muon in the final state.

3.6 Monte Carlo Event Generators

Monte Carlo (MC) event generators provide an event-by-event prediction of complete hadronic final states based on QCD calculation. They allow the study of the topology of events generated in hadronic interactions and are used as input for detector simulation programs to investigate detector effects. The event simulation is divided into different stages as illustrated in Fig. 3.11.

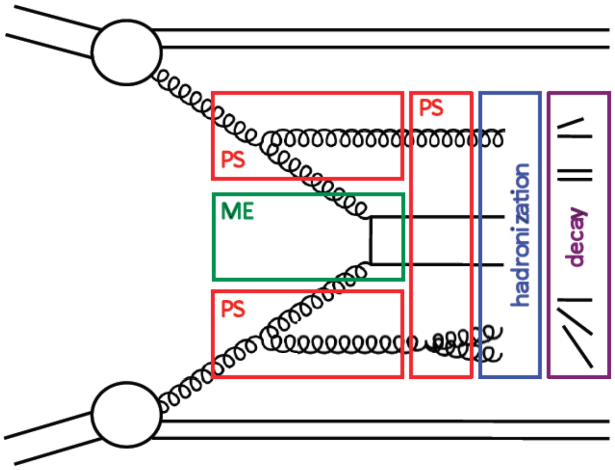

Figure 3.11: Schematic view of the subsequent steps of a MC event generator: matrix element (ME), parton shower (PS), hadronization and decay.

First, the partonic cross section is evaluated by calculating the matrix element in fixed order pQCD. The event generators presently available for the simulation of proton-proton collisions provide perturbative calculations for beauty production up to NLO. Higher order corrections due to initial and final state radiation are approximated by running a parton shower algorithm. The parton shower generates a set of secondary partons originating from subsequent gluon emission of the initial partons. It is followed by the hadronization algorithm which clusters the individual partons into color-singlet hadrons. In a final step, the short lived hadrons are decayed.

In the framework of the analysis presented in this thesis, the MC event generators PYTHIA 6.4 [115] and MC@NLO 4.0 [116] are used to compute efficiencies, kinematic distributions, and for comparisons with the experimental results. All programs were run with their default parameter settings, except when mentioned otherwise.

3.6.1 PYTHIA

In the PYTHIA program, the matrix elements are calculated in LO pQCD and convoluted with the proton PDF, chosen herein to be CTEQ6L1 [117]. The mass of the b-quark is set to $m_b = 4.8$ GeV. The underlying event is simulated with the Z2 and D6T tune [118]. Pile-up events were not included in the simulation. The parton shower algorithm is based on a leading-logarithmic approximation for QCD radiation and a string fragmentation model is applied. The longitudinal fragmentation is described by the Lund symmetric fragmentation function [110] for light, charm and beauty quarks. A dedicated heavy flavour production using the Peterson fragmentation function has been used for comparison purpose and systematic uncertainties estimation, as explained in the analysis Section.

3.6.2 MC@NLO

The MC@NLO package [116] has a NLO matrix element calculation interfaced to the parton shower algorithms of the HERWIG [119] package, which incorporates color coherence effects in the final state and initial state parton showers, as well as in heavy quark processes and the hard process generation. The method has the following features: fully exclusive events are generated, with hadronization according to HERWIG; total exclusive rates are accurate to NLO; NLO results for distributions are recovered upon expansion in α_S; hard emissions are treated as in NLO computations while soft/collinear emissions are handled by HERWIG, with the same logarithmic accuracy as HERWIG; and matching between the hard- and soft/collinear-emission regions is smooth. The mass of the b-quark is set to $m_b = 4.75$ GeV. The CTEQ6M PDF sets were used to generate the MC@NLO events. The events generated with MC@NLO are studied only at the generator level and are not passed through the detailed detector simulation.

3.7 Reliability of the Inclusive b Cross Section Calculations

An interesting way of understanding the production mechanism of heavy flavours is to consider the cross section of jets that contain a heavy quark [120]. It can be defined as the differential p_T spectrum integrated within a fixed rapidity range and above a given p_T threshold (p_T^{min}):

$$\sigma(p_T^{min}) = \int_{|y|<y_{max}} d\,y \int_{p_T>p_T^{min}} d\,p_T \frac{d^2\sigma}{dy\,dp_T} \,. \tag{3.17}$$

Several algorithms can be used to define a jet such as particles clustered in cones of radius R in the pseudorapidity–azimuthal angle plane. In practice, most features discussed here are insensitive to the choice of algorithm.

Using the parton-level Monte Carlo MCFM [121] it is possible to compute the ratio between NLO and LO predictions (hereafter referred to as K-factor) for the Tevatron Run II ($p\bar{p}$, $\sqrt{s} = 1.96$ TeV, left) and for the LHC (pp, $\sqrt{s} = 14$ TeV, right) [122]. The results are shown in the top panels of Fig. 3.12. The K-factor is considerably larger than one, indicating that the perturbative series is very poorly convergent. This implies that the NLO result cannot be an accurate approximation to the full calculation.

The possibility that higher-order corrections may be very large has been pointed out early on in ref. [123] for Tevatron energies. Two different sources can be found. The first are small-x effects which are relevant in the low-p_T domain, arising due to the presence, starting from $\mathcal{O}(\alpha_s^3)$, of diagrams where a gluon exchanged in the t channel becomes soft. Results of the calculations [124] however suggest that they are negligible at the current collider energies. The second source arises because potentially large higher-order corrections appears also

when b quarks are produced at high transverse momentum. In this regime the b-quark behaves more and more like a massless particle, radiating an increasingly large amount of its energy in the form of hard, collinear gluons. This physical phenomenon is associated with the presence of logarithms of the form $\log(p_T/m)$, which appear at all orders in perturbation theory, and has been examined in ref. [125].

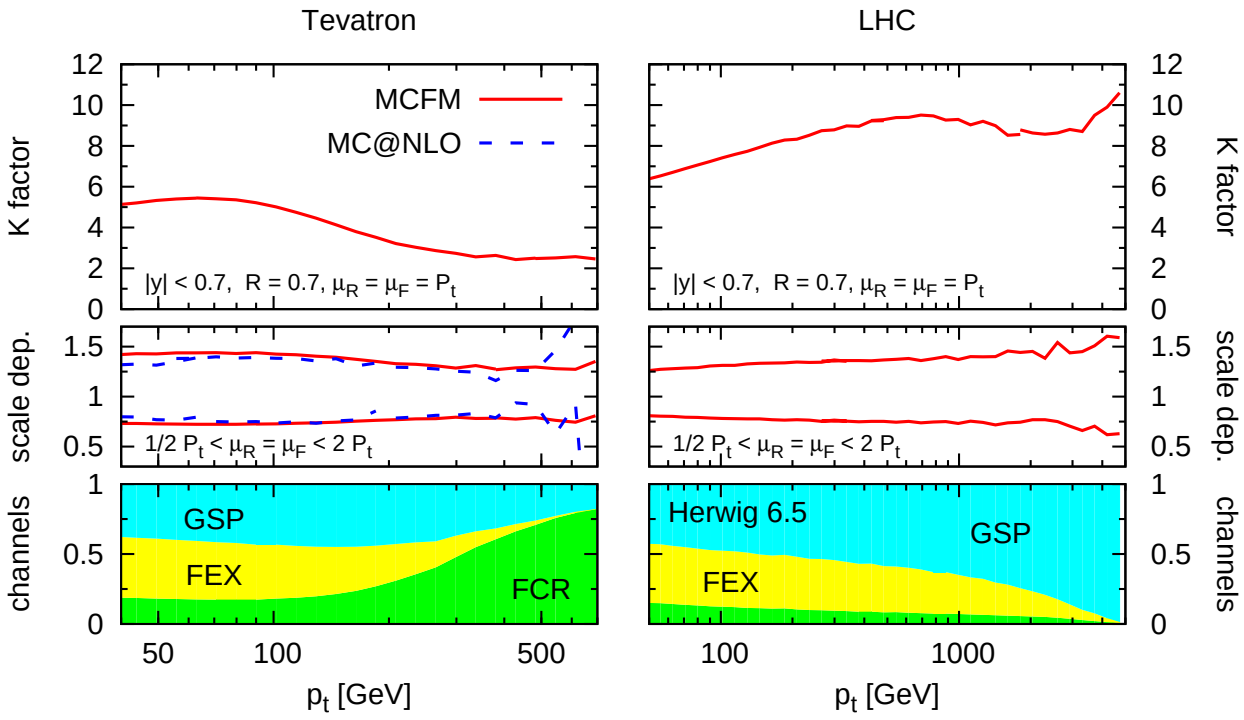

Figure 3.12: Top: K-factor for inclusive b-jet spectrum as computed with MCFM, clustering particles into jets using the k_t jet-algorithm with R=0.7, and selecting jets in the central rapidity region ($|y| < 0.7$). Middle: scale dependence obtained by simultaneously varying the renormalization and factorization scales by a factor two around p_T, the transverse momentum of the hardest jet in the event. Bottom: breakdown of the HERWIG inclusive b-jet spectrum into the three major hard underlying channels cross sections (for simplicity the small $bb \to bb$ is not shown). Figure from [122].

The study of NLO b-jet cross sections at LHC, Tevatron and SPS energies [122, 120, 126] indeed indicates a strong dependence on the choice of factorization and renormalization scales[2], evaluated by varying simultaneously μ_R and μ_F within the range $\mu_0/2 < \mu < 2\mu_0$, with $\mu_0^2 = {p_T}^2 + m_b^2$ [127]. Middle panels of Fig. 3.12 show the scale dependence at Tevatron (left) and LHC (right) energies obtained with MCFM.

[2]Unless otherwise specified the renormalization and factorization scales will be assumed to be equal, and simply denoted as μ.

The uncertainty induced by the choice of different sets of PDF is instead rather marginal, given the tight constraints set by the DIS and HERA data. Also the b-mass dependence of the theoretical result is small, given the large values of p_T probed by the collider experiments.

The strong scale dependence is likely to be associated with the channel with the most logarithms, gluon splitting. One therefore expects that, in a regime where the gluon-splitting contribution is suppressed by the dynamics, the scale dependence should be milder. At Tevatron energies, for low values of E_T, provided that the majority of the final-state generic jets are composed of primary gluons, b-quark jets are dominated by the process of gluon splitting, with the jet formed by the heavy-quark pair. The situation changes at higher values of E_T where heavy quarks are mostly produced via the s-channel annihilation of light quarks. On the contrary, at LHC energies the gluon splitting contribution rises with the energy of the b-jet. The fractions of Flavor Creation (FCR), Flavor Excitation (FEX) and Gluon Splitting (GSP) are reported in the bottom part of Fig. 3.12 as a function of the b-jet energy.

Chapter 4

Measurement of the Inclusive b-quark Cross Section

The measurement of the cross section for inclusive b-quark production at the LHC is a significant probe of Quantum Chromodynamics (QCD) at very high energies. In addition, knowledge of the inclusive b production rate from QCD processes helps constrain the background in searches for massive particles decaying into b quarks, like the top quark, the Higgs boson, or new heavy particles.

The b-quark production cross section is computed at the next-to-leading order (NLO) in a perturbative QCD expansion [104, 123, 125]: the sizeable scale dependence of the result suggests that the contribution from the neglected higher order terms is large [124, 128, 129]. The measurements performed at the Tevatron in $p\bar{p}$ collisions at $\sqrt{s} = 1.8$ TeV and 1.96 TeV [130, 131], and at the LHC by the CMS [132, 133], ATLAS [134] and LHCb [135] collaborations in pp collisions at $\sqrt{s} = 7$ TeV in different rapidity ranges are generally consistent with the theory. However, the comparisons are affected by large theoretical errors. Aside cross section measurements, CMS has performed a measurement of the angular correlations between beauty and anti-beauty hadrons ($B\bar{B}$) [136], thereby probing for the first time the region of small angular separation at LHC. In addition, also the exclusive cross section measurements for the decays $B^+ \to J/\psi K^+$, $B_d^0 \to J/\psi K_s$, $B_s^0 \to J/\psi\phi$ have been measured by CMS [137, 138, 139].

4.1 Previous measurements within CMS

The measurements use data recorded by the CMS detector during the first proton-proton collisions at the LHC at a center-of-mass energy of $\sqrt{s} = 7$ TeV. Complementary methods with different systematic uncertainties and covering different regions in phase space have been used, comparing the results to the NLO QCD predictions and various MC models.

The first approach [132] exploits the semileptonic decay of b quarks into muons and jets.

The muons provide a clean signal in the detector which allows their identification and detection already at the trigger level. Muons from b- and c-quark decays can be distinguished by their momentum distribution: due to the larger mass of the b-quark, the transverse momentum of the muon relative to the jet (p_T^{rel}) is on average larger in b-decays than in charm decays and for muons from light hadrons.

The second method [133] relies on the reconstruction of b-quark decay vertices within jets. Secondary vertices from b-decays are discriminated from background events based on the 3D flight length significance and the track multiplicity at the vertex.

The measurement of the angular correlations between b-jets [136] has been performed identifying the B hadrons through secondary vertices. The B hadron kinematics are reconstructed from the hadron decay vertex properties in combination with the primary interaction vertex. The measured differential $B\bar{B}$ production cross sections show a sizable fraction of the $B\bar{B}$ being produced with small opening angles.

These studies provide a test of QCD and further insight into the dynamics of $b\bar{b}$ hadroproduction. Some of these results will be summarized briefly in the following Sections.

4.1.1 Open beauty production with muons

The events of interest are selected by a single muon trigger with a transverse momentum threshold of $p_T > 3$ GeV [132]. The integrated luminosity used is 8.1 nb^{-1}. Background from non-collision events is reduced by requiring a reconstructed primary vertex with more than three associated tracks. At least one muon with transverse momentum $p_T > 6$ GeV, pseudorapidity $|\eta| < 2.1$ and a longitudinal distance from the interaction point below 20 cm is required. The p_T^{rel} variable is defined with respect to the axis of the fragmentation jet which is reconstructed from charged particle tracks only. In events satisfying the trigger and offline event selection, all tracks with $p_T > 0.3$ GeV are clustered into track jets by the anti-k_T jet algorithm [72] with $R = 0.5$. The b-jet is defined as the track jet containing the muon and is required to fulfill $E_T > 1$ GeV (excluding the muon track). The efficiency for finding a track jet around the muon depends on the muon p_T and rises from 74% to almost 100% for muons with $p_T > 20$ GeV.

A binned log-likelihood fit to the observed p_T^{rel} spectrum, based on templates obtained from simulation (signal and charm background) and data (the remaining background), is used to determine the fraction of signal events among the selected events. Since the shape of the p_T^{rel} distribution of muons from charm decays and muons from light hadrons cannot be distinguished by the fit, a fit discriminating the signal component against a single background component is implemented. The inclusive b-quark production cross section is then calculated according to

$$\sigma(pp \to b + X \to \mu + X', {p_T}^{\mu} > 6 \text{ GeV}, |\eta^{\mu}| < 2.1) = \frac{f_b \cdot N^{data}}{\mathcal{L} \cdot \varepsilon} \tag{4.1}$$

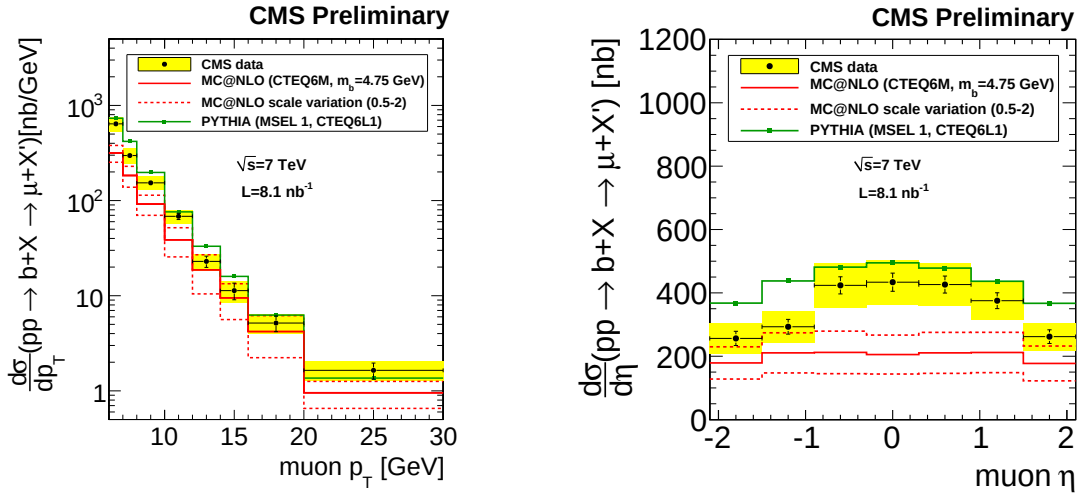

Figure 4.1: Differential b-quark cross section as a function of the muon transverse momentum (left) and pseudorapidity (right) compared to the PYTHIA and MC@NLO predictions. The yellow band shows the quadratic sum of statistical and systematic errors. The systematic error (11%) of the luminosity measurement is not included. Figures from [132].

where f_b is the fitted fraction of b-events among the selected events, N^{data}, and $\mathcal{L}$ the integrated luminosity. The efficiency ε includes the trigger efficiency (82%), the muon reconstruction efficiency (97%), and the efficiency for associating a track jet to the reconstructed muon (77%). The result of the inclusive b-quark production cross section within the kinematic range is

$$\sigma = 1.48 \pm 0.04\ (\text{stat}) \pm 0.22\ (\text{syst}) \pm 0.16\ (\text{lumi})\ \mu\text{b} \tag{4.2}$$

For comparison, the inclusive b-quark production cross section predicted by PYTHIA and MC@NLO are:

$$\sigma_{\text{PYTHIA}} = 1.8\ \mu\text{b}, \tag{4.3}$$

$$\sigma_{\text{MC@NLO}} = 0.84^{+0.36}_{-0.19}\ (\text{scale}) \pm 0.08\ (m_b) \pm 0.04\ (\text{pdf})\ \mu\text{b}, \tag{4.4}$$

where the major source of uncertainty in the NLO case is due to the scale uncertainty and amounts to 43%.

The results of the differential b-quark production cross section measured as a function of the muon transverse momentum and of the pseudorapidity are shown in Fig. 4.1. The NLO calculations underestimate the actual yield at low p_T and central pseudorapidities. The systematic errors of this analysis are dominated by the description of the light quark background (up to 10%) and of the underlying event (10%). The modeling of b-quark production, semileptonic b-hadron decays, and the signal efficiency is better understood and has less impact on the systematic error.

4.1.2 Inclusive b-jet Production

The inclusive b-jet production cross Section [133] is measured for transverse jet momenta $18 < p_T < 300$ GeV and for rapidities $|\eta| < 2$. Data are collected using a combination of minimum bias and single jet triggers, which are consecutively used in the lowest p_T range where the triggers are fully efficient. The integrated luminosity used is 85 nb^{-1}. The jets are reconstructed with the anti-k_T algorithm ($R = 0.5$) using Particle Flow objects [73]. This allows for a reliable jet energy reconstruction and good energy resolution down to low p_T. The jet energies are corrected for the absolute scale, transverse momentum and rapidity dependence [74]. The b-jets are identified using a secondary vertex tagger [140].

At least three tracks are required to be associated to the secondary vertex and b-quark decays are discriminated using the 3D decay length significance. The b-tagging efficiency and the mistag rates from c-jet and light jet flavors are taken from the MC simulation and constrained by a data-driven measurement. The b-tagging efficiency varies between 6% and 60% at $p_T > 18$ GeV and $|\eta| < 2.0$. The b-tagged sample purity is taken from MC.

Additionally, the purity is measured from a fit to the secondary vertex invariant mass distribution based on template function derived from MC. This fit allows for a robust estimate of the b-tagged sample purity and constrains the mistag rate uncertainty from c-jets. The purity obtained from MC simulation and from the template fit are compatible within the statistical uncertainty. The production cross section for b-jets is calculated as a double differential,

$$\frac{d^2\sigma}{dp_T dy} = \frac{N_{tagged} f_b C_{smear}}{\varepsilon_{jet}\varepsilon_b \Delta p_T \Delta y}, \tag{4.5}$$

where N_{tagged} is the measured number of b-tagged jets per bin, Δp_T and Δy are the bin widths in p_T and y, f_b is the fraction of tagged jets containing a b-hadron, ε_b is the efficiency of tagging b-jets, ε_{jet} is the jet reconstruction efficiency and C_{smear} is the unfolding correction to correct the measured jet p_T back to particle level.

The measured b-jet cross section is shown as a stand-alone measurement and as a ratio to the inclusive jet p_T spectrum [141] in Fig. 4.2. The results are found to be in good agreement with PYTHIA and in reasonable agreement with MC@NLO. The NLO calculation is found to describe the overall fraction of b-jets at $p_T > 18$ GeV and $|\eta| < 2.0$ well, but with significant shape differences in p_T and η. The leading uncertainties for the inclusive b-jet production are those coming from jet energy scale (12% at low p_T up to 40% at high p_T), luminosity, b-tag efficiency (about 20%), and mistag rates (15% at high p_T and forward rapidities). The uncertainty of the b-tagging efficiency and mistag rates are dominated by the statistical uncertainty in the data-driven method.

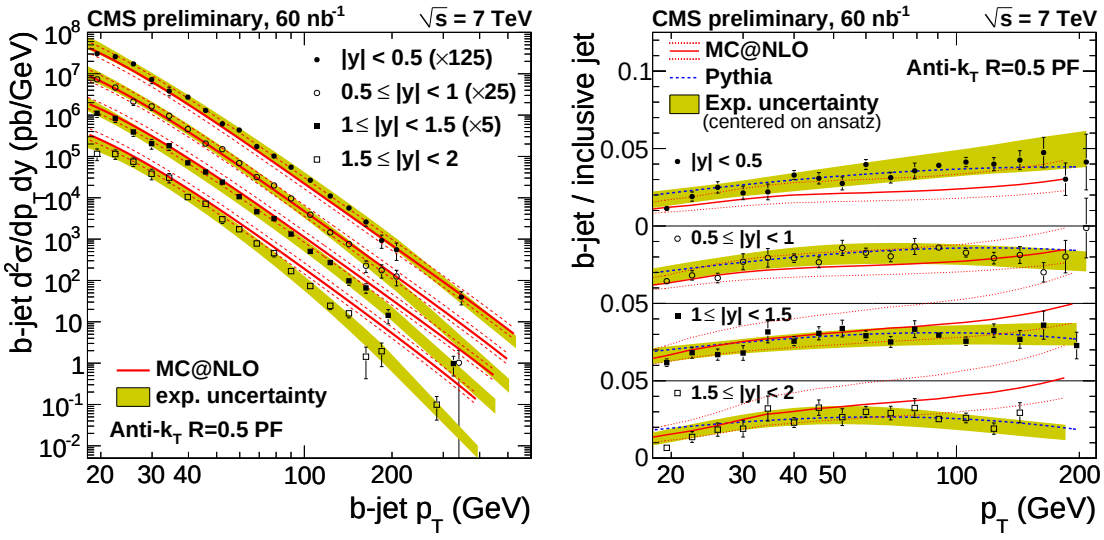

Figure 4.2: Measured b-jet cross section as a stand-alone measurement (left) and as a ratio to inclusive jet cross section (right). The NLO theory and PYTHIA MC predictions are shown for comparison. Figures from [133].

4.1.3 Measurement of $b\bar{b}$ Angular Correlations

The measurement of $b\bar{b}$ angular correlations [136] is done differentially as a function of the opening angle for different event scales, which are characterised by the leading jet transverse momentum in the event (independently of b hadrons). The leading jet of the event is used to trigger. The trigger thresholds are chosen such as to reach an efficiency over 99% for all three energy scale bins, which correspond to a leading jet p_T in excess of 56, 84 and 120 GeV, respectively, when using corrected jet energies. The data sample used corresponds to 3 pb^{-1} of integrated luminosity.

The cross sections are determined by applying efficiency corrections and normalising to the total integrated luminosity. The angular correlations between the two B hadrons are measured in terms of the difference in azimuthal angles ($\Delta\phi$) in radians and the combined separation variable $\Delta R = \sqrt{(D\eta)^2 + (\Delta\phi)^2}$. The analysis results are quoted for the visible kinematic range defined by the phase space at the B hadron level by the requirements $|\eta(B)| < 2.0$ and $p_T(B) > 15$ GeV for both of the B hadrons. The leading jet used to define the minimum energy scale is required to be within a pseudorapidity of $|\eta_{jet}| < 3.0$.

In order to measure the angular correlations also in the collinear regime, the reconstruction of the B hadrons is done independently of jet algorithms. The method uses the B hadron decays and is based on an iterative inclusive secondary vertex finder that exploits the tracking information [65, 66]. This allows to approximate the flight direction of the original B hadron by the vector between the primary (PV) and the secondary vertices (SV). A resolution of 0.02 rad in ΔR is achieved that way. The average overall event reconstruction

efficiencies (for both B hadrons) are found to be of order 10% at an average purity of 84%.

The measured cross sections are presented in Fig. 4.3 (left). Overlaid are the predictions by the PYTHIA calculations, which are normalised to the $\Delta R > 2.4$. region, where the calculations are expected to be more reliable. Note that an overall common systematic uncertainty of 47% due to the absolute normalization is not shown in the figures. The cross sections at small ΔR are substantial and even exceed the values observed at large angular separation values. Hence, the configurations where the two B hadrons are emitted in opposite directions are much less likely than the collinear configuration.

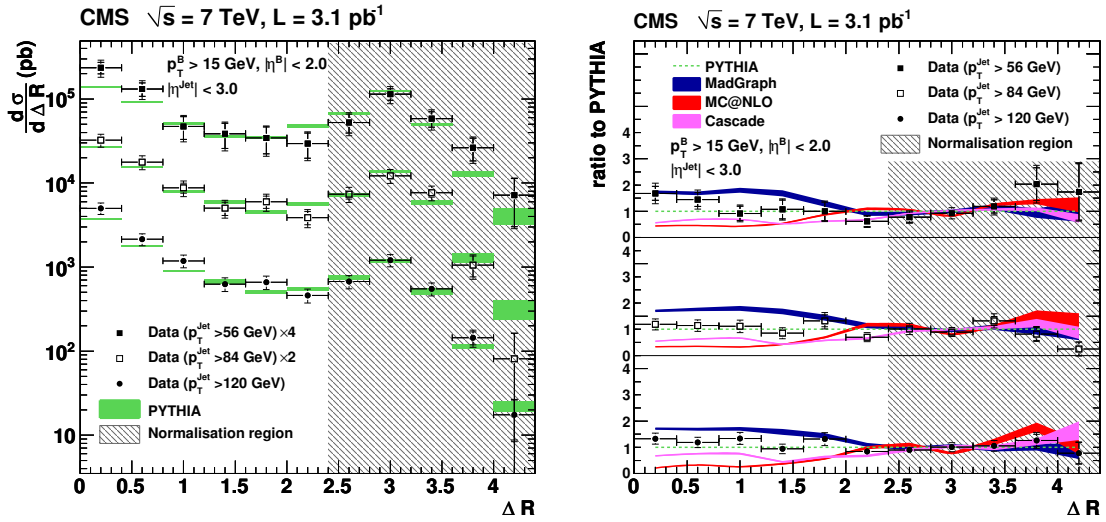

Figure 4.3: Left: differential BB production cross sections as a function of ΔR for the three leading jet p_T regions. For clarity, the $p_T > 56$ and 84 GeV bins are offset by a factor 4 and 2, respectively. The error bars of the data show the statistical (inner) and the total (outer bars) uncertainties. A common uncertainty of 47% due to the absolute normalization on the data points is not included. The PYTHIA prediction is normalised to the region $\Delta R > 2.4$. Right: ratio of the differential BB production cross sections, as a function of ΔR, for data, MADGRAPH [142], MC@NLO and CASCADE [143], with respect to the PYTHIA predictions, shown also for the three leading jet p_T bins. The simulation is normalised to the region $\Delta R > 2.4$ (rad) (FCR region), as indicated by the shaded normalization region. The widths of the theory bands indicate the statistical uncertainties of the simulation. Fogs. from [136].

The measurements are compared to various predictions, based on LO and NLO pQCD calculations. Fig. 4.3 (right) illustrates the shape sensitivity by showing the ratio of the different ΔR distributions to the PYTHIA Monte Carlo predictions. It is found that the overall tendency in shape is in general reasonably described by the predictions, however the normalizations and the details in shape, in particular at small opening angles, are not described well by any of the calculations. Apart from MADGRAPH, all predictions

underestimate the rate of collinear events: this kinematic region is mostly due to gluon splitting diagrams. The measurements show furthermore that the $B\bar{B}$ production cross section ratio $\rho_{\Delta R} = \sigma_{\Delta R} < 0.8/\sigma_{\Delta R} > 2.4$ increases as a function of the leading jet p_T in the event. Larger p_T values lead to more gluon radiation and, hence, are expected to produce more gluon splitting into $B\bar{B}$ pairs. This general trend is described reasonably by the theoretical calculations. The systematic uncertainties related to the shape analysis are evaluated to be around 15% in all the p_T bins and are dominated by the data-driven Jet energy scale, MC statistical uncertainty and its B hadron kinematics modeling.

4.1.4 Conclusions

The data yields tend to be higher than the MC@NLO prediction. Furthermore, significant shape differences are observed. In case of the cross section measurement with muons the discrepancies are confined to low p_T and central pseudorapidities, while the b-jet cross section is underestimated at high p_T and forward rapidities.

The angular correlation analysis shows an inadequate description of the $B\bar{B}$ opening angle distributions, since a substantial amount of small angle production is found in data, larger than that predicted, with large uncertainties, by the different generators. The collinear production tend to increase with respect to the back to back topology at higher event energy scale.

Chapter 5

The $pp \to b\bar{b}\mathrm{X} \to \mu\mu\mathrm{X}'$ Cross Section Measurement

5.1 Motivations

Given the large scale dependence of the b-quark production cross section, it is preferable to measure it in a region where the calculations are more reliable, for instance by selecting a kinematic domain where the gluon splitting contribution is suppressed. This seems particularly difficult at the LHC, because it represents the major contribution to the heavy flavor production mechanism.

An approach based on an alternative definition of b-jets has been proposed in [144, 122]. In this context, a definition of b-jets which maintains the correspondence between partonic flavour and jet flavour is used (such as the flavour-k_t algorithm of [145]). Within this algorithm, a jet containing equal number of b quarks and b antiquarks is considered to be a light jet, so that jets that contain a b and $\bar{b}$ from the gluon splitting channel do not contribute to the b-jet spectrum. The use of this kind of algorithm already leads to some reduction of the theoretical uncertainty on the b-jet spectrum with a standard massive calculation (*e.g.* MCFM). However, from the experimental point of view this approach relies on jets with two b's inside correctly distinguished from jets with a single b, which is a not a trivial task to achieve.

A different approach consists in the measurement of the cross section for the process $pp \to b\bar{b}\mathrm{X} \to \mu\mu\mathrm{X}'$. It requires a dimuon final state (cleaner with respect to the use of jets) which allows for the selection of a sample with high $b\bar{b}$ event purity in a wide kinematical region (muon pseudo-rapidity $|\eta| < 2.1$, muon momentum in the plane transverse to the beam axis $p_T > 4$ GeV or $p_T > 6$ GeV in the analysis presented here). The contribution from the gluon splitting is suppressed, as can be argued from simple kinematical considerations. In fact by requiring two muons (and therefore two b quarks) with a certain p_T threshold, we are naturally selecting events in which the two quarks carry a large

fraction of the overall available energy released in the pp collision and therefore more likely to be back-to-back (in this limit each quark carries half of the available energy), while in the gluon splitting configuration the two quarks have very little angular separation and therefore share the available energy with the recoil activity (in the limit case each quark carries one fourth of the available energy). The two different configurations are sketched in Fig. 5.1.

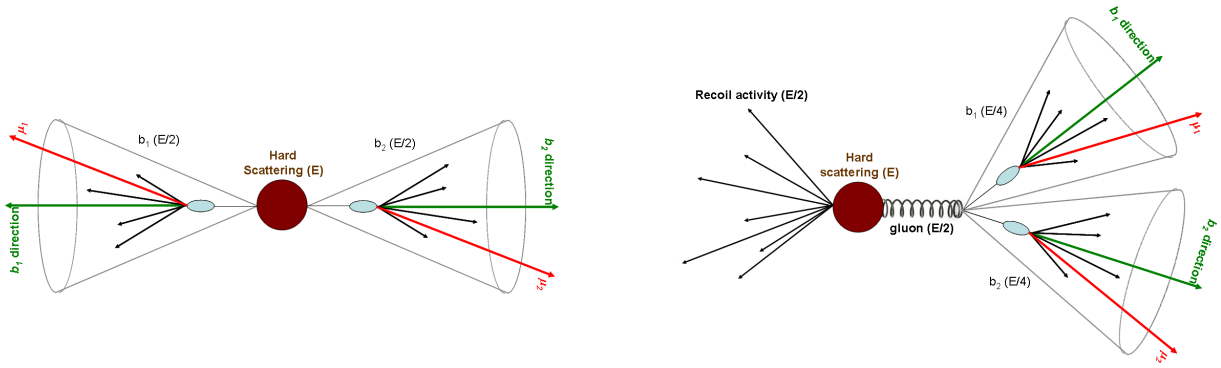

Figure 5.1: Sketch of angular configuration for b quarks emitted in different production processes. Left: back to back to configuration arising in Flavor Creation and Flavor Excitation; in this case each quark carries up to half of the available energy in the event. Right: little angular separation configuration arising from Gluon Splitting; in this case each quark carries only up to one fourth of the available energy in the event.

Background discrimination is accomplished with a fit to the two-dimensional distribution of the muon impact parameters, defined in Eq. 3.15. Since the particles involved in the process are all relativistic, then on average, δ is of the order of $1/\gamma$, and for $\gamma \gg 1$, the average impact parameter is

$$\langle d \rangle \simeq \beta\gamma c\tau(1/\gamma) = \beta c\tau \simeq c\tau, \tag{5.1}$$

where τ is the lifetime of the parent particle [113]. Note that, in this regime, the average size of the impact parameter is independent from the Lorentz boost γ and hence not very sensible to possible distortions in the p_T distribution in the simulation induced by the fragmentation model.
The measurements of the cross section presented here allows therefore a comparison with QCD predictions in a kinematic domain where NLO calculations are more reliable and the experimental uncertainties can be greatly reduced.

The cross section within the acceptance range is determined from the observed number of events $\mathcal{N}_{\mu\mu}$, the fraction of signal events in the dimuon sample f_{BB}, the average efficiency for the trigger, muon identification and event selection ϵ, the integrated luminosity $\mathcal{L}$, and

the fraction of signal events in the dimuon sample f_{BB} according to the relation:

$$\sigma(pp \to b\bar{b}X \to \mu\mu Y, {p_T}^{1,2} > 4 \text{ or } 6 \text{ GeV}, |\eta^{1,2}| < 2.1) = \frac{\mathcal{N}_{\mu\mu} \cdot f_{BB}}{\epsilon \cdot \mathcal{L}}. \tag{5.2}$$

The analysis is presented as follows. Section 5.2 describes the real and simulated data used for this measurement, and the selection criteria applied to define the analysis sample. Section 5.3 contains a detailed description of the categories in which events are grouped according to each muon production process and kinematic features. The fit algorithm is discussed in Section 5.4, and Section 5.5 describes how the efficiency is computed. Chapter 6 is entirely devoted to the determination of the systematic uncertainties. Finally, Chapter 7 reports the final result for cross Section measured in data and expected from QCD predictions.

5.2 Data Selection and Monte Carlo Simulation

The data employed for this measurement were collected by the CMS detector during the 2010 run of the LHC. They correspond to an integrated luminosity $\mathcal{L} = 27.9 \pm 1.1\,\text{pb}^{-1}$. A sample of events with two muons, each with transverse momentum $p_T > 3$ GeV were selected at the trigger level.

Further requirements, designed to increase the purity of the muon candidates and to improve the signal to background ratio, are applied at the analysis stage. A good muon candidate is obtained by matching hits in the tracker system with those in the muon chambers. The track must contain signals from at least 12 layers of silicon detectors, with at least two of which within the pixel detector, with a normalized χ^2 not exceeding 2. The overall χ^2 obtained when recomputing the track combining the hits in the tracker with those in the muon chambers should not exceed ten times the number of degrees of freedom. Finally, each muon must be contained in the acceptance region defined by the pseudo-rapidity range $|\eta| < 2.1$, and transverse momentum $p_T > 4$ GeV or $p_T > 6$ GeV.

Primary interaction vertices are reconstructed event-by-event from the reconstructed tracks. A candidate vertex is accepted if it has at least four degrees of freedom, and its distance from the beam spot does not exceed 24 cm along the beam line and 1.8 cm in the plane transverse to the beams. Muon tracks are retained if their transverse impact parameter d_{xy} with respect to the chosen primary vertex is smaller than 0.2 cm. To ensure that the two muons come from the same collision, events are retained only if both muon tracks belong to the same primary vertex within 1 cm along the beam direction.

To remove muons from Z decays, a cut on the dimuon mass $M_{\mu\mu} < 70$ GeV is applied. The region of Υ resonances, 8.9 GeV $< M_{\mu\mu} <$ 10.6 GeV, is also rejected. Charmonium resonances and sequential semileptonic decays from a single b-quark (for example $b \to J/\psi$ X $\to \mu\mu$X, $b \to c\mu$X $\to \mu\mu$X$'$) are rejected by selecting dimuons with $M_{\mu\mu} > 5$ GeV, as shown in

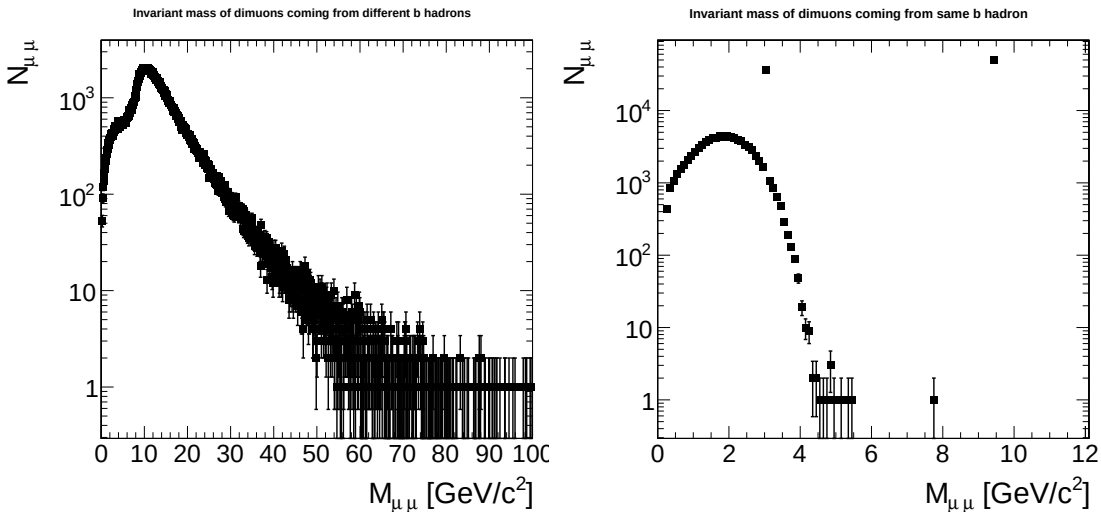

Figure 5.2: Invariant mass of generated muons coming from two different B hadrons (left) or coming from the same B hadron (right). The latter includes sequential decays and resonances (non-prompt J/ψ, Υ(1S)).

Fig. 5.2. Events are finally selected if one and only one pair of muons is found satisfying all the criteria defined above. A total of 537 734 events for $p_T > 4$ GeV and 151 314 events for $p_T > 6$ GeV are selected by these requirements.

Two samples of simulated events have been generated by using the Minimum Bias settings of PYTHIA 6.422 [115] (with MSEL=1), with Z2 tune [118] and using the CTEQ6L1 parton distribution functions [117]. To increase the generation efficiency within the selected acceptance, a filter is applied at generator level on the p_T, η of the hard interaction (p_T^{hat},η^{hat}) and by requiring two generated muons with kinematic cuts on ($p_T^{\rm Gen}$,$\eta^{\rm Gen}$). For the measurement with $p_T > 4$ GeV the hard interaction is imposed to fulfill $p_T^{hat} > 2$ Gev and $\eta^{hat} < 5$ and for the generated muons $p_T^{\rm Gen} > 2.5$ GeV and $|\eta^{\rm Gen}| < 2.5$, while for the measurement with $p_T > 6$ GeV is required that $p_T^{hat} > 5$ Gev and $\eta^{hat} < 5$, and for generated muons $p_T^{\rm Gen} > 5$ GeV and $|\eta^{\rm Gen}| < 2.5$. The generated samples include decays of light mesons (mostly charged kaons and pions) only within the tracker volume. The code name for this simulation is /QCD_DoubleMuFilter_OSAndSSMuons_7TeVpythia6/Fall10-START38_V12-v2/. The efficiency of the filter is extremely low, and prevented the production of a larger sample of QCD events.

A third Monte Carlo sample has been produced to simulate the Drell-Yan (DY) process. DY was produced in three different datasets with 3 invariant mass ranges, as listed in Table 5.2. The total DY spectrum in simulation was obtained by summing the partial spectra, rescaling the datasets to the same integrated luminosity.

Monte Carlo events, including full simulation of the CMS detector and trigger, are subjected

to the same reconstruction and selection as the real data.

Analysis p_T cut	σ [pb]	Filter cuts	ε_{Filter}	$N_{Filtered}$ [M]	$\mathcal{L}$ [pb^{-1}]
$p_T > 4$ GeV	48.44×10^9	$\lvert\eta^{hat}\rvert<5$ $\lvert\eta^{\mu}\rvert<2.5$ $p_T^{hat}>2$ GeV $p_T^{\mu}>2.5$ GeV	1.7×10^{-6}	5.37	4.35
$p_T > 6$ GeV	48.44×10^9	$\lvert\eta^{hat}\rvert<5$ $\lvert\eta^{\mu}\rvert<2.5$ $p_T^{hat}>5$ GeV $p_T^{\mu}>5$ GeV	7.7×10^{-8}	0.37	6.57

Table 5.1: Relevant numbers for simulated Minimum Bias muon enriched sample (QCD_DoubleMuFilter_OSAndSSMuons_7TeVpythia6Fall10-START38_V12-v2).

Mass range [GeV]	σ [pb]	N. events [M]	$\mathcal{L}$ [pb^{-1}]	SF
$2 - 10$	72 990	1.92	26.38	1.0
$10 - 20$	2 659	1.96	736.39	0.0358
$20 - \infty$	1 300	1.62	1 244.29	0.0212

Table 5.2: Relevant number for simulated Drell-Yan events in different invariant mass range bins.

5.3 Muon Classes and Transverse Impact Parameter Distributions

The fraction of signal events ($pp \to b\bar{b}X \to \mu\mu X'$) in data is obtained with a fit to the two-dimensional distribution of the transverse impact parameters of the muons. For this purpose reconstructed muons in simulated data are collected in four different classes, defined according to their origin. The single particle distributions of the transverse impact parameter d_{xy} are obtained for each Monte Carlo class and interpolated by analytical functions. From these functions the two-dimensional templates are built symmetrically. This procedure is described in the following paragraphs.

5.3.1 Definition of Muon Classes

Information from the generation process is used to assign each reconstructed muon in the simulation to a well-defined category. Reconstructed muon candidates are linked to the corresponding generated charged particle with a hit-based associator, which reduces the probability of incorrect associations to a negligible level. The association is performed on the basis of the reconstructed muon inner (tracker only), outer (muon system only) and eventually global (tracker + muon system) tracks. These associations can in fact point to several (or none) generated particles, depending on the nature of the muon.
Possible combinations of the association outcomes can be:

- Both the inner and outer tracks are associated to a generated muon or the outer track is not associated to any genparticle. According to the event record the last case

happens when the muon emits one or more electrons inside the endcap yoke (they are decayed by GEANT [146]). The reconstructed muons are coming from physical processes.

- The inner track is associated to a particle P_{in} which is not a muon, while the outer track is associated to a muon P_{out} which belongs to the decay chain of P_{in}. The reconstructed muon comes from a decay in flight which took place in the outer part of the tracker volume.

- The inner track is not associated to any generated particle, while the outer track is associated to a muon. The reconstructed muon comes from a decays in flight in the middle of the tracker volume, therefore neither the generated muon nor its parent particle have enough simulated hits to be associated to the inner track.

- Both the inner and outer tracks are associated to generated particles which are not muons. The reconstructed muon is classified as punchthrough.

- The inner track is associated to a particle P_{in} that is not a muon, and outer track is associated to a particle P_{out} which does not belong to the decay chain of P_{in} or is not associated to any particle. In this case the reconstructed muon is considered as misreconstructed muon.

- No associated particle is found for inner and for outer track. The reconstructed muon is considered as fake.

Muons tracks are then assigned to one of the following classes:

1. Beauty hadron decays (B): muons produced in the decay of a B hadron, including both direct decays ($b \to \mu^{-}\mathrm{X}$) and cascade decays ($b \to c\mathrm{X} \to \mu\mathrm{X}'$, $b \to \tau^{-}\mathrm{X} \to \mu^{-}\mathrm{X}'$, $b \to J/\psi\ \mathrm{X} \to \mu^{\pm}\mathrm{X}$);

2. Charmed hadron decays (C): muons from prompt charm production and following charmed hadron decays;

3. Prompt tracks (P): candidates originating in the primary vertex, mostly muons from Drell-Yan process and quarkonia decays. This category also includes primary hadrons punching through the calorimeters and the iron yoke to the muon chambers and muons produced in the late decay of charged pions and kaons in the volume included between the tracker and the muon chambers;

4. Decays in flight (D): muons produced in the weak decay of charged pions or kaons (which may come either from light- or heavy-flavour hadrons) taking place within the tracker volume.

Source	$p_T > 4$ GeV	$p_T > 6$ GeV
B hadron (B)	77.82 ± 0.24	79.75 ± 0.36
C hadron (C)	13.96 ± 0.08	12.59 ± 0.12
Prompt sources (P)	1.84 ± 0.04	3.44 ± 0.08
Decays in flight (D)	6.38 ± 0.07	4.21 ± 0.09

Table 5.3: Percent fraction of events from each muon source in simulated events.

Table 5.3 reports the sample composition according to the simulation for events passing the full selection and the dimuon trigger. While the fraction of muons due to decays in flight decreases at larger p_T, the prompt component increases due to Drell-Yan muons.
A dedicated Monte Carlo simulation of 200 000 QCD events without muon filter has been produced to check that PYTHIA is correctly reproducing the branching fractions of the b- and c-hadron. The expectation values for the B hadrons are taken from the PDG [112] while the C hadrons references [147, 148] have been used. The results are reported in table 5.4. Most of the b and c hadrons are produced with proportions consistent within the errors of the published numbers.

Hadron name	PYTHIA fraction	Expected fraction
B hadrons	3946	-
B^0	40.55%	(39.7±1.0)%
B^+	38.67%	(39.7±1.0)%
B_s	12.57%	(10.7±1.1)%
Λ_b	8.01%	(9.9±1.7)%
B_c	0.05%	-
$b\bar{b}$	0.15%	-
C hadrons	59228	-
D^0	10.04% (direct)	(16.4±2.3)%
D^+	10.18% (direct)	(16.4±2.3)%
$D*^0$	29.50%	(22.8±2.5)%
($\mathrm{D}^{*0} \to \mathrm{D}^0$)	100%	100%
$D*+$	29.46%	(22.8±2.5)%
($\mathrm{D}^{*+} \to \mathrm{D}^0$)	67.78%	(67.7±0.5)%
($\mathrm{D}^{*+} \to \mathrm{D}^+$)	32.20%	(32.3±0.5)%
D_s	2.92%	-
$D*_s$	8.84%	-
Total for Charm hadrons		
$D^0 tot$	59.51% (direct+D^{*0}+D^{*+})	(54.6±2.6)%
$D^+ tot$	19.67% (direct+D^{*+})	(23.76±2.5)%
$D*_s\, tot$	11.76%	(12.1±2.5)%
Λ_c	8.20%	(9.5±4.0)%
$c\bar{c}$	0.87%	-

Table 5.4: Comparison of b- and c-hadrons fractions in PYTHIA and in ref. [112, 147, 148]

5.3.2 Measurement of the Transverse Impact Parameter Resolution in Data and Simulation

The transverse impact parameter resolution is an important aspect of this analysis.
To measure it muons coming from a prompt source are selected. Their distribution is described by a pure resolution. Muons from the $\Upsilon(1S) \to \mu^+\mu^-$ events are used [131]. The invariant mass in the resonance range is shown in Fig. 5.3 for data (where the whole Υ familiy is observed) and MC (where only the $\Upsilon(1S)$ is produced). The background, which

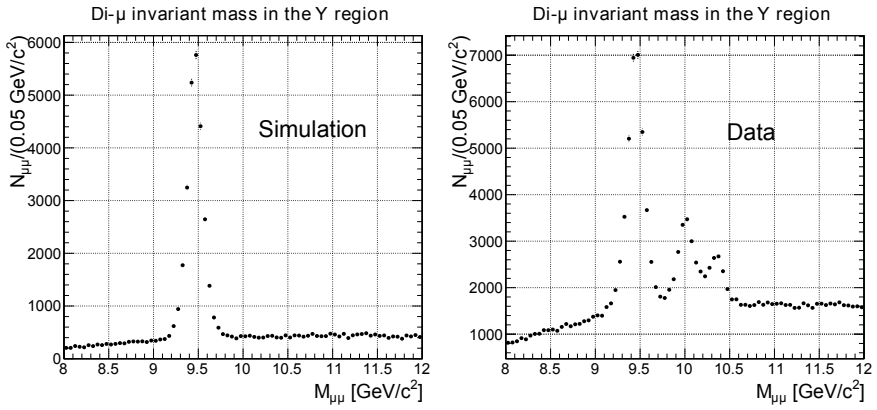

Figure 5.3: Di-muon invariant mass in the Υ range for MC (left) and data (right). Muons contributing to the first Υ resonance (1S) are considered as "prompt" and are selected to calculate the resolution on the measurement of transverse impact parameter.

is fitted with a quadratic function, is properly taken into account by sideband subtraction.

The signal (red) and background (blue) regions are highlighted in the left part of Fig. 5.4. The transverse impact parameter distribution of the two regions, using the same color scheme, is reported in the right part of the same Figure. The sideband subtracted impact parameter distribution from prompt sources is then computed, as shown in the left part of Fig. 5.5. To ensure that the procedure is correct we verify that the tail ($d_{xy} > 0.05$ cm) of the sideband subtracted transverse impact parameter distribution is compatible with zero as shown in the right part of Fig. 5.5. Finally, the side-band subtracted transverse impact parameter distribution for $\Upsilon(1S)$ in data and MC for muons with $p_T > 4$ GeV and $p_T > 6$ GeV is reported in Fig. 5.6.

To give a quantitative estimate of the resolution it is possible to compute the transverse impact parameter value corresponding to 68% (1σ) and 95% (2σ) of the distribution integral, as reported in Table 5.5. The resolution is defined as the impact parameter value at 1σ. The difference in the resolution between data and MC will be taken into account while estimating the systematic uncertainties affecting the measurement.

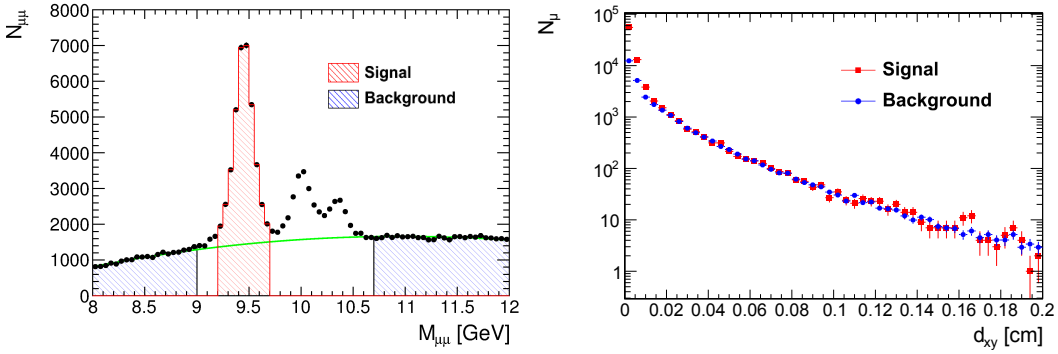

Figure 5.4: Left: di-muon invariant mass in the Υ peak region. The signal (red) and sideband (blue) ranges are highlighted, and the function used to fit the background is shown superimposed. Right: single muon transverse impact parameter distributions for muons coming from the signal (red) and the sideband (blue) region. The sideband is rescaled to the fitted background area below the signal.

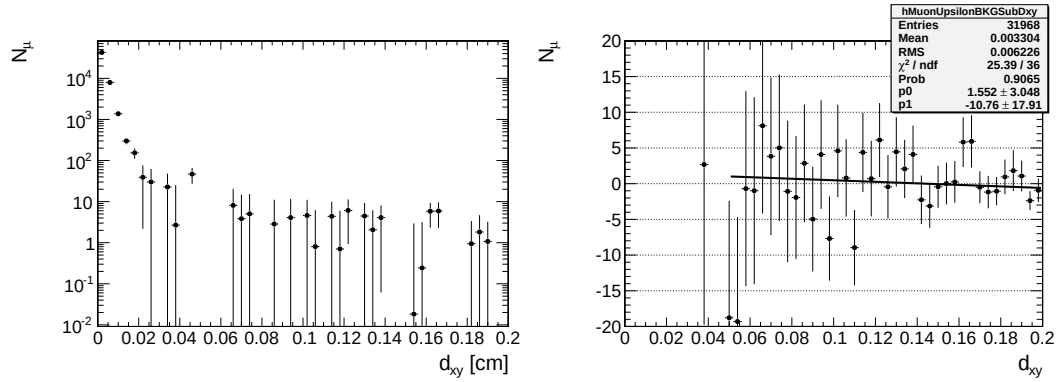

Figure 5.5: Left: single muon sideband-subtracted transverse impact parameter for muons under the Υ peak. Right: tail of the single muon sideband-subtracted transverse impact parameter for muons under the Υ peak, with a linear fit superimposed, showing that it is compatible with a flat line.

	$p_T^\mu > 4$ GeV		$p_T^\mu > 6$ GeV	
CL	68%	95%	68%	95%
MC	29.4 μm	70.9 μm	22.1 μm	47.8 μm
Data	27.9 μm	73.5 μm	21.4 μm	52.0 μm

Table 5.5: Integral of fitting function. Table shows the values of d_{xy} corresponding to the 68% and 95% of the integral.

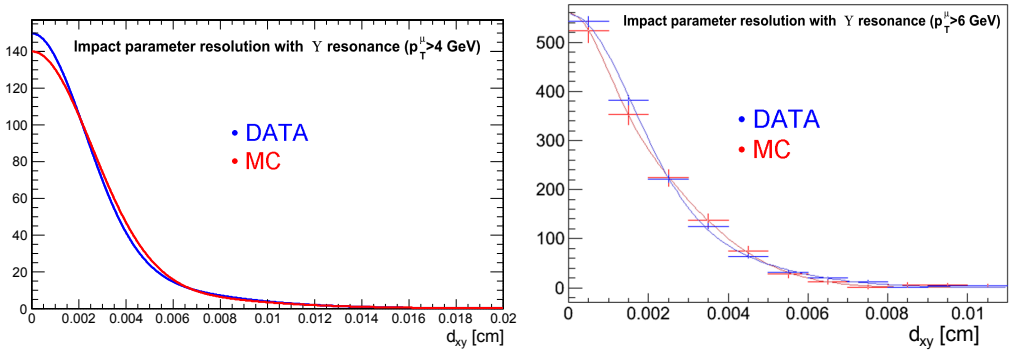

Figure 5.6: Comparison of the fit results in MC (RED) and data (BLUE). Both curves are renormalized to the same integral. Left: muons with $p_T^\mu > 4$ GeV, right: muons with $p_T^\mu > 6$ GeV.

5.3.3 One-Dimensional Template Distributions

The d_{xy} distributions for muons with $p_T > 4$ GeV obtained in the simulation for classes B, C, D are shown in Figs. 5.7, 5.8 and marked with red points .
The transverse impact parameter distribution for muons coming from prompt sources described in class P is taken by mean of a data-driven technique using the $\Upsilon(1S)$ resonance, as discussed in the previous paragraph. The analytical function used in interpolation of the prompt sample is the superposition of a Gaussian centered at zero and an exponential function describing the effect of the finite resolution of the detector; the other classes are interpolated with a sum of two exponential functions plus a Gaussian. The resulting fit parameters are reported in table 5.6. The functions are represented by continuous black lines overlaid to the histograms in Fig. 5.7 and 5.8, while the black points represent the template histograms obtained by evaluating the fit functions at the bin center. The templates for muons with $p_T > 6$ GeV are obtained in a similar way.

Fit Parameters		B	C	P	D
Muons with $p_T > 4$ GeV					
Gaussian	Constant	$(5.68 \pm 0.05) \times 10^4$	$(1.68 \pm 0.04) \times 10^4$	$(4.1 \pm 0.1) \times 10^4$	$(3.6 \pm 0.1) \times 10^3$
	σ	$(3.05 \pm 0.02) \times 10^{-3}$	$(3.15 \pm 0.05) \times 10^{-3}$	$(2.83 \pm 0.02) \times 10^{-3}$	$(3.28 \pm 0.08) \times 10^{-3}$
Exponential 1	Constant	(10.30 ± 0.01)	(6.5 ± 0.3)	(9.9 ± 0.1)	(6.6 ± 0.2)
	Slope	(-67±1)	(-45 ± 3)	$(-2.78 \pm 0.07) \times 10^2$	$(-1.0 \pm 0.1) \times 10^2$
Exponential 2	Constant	(8.41±0.08)	(9.01 ± 0.05)	-	(3.8 ± 0.3)
	Slope	(-26.1±0.6)	$(-1.20 \pm 0.06) \times 10^2$	-	(-18 ± 2)
Muons with $p_T > 6$ GeV					
Gaussian	Constant	$(2.94 \pm 0.04) \times 10^4$	$(8.0 \pm 0.2) \times 10^3$	$(8.9 \pm 0.1) \times 10^3$	$(3.4 \pm 0.1) \times 10^3$
	σ	$(2.63 \pm 0.04) \times 10^{-3}$	$(2.87 \pm 0.07) \times 10^{-3}$	$(2.78 \pm 0.02) \times 10^{-3}$	$(2.75 \pm 0.09) \times 10^{-3}$
Exponential 1	Constant	(9.54 ± 0.02)	(5.1 ± 0.5)	(0.00 ± 0.02)	(6.7 ± 0.2)
	Slope	(-67±2)	(-40 ± 6)	-	$(-1.3 \pm 0.2) \times 10^2$
Exponential 2	Constant	(7.7±0.1)	(8.00 ± 0.07)	-	(4.1 ± 0.2)
	Slope	(-27.0±0.8)	$(-1.11 \pm 0.08) \times 10^2$	-	(-27 ± 3)

Table 5.6: Fit parameters of the analytical functions used to interpolate the templates, sum of a Gaussian plus one or two exponential functions.

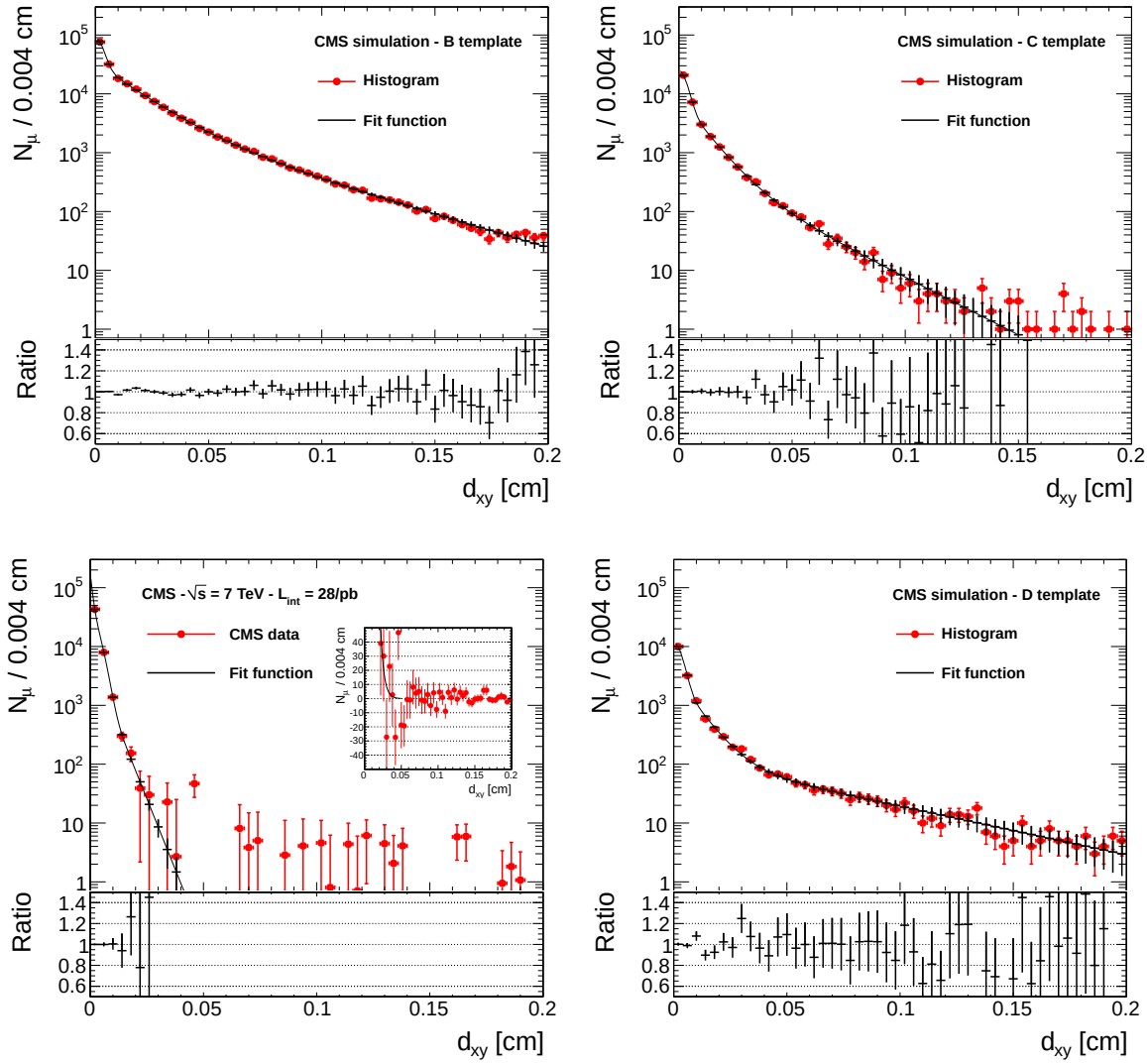

Figure 5.7: Comparison, for muons with $p_T > 4$ GeV, between the raw template histogram (red) and template fitting function (black) for muons coming from B hadrons (top left), charmed hadrons (top right), from prompt tracks (bottom left) and decays in flight (bottom right). For the prompt tracks, obtained with the sideband subtraction technique, the zoomed region around $y = 0$ is shown inlay in linear scale. The ratios between the raw data and the fit functions are displayed below all the main histograms.

5.3.4 Two-Dimensional Template Distributions

In principle, the dimuon events could be split into sixteen different categories, obtained by combining the four classes defined above for each muon. In order to reduce the number of categories, the d_{xy} distributions are symmetrized (i.e. BC=CB, BD=DB, etc.) by employing a method originally developed by the CDF collaboration [131]. The one-dimensional

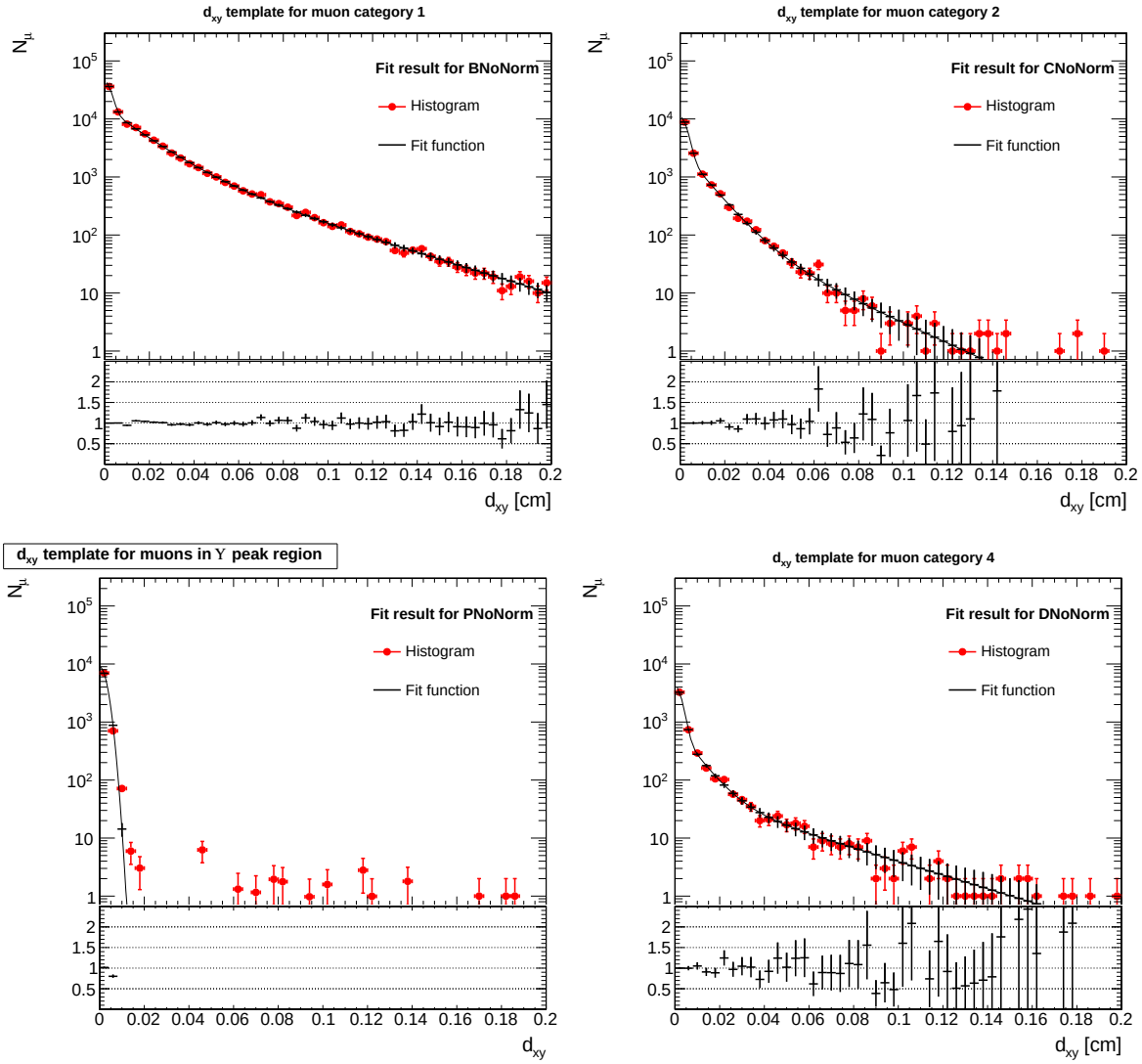

Figure 5.8: Comparison, for muons with $p_T > 6$ GeV, between the raw template histogram (red) and template fitting function (black) for muons coming from B hadrons (top left), charmed hadrons (top right), from prompt tracks (bottom left) and decays in flight (bottom right). The ratios between the raw data and the fit functions are displayed below all the main histograms.

smoothed histograms, built as described above, are normalized to unity within the fit range ($0 < d_{xy} < 0.2\,\text{cm}$). The symmetrized two-dimensional template histogram for the event with a muon of class ρ and another of class σ (ρ, $\sigma = 1, ..., 4$ according to the definition in Section 5.3.1) is then constructed as:

$$T_{ij}^{\rho,\sigma} = \frac{1}{2}(S_i^\rho S_j^\sigma + S_j^\rho S_i^\sigma) \tag{5.3}$$

Source	Fraction in simulation (%)	
	$p_T > 4$ GeV	$p_T > 6$ GeV
BB	71.59 ± 0.24	74.62 ± 0.44
CC	9.24 ± 0.08	8.67 ± 0.14
BC	5.66 ± 0.07	5.22 ± 0.11
PP	1.84 ± 0.04	3.43 ± 0.08
DD	1.49 ± 0.04	0.73 ± 0.04
BD	6.01 ± 0.07	4.40 ± 0.10
CD	3.69 ± 0.05	2.53 ± 0.08
PX	0.48 ± 0.02	0.40 ± 0.03

Table 5.7: Sample composition of dimuon event sources in the simulation. PX represents the sum of the contributions from PB, PC and PD.

where S_i^ρ is the content of the i^{th} bin of the histogram describing the class ρ. In this way ten symmetric distributions are obtained. In practice, the few events from PX (where X=B,C,D) are neglected, thus reducing the number of significant classes to seven.
Fig. 5.9 shows the result for the BB and CC components, while Fig. 5.9 reports the PP and DD ones, obtained for muons with $p_T > 4$ GeV. The 1D projections of the seven templates used in the analysis are shown in Fig. 5.10.
The expected composition of the dimuon events in the simulation is reported in Table 5.7. The errors in the table are due to the limited size of the simulated samples.

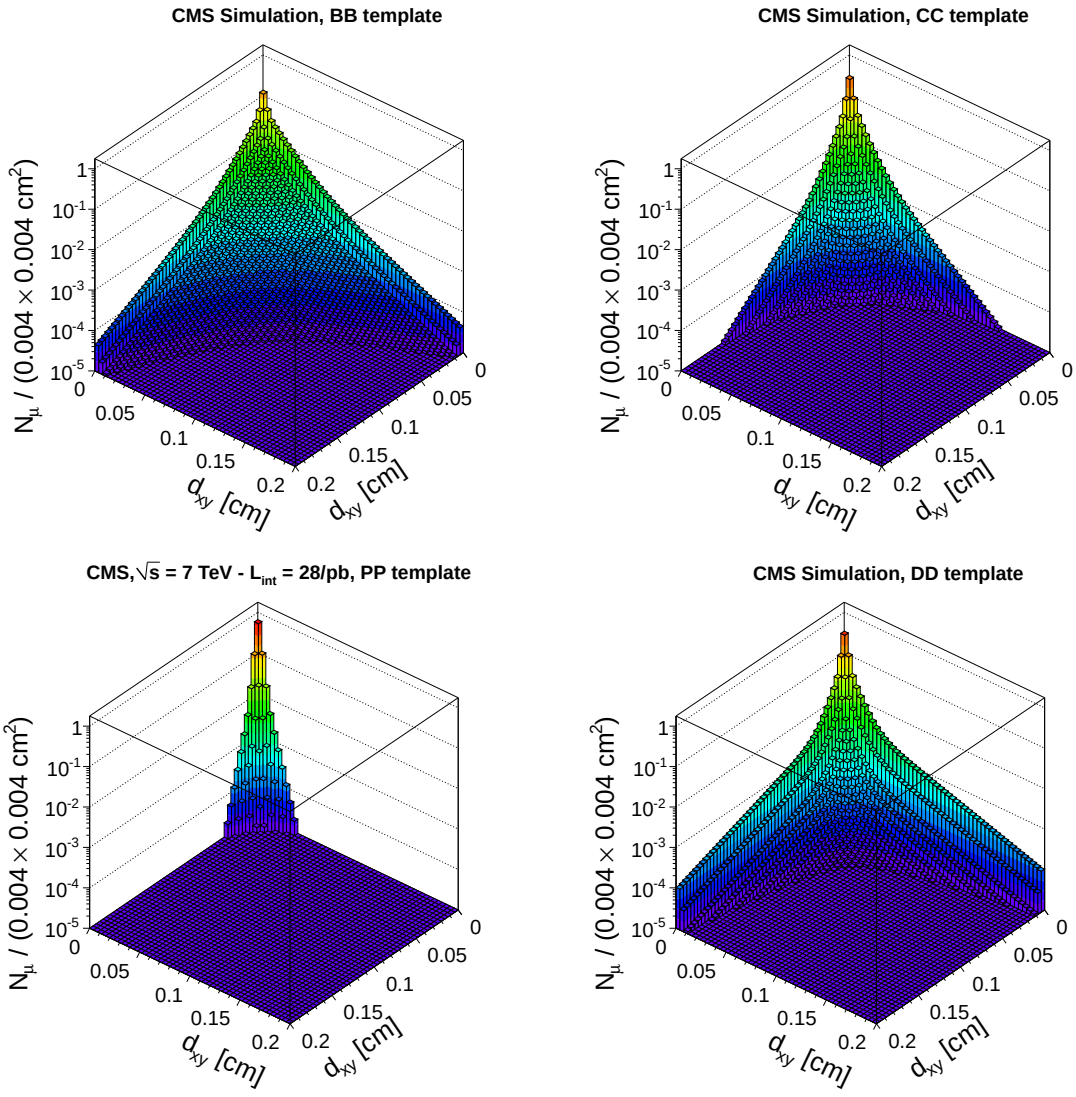

Figure 5.9: 2D template built by symmetrizing the 1D templates obtained by raw template fitting in the simulation. Top: BB (left) and CC (right). Bottom: PP (left) and DD (right).

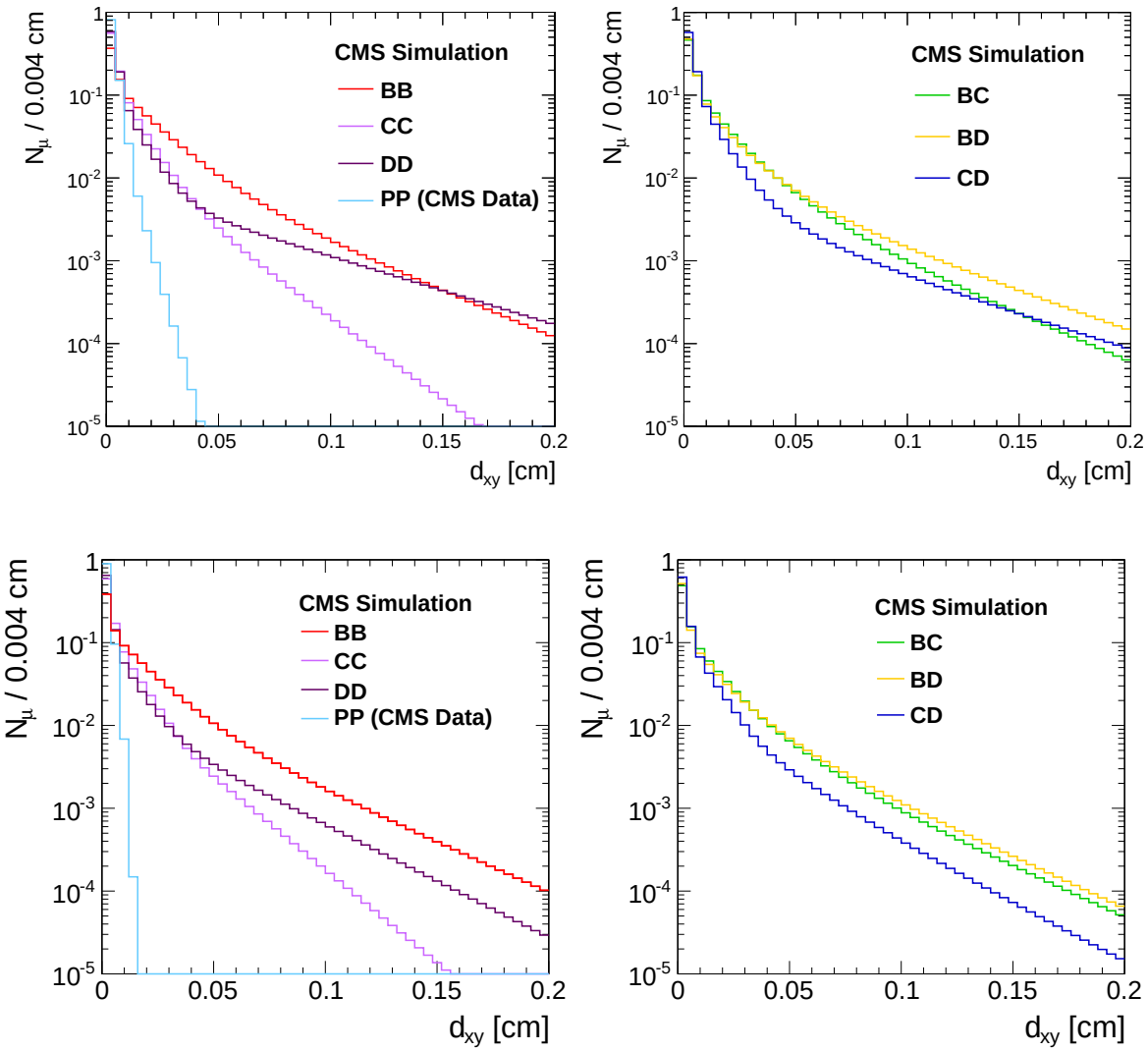

Figure 5.10: The 1D projections of the seven templates used in the analysis for muons with $p_T > 4$ GeV (top row) and $p_T > 6$ GeV (bottom row), for the diagonal components (BB, CC, PP, DD) on the left, and for the off-diagonal ones (BC, BD, CD) on the right.

5.4 Measurement of the Sample Composition

Consistent with the symmetric two-dimensional templates, data events are randomized by taking the impact parameters of the two muons in each event, and filling the bin corresponding to $[d_{xy}(\mu_1), d_{xy}(\mu_2)]$ or to $[d_{xy}(\mu_2), d_{xy}(\mu_1)]$ according to the outcome of a random number generator. The results can be seen in Fig. 5.11 for data together with the 1D projections along the x and y axis.

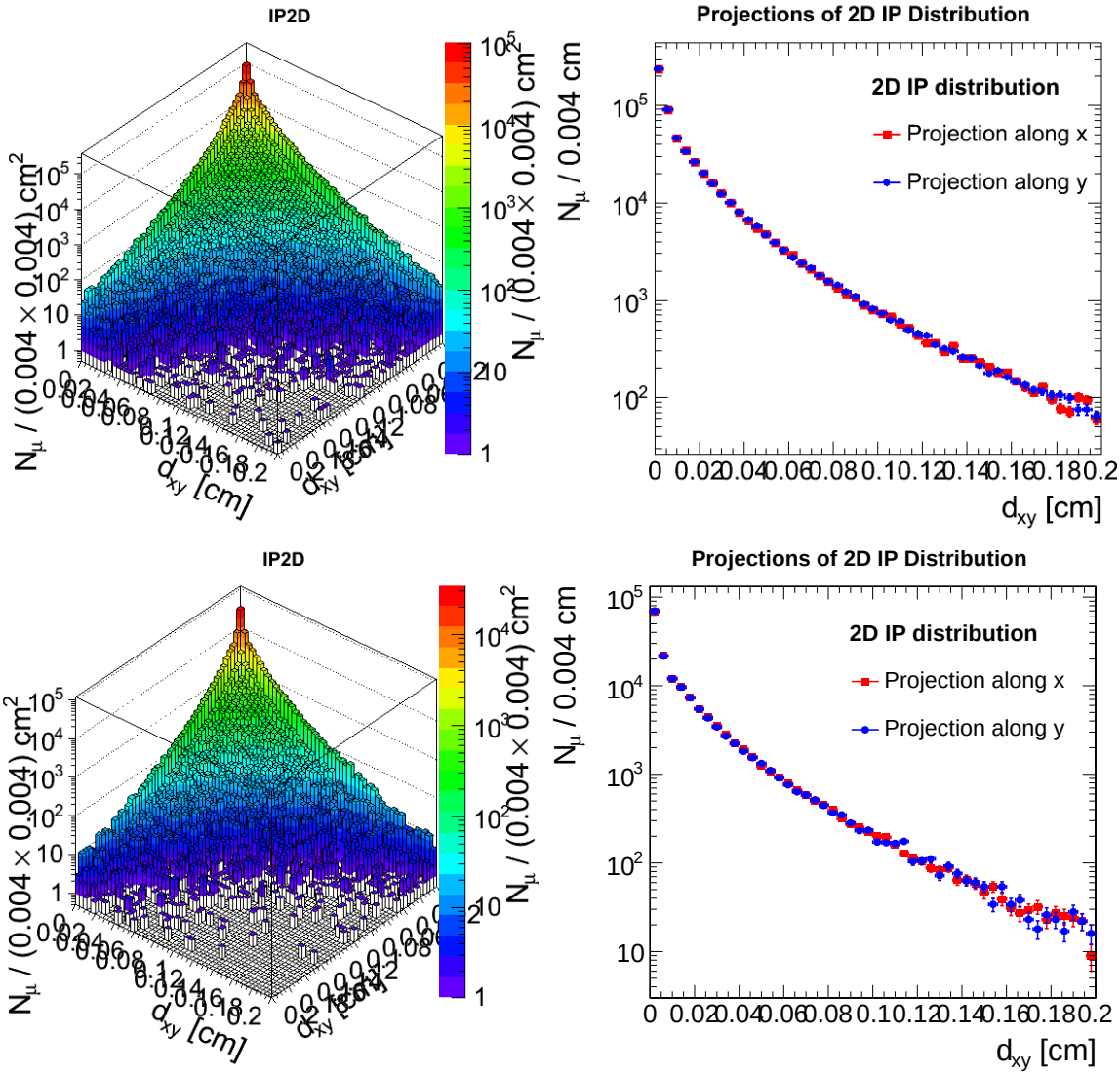

Figure 5.11: 2D symmetrized distributions in data and their projections for muons with $p_T > 4$ GeV (top) and $p_T > 6$ GeV (bottom).

The sample composition, expressing the individual contributions to the observed distribution, is determined with a binned maximum likelihood fit. The fraction of $b\bar{b}$ events can be

obtained by minimizing the function:

$$-2 \cdot \ln(L) = -2 \cdot \left\{ \sum_{i,j=1}^{7} [n_{ij} \cdot \ln(l_{ij}) - l_{ij}] - \frac{1}{2} \cdot \sum_{k'=1}^{3} \left(\frac{r_{k'} - r_{k'}^{MC}}{\sigma_{r_{k'}}^{MC}} \right)^2 \right\} \tag{5.4}$$

where n_{ij} is the content of the data histogram in the bin $(i,\ j)$, $l_{ij} = \sum_k [f_k \cdot T_{k,ij}]$, T_k is the k^{th} template ($k = 1, ..., 7$) and f_k is the fit parameter expressing the fraction of events from the k^{th} source. The fitted fractions are subject to the normalization condition $\sum_{k=1}^{7} f_k = 1$.

To reduce the number of fit parameters, and ease the fit convergence, the three parameters f_{BC}, f_{BD}, and f_{CD} are constrained in such a way that the ratios f_{BC}/f_{BB}, f_{BD}/f_{BB}, and f_{CD}/f_{CC} are compatible with the expectations from the MC simulation within their statistical uncertainties. It must be noted that the BC component originates from the production of an extra $c\bar{c}$ pair from gluon splitting in a $b\bar{b}$ event. The production of charm (and beauty) pairs from gluon splitting has been measured at LEP [149, 150, 151] and compared to the theory predictions. In contrast, the BD and CD contributions are related to the misidentified muon rate in events with true B and C production. Here we rely on the quality of our MC simulation, which has been compared to direct measurements of the fake rates in data [68]. In Eq. (5.4), k' is the index of the constrained templates (BC, BD, CD), $r_{k'}$ is the ratio of the constrained fit fraction with respect to the reference fit fraction (for instance in the BC case $r_{BC} = f_{BC}/f_{BB}$), $r_{k'}^{MC}$ is the ratio between the constrained fraction and reference fraction in the simulation and $\sigma_{r_{k'}}^{MC}$ its statistical uncertainty due to the limited amount of simulated events. The systematic uncertainty induced by the use of these constraints is discussed in Section 6.

Table 5.8 reports the results of the fit on the data sample. The quoted errors are obtained from the fit and are limited by the statistics in the data sample. It is observed that the BB fraction is smaller than the PYTHIA prediction while the DD is larger than expected. The PP fraction is in good agreement with expectations for the two $p_T$selections used.

Source	Fraction in data (%)	
	$p_T > 4$ GeV	$p_T > 6$ GeV
BB	65.1 ± 0.3	69.0 ± 0.4
CC	11.5 ± 0.6	7.8 ± 1.2
BC	5.1 ± 0.1	4.9 ± 0.1
PP	1.3 ± 0.3	4.6 ± 0.5
DD	6.9 ± 1.2	7.3 ± 2.7
BD	5.5 ± 0.1	4.2 ± 0.1
CD	4.6 ± 0.8	2.3 ± 1.3

Table 5.8: Results of the likelihood fit on data. The BC, BD and CD fractions are constrained to their ratios to BB and CC fractions as expected from the simulation.

Projections of the fits on the d_{xy} distributions are shown in Fig. 5.12 for the two p_T cuts used in the analysis.

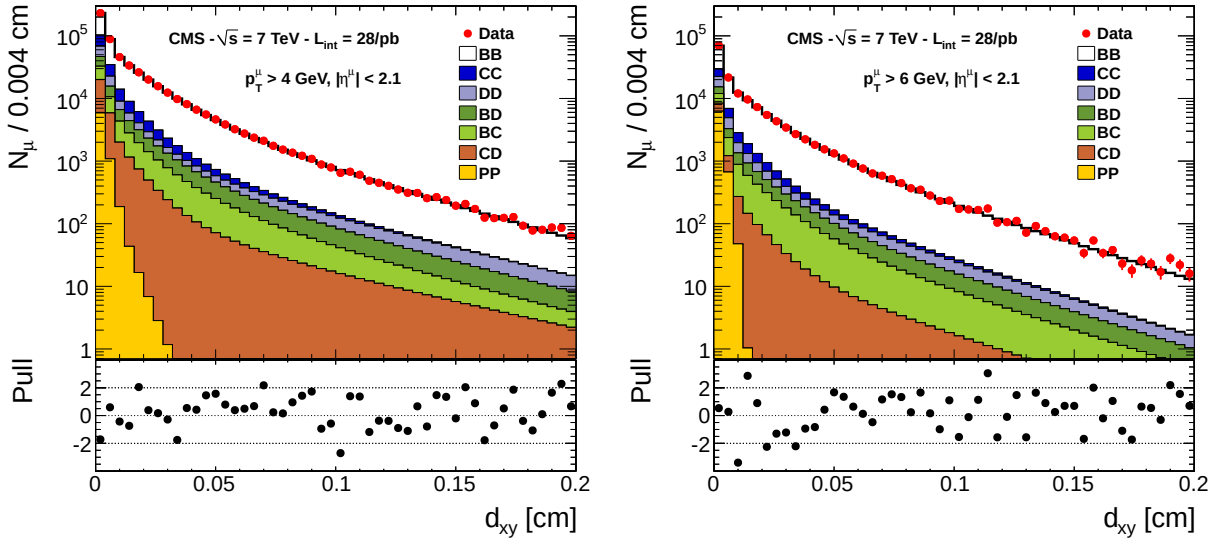

Figure 5.12: Projection of the likelihood fit result superimposed to data. The different contributions as measured by the fit are stacked with different colors. Left: muons with $p_T > 4$ GeV. Right: muons with $p_T > 6$ GeV.

Finally, the distributions obtained for the p_T, η and invariant mass of the leading and second leading p_T muons in the selected events are compared to the simulation rescaled to match the fit results. They are displayed in Figs. 5.13, 5.14.
Discrepancies can be observed in the p_T and invariant mass spectrum, which will be taken into account in the evaluation of the systematic uncertainties.

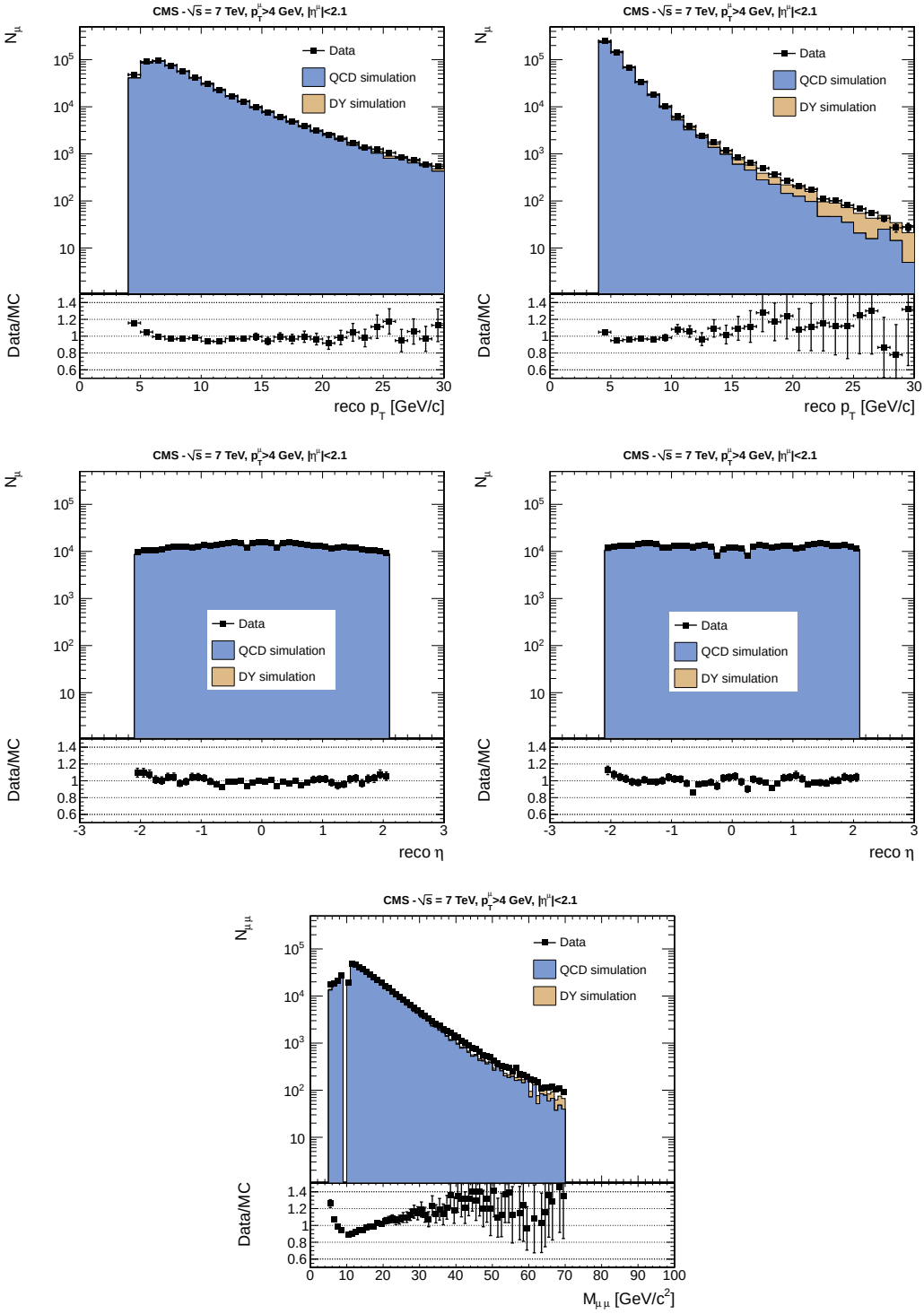

Figure 5.13: Comparison of data and simulation for muons with $p_T > 4$ GeV, together with the ratio Data/MC. The simulation is reweighted according to the fit result and divided in QCD and Drell-Yan (DY) contributions. Top left: p_T of the leading p_T muon. Top right: p_T of the second leading p_T muon. Middle left: η of the leading p_T muon. Middle right: η of the second leading p_T muon. Bottom: Invariant mass of the two muons.

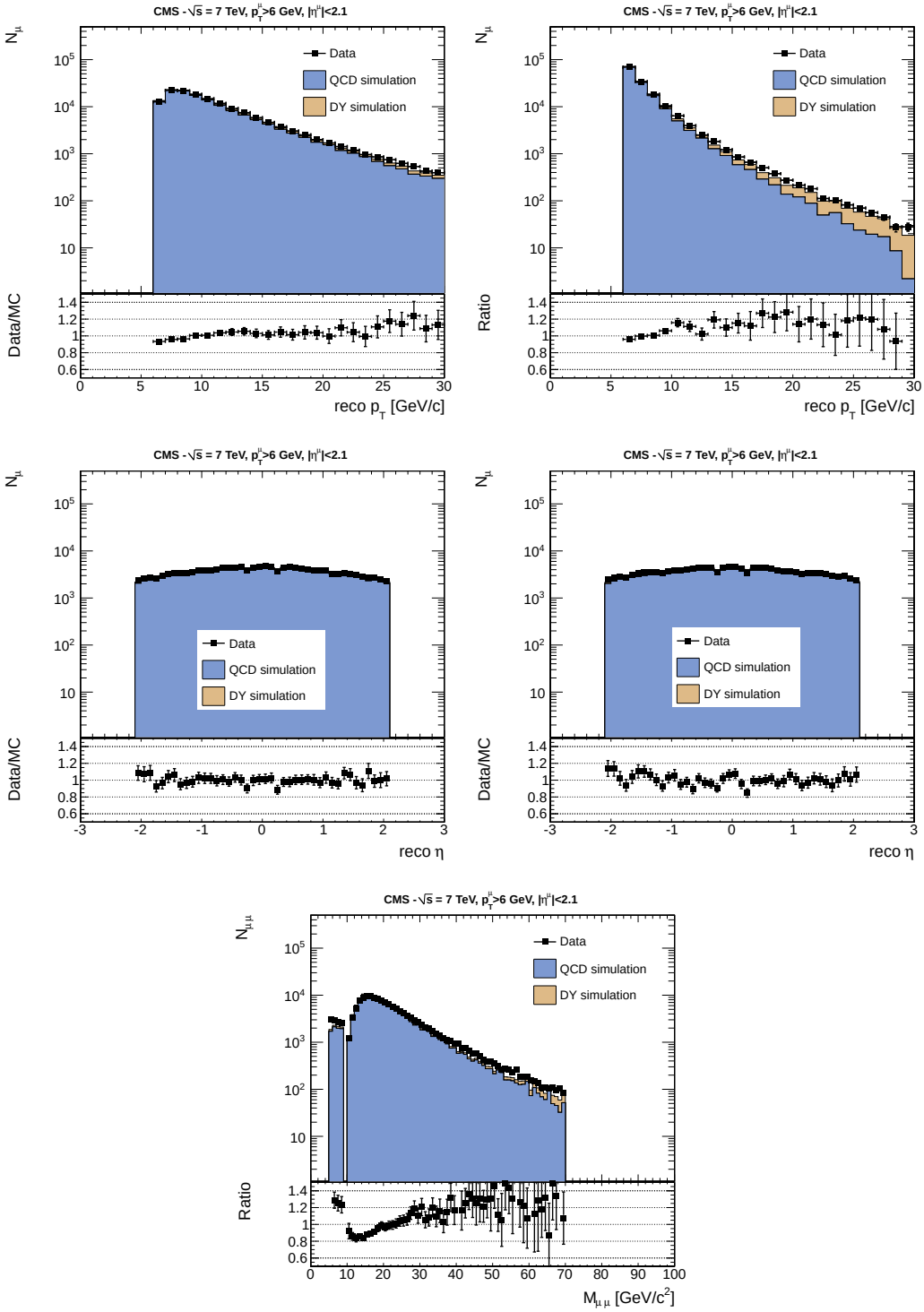

Figure 5.14: Comparison of data and simulation for muons with $p_T > 6$ GeV, together with the ratio Data/MC. The simulation is reweighted according to the fit result and divided in QCD and Drell-Yan (DY) contributions. Top left: p_T of the leading p_T muon. Top right: p_T of the second leading p_T muon. Middle left: η of the leading p_T muon. Middle right: η of the second leading p_T muon. Bottom: Invariant mass of the two muons.

5.5 Efficiency Determination

This Section summarizes the results on the efficiency determination. More details are provided in Appendix A and ref. [68, 67].
The total efficiency ϵ is defined as the fraction of signal events produced within the acceptance ($p_T > 4$ GeV or $p_T > 6$ GeV, $|\eta| < 2.1$ for each muon) that are retained in the analysis. In the simulation, the values of $\epsilon_{\rm MC} = 44.3 \pm 0.1\%$, and $\epsilon_{\rm MC} = 69.9 \pm 0.1\%$, are computed for signal events with a p_T threshold of 4 and 6 GeV respectively.
In order to compare these values to data efficiencies, the selection procedure is divided into three steps, each conditional to the following ones, defined as:

1. muon selection ("MuSel"): events having at least two selected muons, each associated to a good reconstructed vertex;

2. event selection ("EvSel"): events passing the invariant mass cuts, with both muons belonging to the same vertex;

3. trigger selection ("Trg"): events passing the trigger requirements.

The efficiencies obtained by counting the signal events passing each step in the simulation are reported in Table 5.9.

Sample	$\epsilon_{\rm MuSel}$	$\epsilon_{\rm EvSel}$	$\epsilon_{\rm Trg}$	ϵ
$p_T > 4$ GeV, MC	$64.8 \pm 0.1\%$	$78.0 \pm 0.1\%$	$87.7 \pm 0.1\%$	$44.3 \pm 0.1\%$
$p_T > 6$ GeV, MC	$83.6 \pm 0.1\%$	$90.1 \pm 0.1\%$	$92.8 \pm 0.1\%$	$69.9 \pm 0.1\%$
$p_T > 4$ GeV, data	$69.5 \pm 3.6\%$	-	$86.1 \pm 2.0\%$	$48.8 \pm 2.9\%$
$p_T > 6$ GeV, data	$87.0 \pm 3.4\%$	-	$93.4 \pm 2.1\%$	$74.4 \pm 3.8\%$

Table 5.9: Efficiencies (percent) at each step of the analysis in the simulation and in the data averaged over p_T and η bins. The last column reports the overall efficiency, obtained from the product of the three steps; for the data, it also includes the bias and feed-through correction described in the text. Only statistical uncertainties are reported.

The total efficiency can be alternatively expressed on event-by-event basis, defining the efficiency ϵ_i to select the $i^{\rm th}$ signal event as:

$$\epsilon_i = \epsilon_{i,\rm MuSel} \cdot \epsilon_{i,\rm EvSel} \cdot \epsilon_{i,\rm Trg} \tag{5.5}$$

where the subscripts "MuSel", "EvSel" and "Trg" refer to the muon, event and trigger selection steps respectively. The (p_T, η) distribution of the signal events and the efficiency $\epsilon_{i,\rm EvSel}$ can be extracted from simulation only. The efficiencies $\epsilon_{i,\rm MuSel}$ and $\epsilon_{i,\rm Trg}$ can be instead factorized in terms of the single-muon efficiencies, $\epsilon_i = \epsilon_{\mu_1}(p_T, \eta) \cdot \epsilon_{\mu_2}(p_T, \eta)$, under the assumption that the single-muon efficiencies ϵ_{μ_i} only depend on the p_T and η of the muon. The factorization hypothesis is found to be compatible with observed yields in the simulated sample, as reported in Table 5.9.

In the data, the single-muon selection and trigger efficiencies are measured in intervals of p_T and η with the well established "Tag & Probe" method (T&P), as discussed in Appendix A, which employs a sample of $J/\psi \to \mu\mu$ events selected with minimal trigger requirements. The selection efficiency is somewhat larger in the data ($\epsilon^{\rm data}_{\rm MuSel}/\epsilon^{\rm MC}_{\rm MuSel} = 1.073 \pm 0.054$ for $p_T > 4$ GeV and 1.041 ± 0.047 for $p_T > 6$ GeV) as will be explained in Section A.3.2, while the trigger efficiency is consistent with the simulation expectation, within the statistical precision of the method ($\epsilon^{\rm data}_{\rm Trg}/\epsilon^{\rm MC}_{\rm Trg} = 0.982 \pm 0.028$ for $p_T > 4$ GeV and 1.006 ± 0.023 for $p_T > 6$ GeV).

Differences in the kinematic distributions between the J/ψ sample and the $b\bar{b}$ events might imply different bin-averaged efficiencies, causing biases in the region close to the acceptance thresholds. An overall bias correction of 0.966 ± 0.015 (1.004 ± 0.012) is computed when comparing the efficiencies in the simulation computed with the T&P method and those obtained with the signal in the two p_T ranges $p_T > 4$ GeV ($p_T > 6$ GeV).
Another correction to the total efficiency is applied to take into account the feed-through of events where one of the muons has true p_T below the acceptance cut, whereas the reconstructed p_T is above it. This effect has been computed using the simulation, by finding the fraction of selected events having at least one muon generated outside of acceptance, and is equal to 0.990 for $p_T > 4$ GeV and 0.980 for $p_T > 6$ GeV, with negligible errors. The effect of reverse feed-through of events where one of the muons has true p_T above the acceptance cut, whereas the reconstructed p_T is below it is negligible due to the steeply falling p_T spectrum.

The overall efficiency is computed as the product of the step efficiencies for muon selection and trigger, as obtained with T&P in data, times the event selection efficiency computed in the simulation, divided by the bias and the feed-through corrections. Results are reported in the last two lines of Table 5.9.

5.6 Results on the Cross Section Measurement

The cross section within the acceptance range is determined from the observed number of events $\mathcal{N}_{\mu\mu}$, the fraction of signal events in the dimuon sample f_{BB}, the average efficiency for the trigger, muon identification and event selection ϵ, the integrated luminosity $\mathcal{L}$, and the fraction of signal events in the dimuon sample f_{BB} according to the relation:

$$\sigma(pp \to b\bar{b}X \to \mu\mu Y, {p_T}^{1,2} > 4 \text{ or } 6 \text{ GeV}, |\eta^{1,2}| < 2.1) = \frac{\mathcal{N}_{\mu\mu} \cdot f_{BB}}{\epsilon \cdot \mathcal{L}}. \tag{5.6}$$

By applying equation 5.6 we compute the final cross section as

$$\sigma(pp \to b\bar{b}X \to \mu\mu X', {p_T}^{1,2} > 4 \text{ GeV}) = 25.70 \pm 0.14 \text{ (stat.)} \text{ nb}. \tag{5.7}$$

and

$$\sigma(pp \to b\bar{b}X \to \mu\mu X', {p_T}^{1,2} > 6 \text{ GeV}) = 5.03 \pm 0.05 \text{ (stat.)} \text{ nb}. \tag{5.8}$$

where the quoted errors are statistical only.

Chapter 6

Systematic Uncertainties

Several sources of systematic uncertainties have been considered for this measurement. They are divided in: model dependencies for both the signal and the backgrounds, effects related to the impact parameter resolution, uncertainties due to the fit method, and uncertainties related to the measurement of the efficiency, as described in detail below.

6.1 Model Dependent Uncertainties

The transverse impact parameter of a muon produced in a heavy hadron semileptonic decay is connected to the parent hadron proper decay time (t) by the relation expressed in Eq. 3.16. Uncertainties in the parent lifetime affect the proper time distribution t, while uncertainties in the hadron energy spectrum affect the Lorentz boost factor $\beta\gamma$ and the angle δ used in the definition of the transverse impact parameter.

B,C hadron properties: four of the different long-lived B hadrons produced at the LHC decay to muons at non-negligible rate. Their properties are listed in Table 3.2, together with the relevant C hadrons. While the B_d and B_u lifetimes are known with a precision better than 1%, B_s and Λ_b lifetimes are measured with larger uncertainties. Simulated events from B_s and Λ_b decays are re-weighted in turn so as to vary the corresponding lifetimes by their uncertainties [114], templates are recomputed and the fit is then repeated.
A weight (w) is assigned to every impact parameter of the muons coming from the hadron such as

$$w = \frac{e^{-(t/\tau_{new})}/\tau_{new}}{e^{-(t/\tau_{old})}/\tau_{old}} \tag{6.1}$$

where t is the proper decay time of the considered hadron, τ_{old} is its lifetime and $\tau_{new} = \tau_{old} \cdot (1 \pm \tau_{err})$ is the varied lifetime.
The fit result changes by $\pm 2.1\%$ ($\pm 1.5\%$) for $p_T > 4$ GeV ($p_T > 6$ GeV) which is added in quadrature to the systematic uncertainties. The uncertainties on B_d, B_u and c-hadron lifetimes, similarly evaluated, are negligible. Varying the b-hadron and c-hadron sample compositions by two times the uncertainties of the LEP measurements [114, 27] has a smal-

ler effect for both $p_T > 4$ GeV and $p_T > 6$ GeV ($\pm 1.0\%$, $\pm 1.1\%$ respectively).

b-quark properties: uncertainties in the production of B hadrons in the fragmentation of a b-quark affect both the shape of the d_{xy} distribution and the efficiency estimate. The systematic uncertainty is computed as the difference between the reference result and those obtained with two different hadronization models in the PYTHIA simulation: the Lund symmetric [110], and the Peterson [107] functions. The latter has been evaluated for three different values of the ϵ parameter: 0.002, 0.005, 0.007. The results are reported in Table 6.1. By adding linearly the effects on the b templates and those connected with the extraction of the efficiency, overall uncertainties of $\pm 3.3\%$ ($p_T > 4$ GeV) and $\pm 3.6\%$ ($p_T > 6$ GeV) are obtained.

	$p_T > 4$ GeV						
	f_{BB} (%)	ϵ_{MuSel} (%)	ϵ_{EvSel} (%)	ϵ_{Trg} (%)	ϵ_{Tot} (%)	$f_{BB}/\epsilon_{\text{Tot}}$	Syst. (%)
Lund Symmetric	65.10	70.30	78.0	88.15	48.83	1.3333	-
Peterson $\epsilon = 0.002$	64.38	71.39	78.0	88.75	49.92	1.2897	-3.27
Peterson $\epsilon = 0.005$	64.31	71.05	78.0	88.75	49.69	1.2943	-2.92
Peterson $\epsilon = 0.007$	64.98	71.13	78.0	88.65	49.68	1.3079	-2.74
	$p_T > 6$ GeV						
	f_{BB} (%)	ϵ_{MuSel} (%)	ϵ_{EvSel} (%)	ϵ_{Trg} (%)	ϵ_{Tot} (%)	$f_{BB}/\epsilon_{\text{Tot}}$	Syst. (%)
Lund Symmetric	68.99	85.57	90.1	94.59	74.42	0.9271	-
Peterson $\epsilon = 0.002$	67.84	86.52	90.1	95.00	75.56	0.8978	-3.16
Peterson $\epsilon = 0.005$	67.61	86.54	90.1	95.10	75.66	0.8936	-3.61
Peterson $\epsilon = 0.007$	68.77	86.12	90.1	94.89	75.13	0.9153	-1.27

Table 6.1: Systematic uncertainties associated to fragmentation function. Effect on the fit result f_{BB} (left), on the efficiency ε (center) and on the cross section through the combination f_{BB}/ε (right).

The generated p_T distribution of leading and second leading p_T muons in signal events in PYTHIA using the two fragmentation functions are showed in Fig. 6.1.

The dependence of the PDF to describe b-quark production in the pp collision has been evaluated by use 4 different sets: CTEQ6L (standard), MRST2007lomod, MRST2001LO and MRSTMCal. The maximum deviation from the central value obtained considering the change of efficiency and BB fraction in the fit is taken as systematic uncertainties. The results are reported in Table 6.2.
The effect is $\pm 0.9\%$ ($p_T > 4$ GeV) and $\pm 0.5\%$ ($p_T > 6$ GeV).

Light meson decays in flight: muons from K and π decays have different d_{xy} distributions. The shape is also different for light mesons produced in the hadronization of a light quark, or in the decay of a heavy hadron. While a variation of $\pm 30\%$ in the relative amount of charged pions and kaons has a negligible effect, varying the fraction of light mesons from heavy flavour to light flavour by $\pm 50\%$ affects the results by $\pm 2.5\%$ and $\pm 2.6\%$. The effect

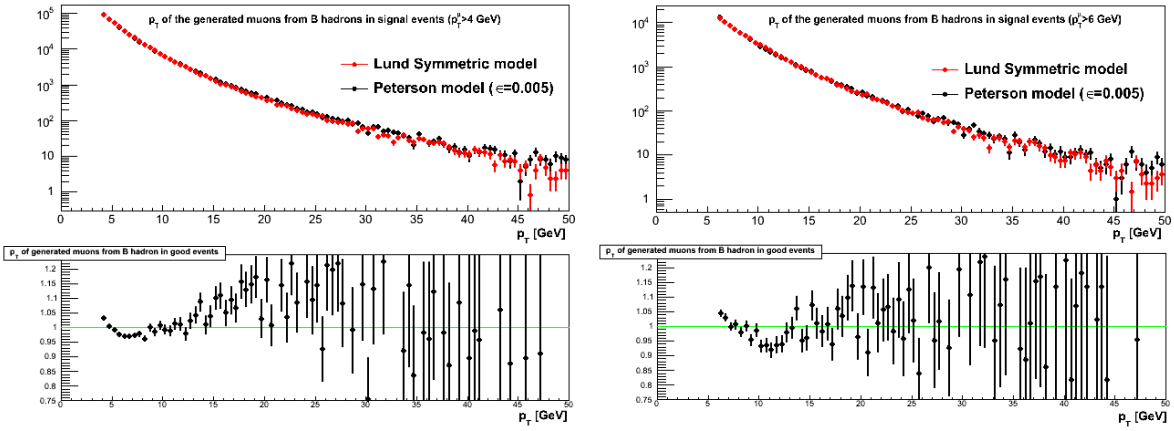

Figure 6.1: Generated p_T distribution of leading and second leading p_T muons in signal events in PYTHIA using the Lund symmetric fragmentation function (red) and the Peterson model with $\epsilon = 0.005$ (black) for muons with $p_T > 4$ GeV (left) and $p_T > 6$ GeV (left). The ratio between the two distributions (Peterson/Lund) are also shown.

	$p_T > 4$ GeV					
	f_{BB}		ε		f_{BB}/ε	
PDF set name	Value	Syst. (%)	Value	Syst. (%)	Value	Syst. (%)
CTEQ6L1 (Standard)	65.10	-	48.33	-	1.3470	-
CTEQ6L	65.29	0.29	48.25	-0.17	1.3532	0.46
MRST2007lomod	64.71	-0.39	48.41	0.17	1.3367	-0.78
MRSTMCal	64.65	-0.69	48.42	0.19	1.3352	-0.88
MRST2001lo	64.75	-0.54	48.32	0.02	1.3400	-0.52
	$p_T > 6$ GeV					
	f_{BB}		ε		f_{BB}/ε	
PDF set name	Value	Syst. (%)	Value	Syst. (%)	Value	Syst. (%)
CTEQ6L1 (Standard)	68.99	-	72.97	-	0.9455	-
CTEQ6L	69.13	0.20	72.98	0.01	0.9472	0.19
MRST2007lomod	68.98	0.01	72.85	-0.16	0.9469	0.15
MRSTMCal	69.02	0.04	72.85	-0.16	0.9474	0.21
MRST2001lo	68.38	0.88	72.69	-0.38	0.9407	-0.50

Table 6.2: Systematic uncertainties associated to PDF. Effect on the fit result f_{BB} (left), on the efficiency ε (center) and on the cross section through the combination f_{BB}/ε (right).

of this variation on the D template is shown in Fig. 6.2. The generator-level filter applied in the simulated sample, requiring two muons produced within the tracker volume in each event, can have an effect on the shape and composition of the decays-in-flight template. The impact on the BB fraction has been evaluated by extracting the same template from an unbiased sample and repeating the fit procedure with the latter. The associated systematic uncertainty is $\pm 0.5\%$ with both p_T selections.

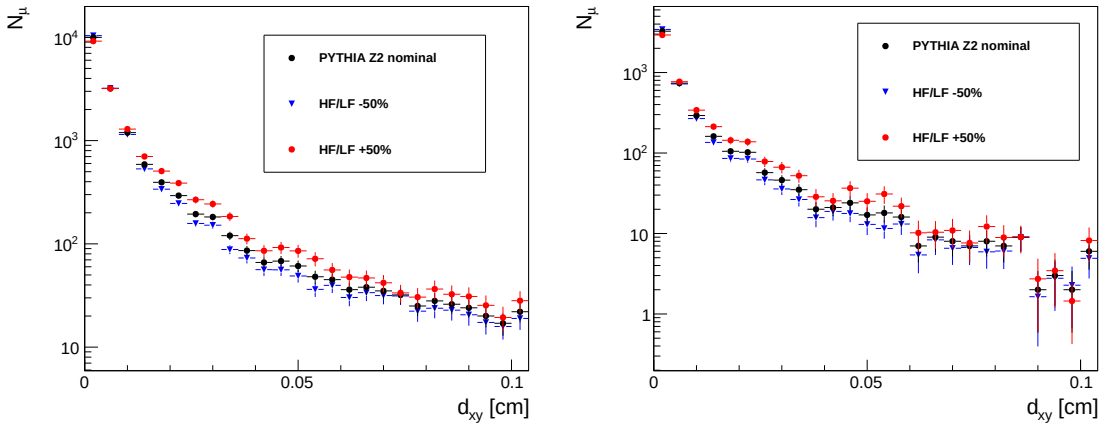

Figure 6.2: Direct comparison of D templates obtained by varying the heavy flavor content compared to the nominal simulation, in the range [0,0.1] cm, for muons with $p_T > 4$ GeV (left) and $p_T > 6$ GeV (right). The distributions are normalized to the same area.

6.2 Uncertainties on the Impact Parameter Resolution

Detector resolution: The resolution of the impact parameter d_{xy} is determined from prompt $\Upsilon(1S) \to \mu^+\mu^-$ decay candidates, reconstructed in real data with sidebands subtraction, and compared to the expected resolution from MC simulation. A slight ϕ dependence in the determination of the signed impact parameter with respect to the beam spot is not reproduced by the simulation.

The combined effect on the analysis due to the misalignment and to the different resolution in data and simulation has been evaluated by an additional smearing of the impact parameter consistent with the observed discrepancies between data and simulation reported in Section 5.3.2. A further check to avoid the region dominated by the resolution has been performed moving the lower bound of the fit range to 40 μm. The maximum of the deviation found with the two methods is 2.7% for $p_T > 4$ GeV and 4.0% for $p_T > 6$ GeV and is taken as systematic uncertainty due to the detector resolution.

6.3 Uncertainties Related to Monte Carlo Statistics and Fit Method

Monte Carlo statistics: the likelihood fit has been validated using a set of 500 parameterized simulated datasets (also called "toy" experiments), each with the same number of events as the real data sample. The procedure is performed in several steps:

1. Extract the 1D impact parameter distributions of the several sources (B,C,P,D)
2. Perform a fit on B,C,P,D
3. Define 1D binned templates (B,C,P,D) by sampling the fit functions
4. Fluctuate with Poissonian statistics all the template bins (for B,C,P,D)
5. Build the 2D symmetrized templates (BB,BC,CC,PP,DD,BD,CD) by combining the fluctuated 1D templates
6. Fluctuate with Poissonian statistics the data-like 2D distribution obtained from MC
7. Perform a fit to the data-like 2D distribution with the "fluctuated" 2D templates

The fit results reproduce the input values with uncertainties consistent with those obtained in data, and the pull distribution is well described by a normal function, as visible in Fig. 6.3. The width of the results obtained for the BB fraction is 0.3% for $p_T > 4$ GeV and 0.7% for $p_T > 6$ GeV, which are taken as the systematic uncertainties related to the limited statistics of the simulated sample.

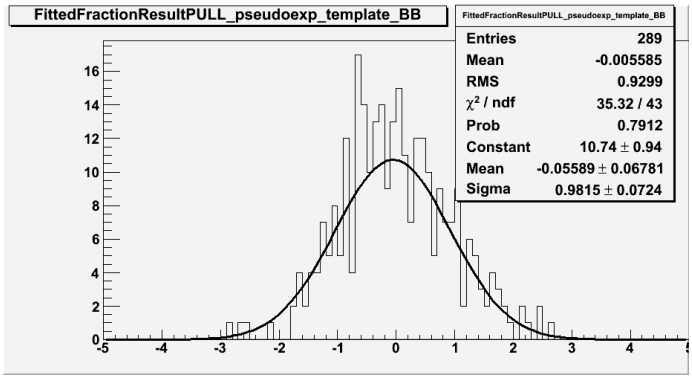

Figure 6.3: BB fraction pull distribution with superimposed Gaussian fit for muons with $p_T > 4$ GeV.

Template parameterization: the d_{xy} distributions of the simulated data used for the fit are smoothed using a superposition of a Gaussian plus one or two exponential functions, depending on the extent of the tail, as described in Section 5.3.3. The associated systematic uncertainty, evaluated by using different parametrizations, is equal to ±0.7% of the final result for both p_T selections. The systematic uncertainty due to the use of symmetrized templates has been estimated to be ±0.6% for $p_T > 4$ GeV and ±0.7% for $p_T > 6$ GeV, by looking at the result obtained in the simulation when a sum of symmetrized templates is used as pseudo-data instead of the usual randomized distribution.

Bin size and fit upper bound: varying the bin size in the range $0.002-0.008$ cm accounts for a systematic uncertainty of 1.0% for $p_T > 4$ GeV and 2.1% for $p_T > 6$ GeV, while varying the fit upper bound in the range $0.15-0.25$ cm accounts for 0.3% for $p_T > 4$ GeV and 0.4% for $p_T > 6$ GeV.

Fit constraints: The non-diagonal fractions BC, BD and CD are constrained to the fitted BB and CC fractions by using the simulation, as described in Section 5.4. A conservative check is obtained by varying the constraints on these fractions by ±50% around the expectation values, that induces a difference of 1.6% for $p_T > 4$ GeV and 1.2% for $p_T > 6$ GeV in the fitted BB fraction. Since the two-dimensional fit neglects the mixing prompt and non-prompt muon components (PB, PC, PD), a further systematic uncertainty is conservatively computed by assigning to the BB fraction an error equal to the missing contributions as found in the simulation (0.7% for $p_T > 4$ GeV and 0.6% for $p_T > 6$ GeV). The total systematic uncertainty related to the fit method is therefore 2.2% for $p_T > 4$ GeV and 2.7% for $p_T > 6$ GeV.

As a consistency check, an unconstrained one-dimensional fit has been performed on the d_{xy} distribution of the muons selected for the analysis, using the templates derived in Section 5.3.1, and its results have been found in agreement within the quoted systematic uncertainty for the two-dimensional fit.

6.4 Efficiencies from Data and Invariant Mass Extrapolation

The statistical uncertainty of the result of Tag & Probe method, which amounts to 6.0% for $p_T > 4$ GeV and 5.2% for $p_T > 6$ GeV, is taken as systematic uncertainty and is propagated to the final result. A complete description of the T&P method is reported in Appendix A.

6.5 Invariant Mass Extrapolation

The invariant mass distribution of the signal in the regions excluded in the analysis is evaluated from simulation and its efficiency correction is taken into account in ϵ_{EvSel}, as explained in Section 5.5. However the invariant mass distribution exhibits a discrepancy when data are compared to simulation rescaled to the fitted fractions in data, as shown in in the bottom part of Figs. 5.13- 5.14, in which the histograms are normalized to the same area. In fact, data is higher than MC in the low- and high-range invariant mass region, while is lower in the mid-range region.

For comparison, the distribution of invariant mass for signal events with two different PYTHIA tunes (Z2, D6T) and MC@NLO is presented in left side of Fig. 6.4. Also in this case a discrepancy is visible, reflected in the ratio between MC@NLO and PYTHIA Z2

shown in the right side of Fig. 6.4. In fact PYTHIA tends to be higher than MC@NLO in the low invariant mass region (and lower in the higher region).

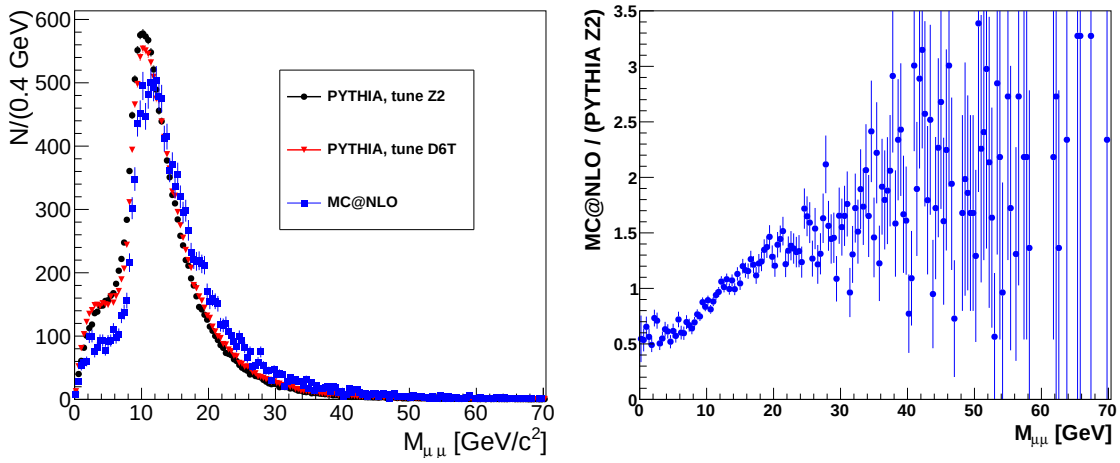

Figure 6.4: Left: generated invariant mass distribution in signal events with two different PYTHIA tunes (Z2, D6T) and MC@NLO. Right: ratio between MC@NLO and PYTHIA Z2 as a function of the invariant mass.

The hierarchy in the low invariant mass region between data, PYTHIA and MC@NLO, has been already observed in CMS within the measurement of $b\bar{b}$ angular correlations [136] outlined in Section 4.1.3. In that case the distribution of the ΔR between the two b's (which is related to the invariant mass of the two muons used in this analysis) is measured in data and simulation and the ratio with respect to PYTHIA is presented, normalized in the high ΔR range. In fact Fig. 4.3 shows that data tend to be higher than PYTHIA in the low part of the ΔR spectrum, while MC@NLO tends to be lower.

For this reason MC@NLO is not used to compute the systematic uncertainty associated to the invariant mass cut. Instead, the difference observed in the invariant mass regions excluded in the analysis between PYTHIA and data is conservatively attributed to the $b\bar{b}$ signal events.

In detail we divide the simulated invariant mass range in 4 parts:

- the range $0 < M_{\mu\mu} < 5$ GeV (the low invariant mass which is excluded in the analysis to reject muons from the same b-quark), with M_0 events,
- the range $5 < M_{\mu\mu} < 8.9$ GeV (the invariant mass region which exhibits the discrepancy between data and simulation), with N_0 events
- the range $8.9 < M_{\mu\mu} < 10.6$ GeV (the invariant mass region which is excluded in the analysis due to Υ), with P_0 events,

- the range $10.6 < M_{\mu\mu} < \infty$ GeV (the high invariant mass region), with Q_0 events.

The invariant mass cut efficiency is computed as the ratio:

$$\epsilon_0 = \frac{N_0 + Q_0}{M_0 + N_0 + Q_0 + P_0} \tag{6.2}$$

and is taken into account in the cross section formula.
The systematic uncertainty is then computed in the following way. Every region is normalized to data such as M_0 is normalized in the range $[5.0, 5.1]$ GeV (i.e. we consider the discrepancy between 0 and 5 GeV to be the same as that observed around 5 GeV), N_0 is normalized in the range $[5.0, 8.9]$ GeV, P_0 is normalized to the mean of the ranges $[8.8, 8.9]$ GeV and $[10.6, 10.7]$ GeV (i.e. we consider the discrepancy between 8.9 and 10.6 GeV to behave linearly), Q_0 is normalized in the range $[10.6, \infty]$ GeV:

$$SF_M = \frac{\int_5^{5.1} M_{\mu\mu}^{DATA}}{\int_5^{5.1} M_{\mu\mu}^{MC}} \tag{6.3}$$

$$SF_N = \frac{\int_5^{8.9} M_{\mu\mu}^{DATA}}{\int_5^{8.9} M_{\mu\mu}^{MC}} \tag{6.4}$$

$$SF_P = \frac{1}{2}\left(\frac{\int_{8.8}^{8.9} M_{\mu\mu}^{DATA}}{\int_{8.8}^{8.9} M_{\mu\mu}^{MC}} + \frac{\int_{10.6}^{10.7} M_{\mu\mu}^{DATA}}{\int_{10.6}^{10.7} M_{\mu\mu}^{MC}}\right) \tag{6.5}$$

$$SF_Q = \frac{\int_5^{8.9} M_{\mu\mu}^{DATA}}{\int_5^{8.9} M_{\mu\mu}^{MC}} \tag{6.6}$$

The results are displayed in Table 6.3.

Table 6.3: Systematic uncertainties on the cross section measurements

	$p_T > 4$ GeV	$p_T > 6$ GeV
ϵ_0	0.76	0.92
SF_M	1.32	1.70
SF_N	1.04	1.43
SF_P	0.90	1.00
SF_Q	0.99	0.98
ϵ	0.75	0.89

Then we define the rescaled regions $M = M_0 \cdot SF_M$, $N = N_0 \cdot SF_N$, $P = P_0 \cdot SF_P$, $Q = Q_0 \cdot SF_Q$ and compute the new invariant mass cut efficiency as:

$$\epsilon = \frac{N + P}{M + N + Q + P} \tag{6.7}$$

so that the systematic uncertainty related to the invariant mass extrapolation is defined as $1 - \epsilon/\epsilon_0$. For muons with $p_T > 4$ GeV the systematic uncertainty is 1.1%, while for muons with $p_T^\mu > 6$ GeV is 3.3%.

6.6 Absolute Normalization and Overall Systematic Uncertainty

The systematic uncertainties due to the analysis technique sum up (in quadrature) to 8.6% for $p_T > 4$ GeV and 9.2% for $p_T > 6$ GeV. The last source of systematic to be considered is related to the integrated luminosity of the dimuon data sample used. It is provided by carrying out Van der Meer scans, wherein the beam sizes are determined by measuring the interaction rate as a function of the beam separation and combining these measurements with measurements of the beam current to determine the absolute luminosity via the relation

$$\mathcal{L} = \frac{N_1 N_2 f}{2\pi\sigma_x\sigma_y} \tag{6.8}$$

where N_1 and N_2 are the number of protons in the two beams, f is the frequency with which the bunches collide, and σ_x and σ_y are the effective beam sizes in the horizontal and vertical scan plans, respectively. With this procedure it is possible to determine the absolute luminosity with 4% precision [152].

The total systematic uncertainty is therefore 9.4% for $p_T > 4$ GeV and 10.1% for $p_T > 6$ GeV. All the contributions to the total systematic error are summarized in Table 6.6.

Table 6.4: Total systematic uncertainties

	$p_T > 4$ GeV		$p_T > 6$ GeV	
Source	Comment	σ ($\pm$%) syst.	Comment	σ ($\pm$%) syst.
b lifetimes	-	2.1%	-	1.5%
b fractions	uncert. doubled	1.0%	uncert. doubled	1.1%
Fragmentation	-	3.3%	-	3.6%
PDF sets	-	0.9%	-	0.5%
D template HF/LF d.i.f. ratio	$\pm$50%	2.5%	$\pm$50%	2.6%
Unbiased D template	-	0.5%	-	0.5%
Model dependency	4.9%		4.9%	
Detector resolution	2.7%		4.0%	
MC statistics	500 toy	0.3%	500 toy	0.7%
Template parametrization	-	0.7%	-	0.7%
Use of symmetrized templates	-	0.6%	-	0.7%
Bin width	$20 - 80$ μm	1.0%	$20 - 80$ μm	2.1%
Fit upper range	$0.15 - 0.25$ cm	0.3%	$0.15 - 0.25$ cm	0.4%
Fit constraints	$\pm$50%	1.6%	$\pm$50%	1.2%
Missing PX	-	0.7%	-	0.6%
Fit method	2.2%		2.7%	
T&P	-	6.0%	-	5.2%
Invariant mass extrapolation	-	1.1%	-	3.3%
Efficiencies and normalization	6.1%		6.2%	
Analysis technique syst. uncert.	8.6%		9.2%	
$\mathcal{L}$	4.0%			
Total systematic uncertainty	9.4%		10.1%	

Chapter 7

Results and Comparison with QCD Predictions

By applying equation 5.6 and taking into account the systematic uncertainties discussed in the previous Chapter we compute the final $pp \to b\bar{b}X \to \mu\mu X'$ cross sections as

$$\sigma({p_T}^{1,2} > 4 \text{ GeV}) = 25.70 \pm 0.14 \text{ (stat.)} \pm 2.20 \text{ (syst.)} \pm 1.03 \text{ (lumi.)} \text{ nb}, \quad (7.1)$$
$$\sigma({p_T}^{1,2} > 6 \text{ GeV}) = 5.03 \pm 0.05 \text{ (stat.)} \pm 0.46 \text{ (syst.)} \pm 0.20 \text{ (lumi.)} \text{ nb}. \quad (7.2)$$

The cross sections predicted by the PYTHIA simulation are:

$$\sigma_{\text{PYTHIA}}({p_T}^{1,2} > 4 \text{ GeV}) = 48.2 \pm 0.1 \text{ nb}, \quad (7.3)$$
$$\sigma_{\text{PYTHIA}}({p_T}^{1,2} > 6 \text{ GeV}) = 9.25 \pm 0.04 \text{ nb}. \quad (7.4)$$

where the errors are statistical only. The fact that PYTHIA predicts a cross section value higher than the one measured in data has also been noticed in previous analyses [132], and is confirmed by our present findings.

7.1 Comparison with NLO QCD Predictions

The NLO QCD prediction for this measurement has been obtained with the next-to-leading-order event generator MC@NLO, interfaced to HERWIG for the parton hadronization and decays, as introduced in Section 3.6. CTEQ6.6 PDF set and b-quark mass parameter $m_b = 4.75$ GeV have been used, without underlying event simulation. A total of 25×10^6 $b\bar{b}$ events has been generated.

The predicted inclusive $b\bar{b}$ cross section is $\sigma_{b\bar{b}} = (2.4199 \pm 0.0008) \times 10^5$ nb. The predicted cross sections for the process $pp \to b\bar{b}X \to \mu\mu X'$ are

$$\sigma_{\text{MC@NLO}}({p_T}^{1,2} > 4 \text{ GeV}) = 19.66 \pm 0.29 \text{ nb}, \quad (7.5)$$
$$\sigma_{\text{MC@NLO}}({p_T}^{1,2} > 6 \text{ GeV}) = 4.40 \pm 0.14 \text{ nb}. \quad (7.6)$$

A scan of the MC@NLO predictions for $b\bar{b}$ pairs decaying into muons as a function of the p_T cut is shown in Fig. 7.1, for events in which only one or both the muons are required to satisfy the selection criterion.

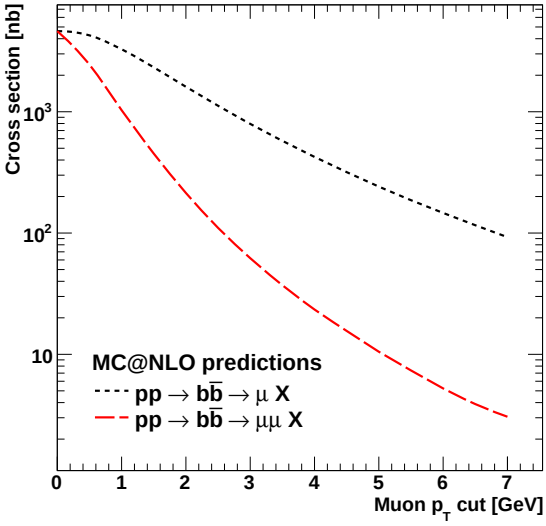

Figure 7.1: Scan of the MC@NLO predictions for $b\bar{b}$ pairs decaying into muons as a function of the p_T cut for events in which only one (black) or both (red) the muons are required to satisfy the selection criterion.

The systematic uncertainties for $\sigma(pp \to b\bar{b}X \to \mu\mu X')$ have been obtained by varying the b-quark mass between 4.5 GeV and 5 GeV and by using the PDF set MSTW2008 [153]. The value of the scale uncertainty is obtained by varying the QCD renormalization (f_{Ren}) and factorization (f_{Fact}) scales as described in Section 3.7. The results are reported in Table 7.1.

	$p_T > 4$ GeV		$p_T > 6$ GeV	
Changed parameter	σ_{bb} [nb]	Variation (%)	σ_{bb} [nb]	Variation (%)
nominal	19.66 ± 0.29	-	4.40 ± 0.14	-
m_b=4.5	20.67 ± 0.32	+5.1	4.71 ± 0.14	+7.0
m_b=5	19.22 ± 0.25	−2.2	4.51 ± 0.15	−2.5
f_{Ren}=0.5	25.85 ± 0.47	+31.5	5.36 ± 0.12	+21.8
f_{Ren}=2	15.89 ± 0.19	−19.2	3.57 ± 0.22	−18.9
f_{Fact}=0.5	18.05 ± 0.21	−8.2	4.33 ± 0.09	−1.6
f_{Fact}=2	21.37 ± 0.38	+8.7	4.71 ± 0.10	+7.0
pdf MSTW2008	20.71	+0.76	-	-

Table 7.1: Results of MC@NLO systematic uncertainties.

The predicted cross sections are therefore

$$\sigma_{\mathrm{MC@NLO}}(p_T > 4\ \mathrm{GeV}) = 19.66 \pm 0.29\ (\mathrm{stat.})\ ^{+6.50}_{-4.12}\ (\mathrm{syst.})\quad \mathrm{nb}, \tag{7.7}$$

$$\sigma_{\mathrm{MC@NLO}}(p_T > 6\ \mathrm{GeV}) = 4.40 \pm 0.14\ (\mathrm{stat.})\ ^{+1.05}_{-0.84}\ (\mathrm{syst.})\quad \mathrm{nb}. \tag{7.8}$$

Both values are compatible with the measured results within the theoretical and experimental uncertainties. A summary of b-quark production cross section measurements performed within the CMS experiment and compared to the MC@NLO predictions is reported in figure 7.2 for exclusive and inclusive final states.

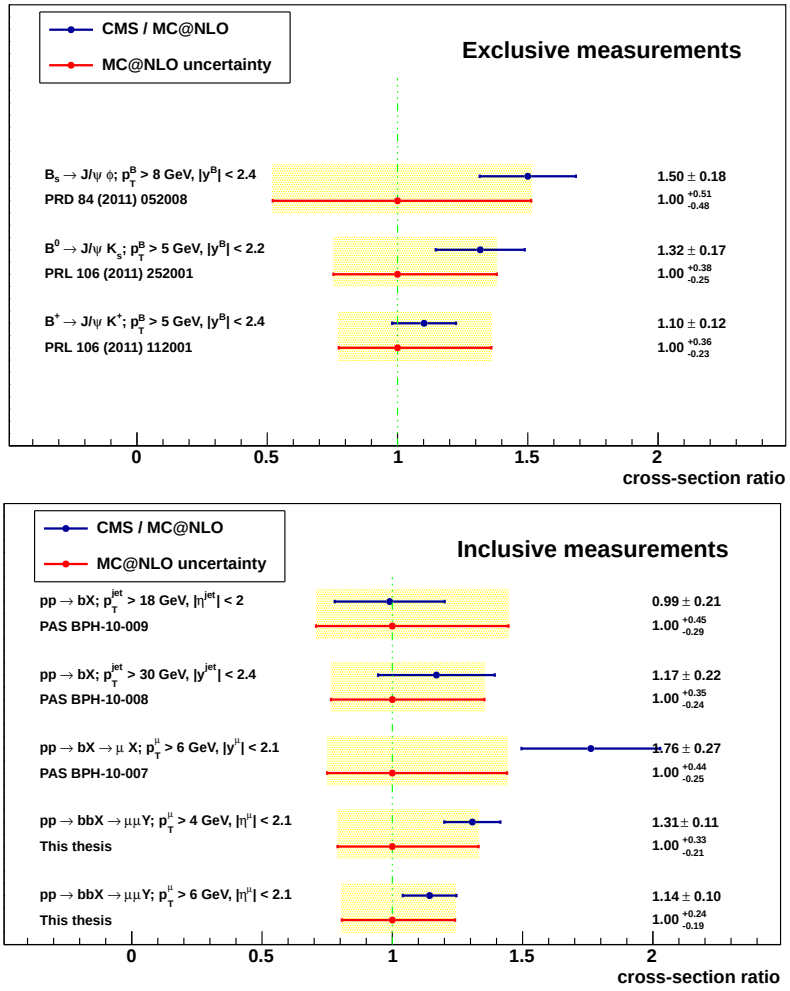

Figure 7.2: Summary of b-quark production cross section measurements performed within the CMS experiment. The ratio with respect to the MC@NLO prediction is shown, together with the total uncertainty. Top: exclusive measurements. Bottom: inclusive measurements.

7.1.1 Considerations on the NLO QCD Predictions

The MC@NLO scale uncertainty related to the prediction for this measurement is smaller than other b-quark measurement already performed in CMS. This is mainly due to the suppression of the gluon splitting contribution to the total cross section in the final state considered here, as can be argued from the simple kinematical considerations already discussed in Section 5.1.

For completeness, a scan of the different systematic uncertainty source related to the MC@NLO prediction as a function of the p_T cut applied to the muons is shown in Fig. 7.3. The relative scale variation as a function of the symmetric p_T threshold compared to the scale variation obtained by imposing a p_T cut on a single muon is reported in the same figure.

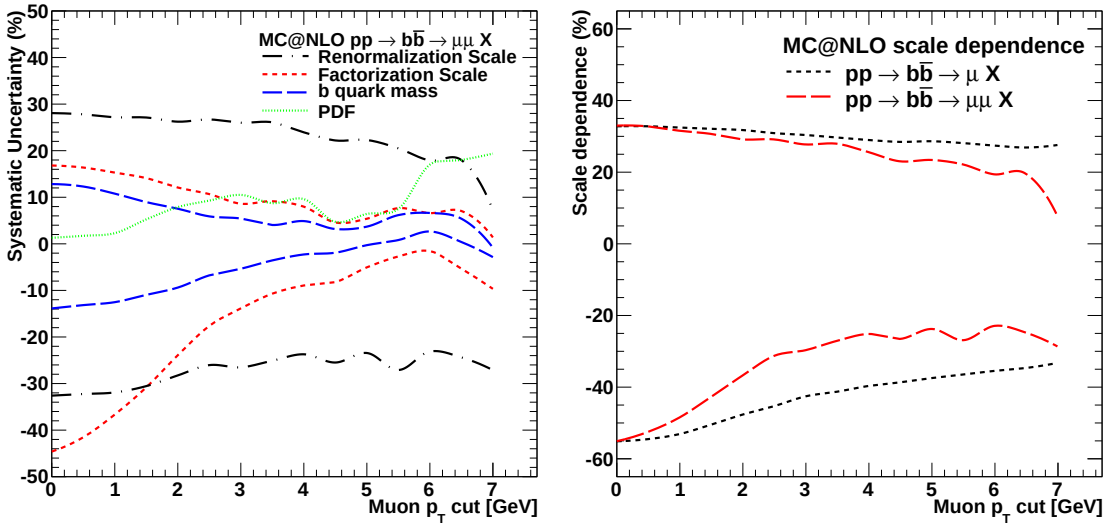

Figure 7.3: Left: scan of the different systematic uncertainty sources related to the MC@NLO prediction as a function of the p_T cut applied to the muons. Right: scan of the relative scale variation as a function of the symmetric p_T threshold (red) compared to the scale variation obtained by imposing a p_T cut on a single muon (black).

Chapter 8

Conclusions

The main result of this thesis is a measurement of the inclusive beauty quark cross section based on the semileptonic decay of b quarks into muons with the process $pp \to b\bar{b}\mathrm{X} \to \mu\mu\mathrm{Y}$ at $\sqrt{s} = 7$ TeV. It is based on an integrated luminosity of $27.9\,\mathrm{pb}^{-1}$ collected by the CMS detector at the CERN LHC collider during the first months of high-energy collision data-taking in the second half of year 2010.

Due to the large b-quark production cross section, high statistics data samples are available soon after the LHC startup. This makes the CMS experiment an excellent facility for the study of heavy flavor physics. Even though the CMS detector is primarily designed for high transverse momentum physics, it is very well suited for heavy flavor physics thanks to the muon system capable to identify low transverse momentum muons and the excellent tracking detectors. The investigation of events containing beauty quarks probes the predictions of the theory of strong interactions at the energy scale provided by the LHC. Furthermore, the production of b quarks is a major source of background for many searches to be performed at the LHC and therefore needs to be well understood.

Because of the relatively long lifetime of the b-quark, muons from semileptonic b-decays have larger transverse impact parameter (d_{xy}) than muons from the decay of lighter quarks. The contribution of $b\bar{b}$-events to the measured distribution is determined by performing a fit based on simulated template distributions for signal and background events.

Selecting pairs of muons with pseudorapidity $|\eta| < 2.1$, the value

$$\sigma({p_T}^{1,2} > 4 \text{ GeV}) = 25.70 \pm 0.14 \text{ (stat.)} \pm 2.20 \text{ (syst.)} \pm 1.03 \text{ (lumi.)} \text{ nb}, \tag{8.1}$$

is obtained for muons with transverse momentum $p_T > 4$ GeV and

$$\sigma({p_T}^{1,2} > 6 \text{ GeV}) = 5.03 \pm 0.05 \text{ (stat.)} \pm 0.46 \text{ (syst.)} \pm 0.20 \text{ (lumi.)} \text{ nb}. \tag{8.2}$$

for muons with $p_T > 6$ GeV. This result is very precise compared to previous ones and to the scale uncertainty of the theory prediction.

The tools developed for the analysis presented here can be applied to a wide range of topics other than b cross section measurements. Future perspectives include the measurement of the time integrated mixing probability and a study of the like-sign dimuon charge asymmetry.

Appendix A

Acceptance and Efficiency Computation

A.1 Acceptance

The acceptance is defined to be equal to the phase space of our signal (i.e. $p_T^\mu > 4$ GeV or $p_T^\mu > 6$ GeV and $|\eta^\mu| < 2.1$). As reported in Section 5.5, the feed-through of events having muons generated outside the acceptance cuts but reconstructed inside is estimated with an event counting procedure in simulated signal sample. The fraction of selected events having at least one muon generated outside of acceptance, and is equal to 0.990 for $p_T > 4$ GeV and 0.980 for $p_T > 6$ GeV, with negligible statistical errors. The effect of reverse feed-through of events where one of the muons has true p_T above the acceptance cut, whereas the reconstructed p_T is below is negligible.

A.2 MC truth efficiency on BB signal events

A.2.1 Event Counting vs Single-particle Factorization

In order to find the event selection efficiency from Monte Carlo truth, we consider all the generated events corresponding to our signal definition, therefore containing at least two generated muons within the acceptance cuts ($p_T > 4$ GeV or $p_T > 6$ GeV and $|\eta| < 2.1$), coming from the decay of two different b quarks. According to PYTHIA about 1% of the signal events contain two $b\bar{b}$ pairs produced in double gluon splitting process. The number of selected events is 209 518 for $p_T > 4$ GeV and 60 764 for $p_T > 6$ GeV.

The event selection efficiency is found in three steps, starting from all the generated signal events and finding:

1. N_{MuSel}, signal events that have at least two reconstructed muons satisfying the single-muon identification requirements defined in Section 5.2;

2. N_{EvSel}, events further satisfying dimuon selection cuts (e.g. invariant mass, association to the same vertex, presence of other muon pairs in the same event).

3. N_{Trg}, events accepted in addition by the trigger;

Thus, the global event selection efficiency can be factorized as:

$$\varepsilon_{TOT} = \varepsilon_{MuSel} \cdot \varepsilon_{EvSel} \cdot \varepsilon_{Trg}, \tag{A.1}$$

where each factor is found from the number of events defined above:

$$\varepsilon_{MuSel} = \frac{N_{MuSel}}{N_{Gen}},\ \varepsilon_{EvSel} = \frac{N_{EvSel}}{N_{Trg}},\ \varepsilon_{Trg} = \frac{N_{Trg}}{N_{MuSel}}. \tag{A.2}$$

The second term in the formula, ε_{EvSel}, cannot be expressed as a function of the single-muon efficiencies, since it depends on multiple-particle observables like the dimuon invariant mass, the association of both muons to the same vertex and the possible presence of other muon pairs in the same event; hence it will be evaluated from MC simulation.

The first and third terms, instead, can be factorized as a function of the single-particle efficiencies to allow a comparison with the Tag & Probe (T&P) results described below, and to compute the efficiency correction adjusting the simulation to the data.
If an event has $N^{\mu}_{Gen} \geq 2$ generated muons, the probability to have at least two of them being reconstructed and passing the selection cuts is:

$$P_{MuSel}(\geq 2) = 1 - \left[P_{MuSel}(0) + P_{MuSel}(1)\right], \tag{A.3}$$

where $P_{MuSel}(0)$ and $P_{MuSel}(1)$ are the probabilities to have exactly 0 and only 1 selected muon. If we assume that the probability $P^{\mu}_{Sel,i}\left(\eta_i, p_{Ti}\right)$ to select the i-th muon depends only on the η and p_T of the muon but not on the presence of other muons in the event, then $P_{MuSel}(0)$ and $P_{MuSel}(1)$ can be expressed as:

$$\begin{aligned} P_{MuSel}(0) &= \prod_{i=1}^{N^{\mu}_{Gen}} \left(1 - P^{\mu}_{Sel,i}\right), \\ P_{MuSel}(1) &= \sum_{i=1}^{N^{\mu}_{Gen}} \left[P^{\mu}_{Sel,i} \cdot \prod_{\substack{j=1 \\ j\neq i}}^{N^{\mu}_{Gen}} \left(1 - P^{\mu}_{Sel,j}\right) \right]. \end{aligned}$$

The single-particle selection probability for each of the selected muons in an event passing step 1 (N_{MuSel}), is expressed as a function of the single-μ efficiencies as $P^{\mu}_{Sel,i} = \varepsilon^{\mu}_{Trk,i} \cdot \varepsilon^{\mu}_{RecoSel,i}$, where $\varepsilon^{\mu}_{Trk,i}$ is the efficiency to reconstruct the inner track of the i-th muon, and $\varepsilon^{\mu}_{RecoSel,i}$ is the efficiency of the muon reconstruction, including quality cuts.

We can find $P_{MuSel}(\geq 2)$ for each generated signal event, and sum it over the whole sample to get the number of events passing our cuts with single muon factorized efficiencies to be compared with the simple event counting. The sum gives the expected number of events with at least 2 selected muons, coming from the efficiency factorization:

$$N'_{MuSel} = \sum_{k=1}^{N_{Gen}} P_{MuSel}(\geq 2)_k = \sum_{k=1}^{N_{Gen}} \{1 - [P_{MuSel}(0)_k + P_{MuSel}(1)_k]\}\,. \tag{A.4}$$

The estimated event selection efficiency is:

$$\varepsilon'_{MuSel} = \frac{N'_{MuSel}}{N_{Gen}}. \tag{A.5}$$

The scaling factor for this single-particle factorized efficiency with respect to the one found with the event counting is:

$$SF'_{MuSel} = \frac{\varepsilon'_{MuSel}}{\varepsilon_{MuSel}} = \frac{N'_{MuSel}}{N_{MuSel}}. \tag{A.6}$$

The trigger efficiency correction is computed in the same way.
We compare single-muon efficiency results from different sources:

1. **MCTruthBB**: genuine signal events;
2. **MCTruth**: MC truth in J/ψ events used to run the T&P;
3. **MC**: T&P applied to simulated J/ψ events;
4. **Data**: T&P applied to real J/ψ events.

The efficiencies in the **MCTruthBB** case are found in the following way. We start from all the generated muons in acceptance coming from B decays, and associate each of them to a inner track. The association is arbitrated using the quality of the association by hits (or the minimum ΔR in case of equal quality) to get the most reliable link between a reconstructed track and a generated particle. The tracking efficiency (as a function of the generated p_T and η) is equal to the ratio between the number of associated tracks and the number of generated muons. The selection efficiency is obtained from the fraction of reconstructed tracks positively identified as muons.

Table A.1 shows the number of events contained in the generated MC sample containing signal muons with $p_T^\mu > 4$ GeV and $p_T^\mu > 4$ GeV, together the number of events after each selection steps. The single step and total efficiencies and the scaling factor obtained using the single-particle MCTruthBB efficiencies are reported in the same table
By switching the sequence of the Trigger and Event selection cuts, the results are still compatible with the simple event counting uncertainties, ensuring the validity of the factorization approach.

	Generated events	N_{MuSel}	N_{EvSel}	N_{Trg}
$p_T > 4$ GeV				
Event counting	209518	135680	105810	92792
Step efficiency	-	$64.8 \pm 0.1\%$	$78.0 \pm 0.1\%$	$87.7 \pm 0.1\%$
Total efficiency	-	$64.8 \pm 0.1\%$	$50.5 \pm 0.1\%$	$44.3 \pm 0.1\%$
$SF_{MCTruthBB}$	-	$0.997^{+0.022}_{-0.035}$	-	$1.019^{+0.012}_{-0.027}$
$p_T > 6$ GeV				
Event counting	60764	50690	45782	42506
Step efficiency	-	$83.6 \pm 0.1\%$	$90.1 \pm 0.1\%$	$92.8 \pm 0.1\%$
Total efficiency	-	$83.6 \pm 0.1\%$	$75.3 \pm 0.1\%$	$69.9 \pm 0.1\%$
$SF_{MCTruthBB}$	-	$1.020^{+0.027}_{-0.064}$	-	$1.000^{+0.046}_{-0.017}$

Table A.1: Number of events for muons with $p_T > 4$ GeV and $p_T > 4$ GeV contained in the generated MC sample and in each of the selection steps together with the respective scaling factor obtained using the single-particle MCTruthBB efficiencies.

A.3 Efficiencies with T&P from J/Ψ

The scaling factors obtained with the MCTruthBB efficiencies are compatible with 1, ensuring that the single-particle efficiency factorization is not introducing any sizeable bias. The single muon efficiency has been computed also with the "Tag & Probe" method (T&P) method as described in [68, 67, 154].
This data-driven method can be applied to determine the relative efficiency of a selection with respect to a strictly looser one.

1. The looser selection is used to define the *probe* muons.

2. Probes are then separated into two classes, *passing* and *failing* probes, according to the tighter selection.

3. A third separate selection, usually very tight, is used to define *tag* muons. The tag and probe selections are inclusive, i.e. a muon can be at the same time tag and probe, only a tag, only a probe or none.

4. Dimuon candidates are made by pairing tag muons with probe muons, requiring the invariant mass of the pair to be close to the resonance mass (J/ψ, Z etc.), and the total charge to be zero.

5. Some procedure is applied at the *tag+probe* invariant mass spectra for the passing and failing probes in order to subtract the non-resonant background (e.g. from fake probes) to estimate the net number of passing and failing dimuon probes.

6. The efficiency is determined by the fraction of tag+probe pairs for which the probe passes the tighter selection.

In this study the invariant mass distribution is fitted with the sum of two functions, one representing the signal contribution (a double Gaussian for the tracking efficiency and a Crystal Ball [155] for the muon related efficiencies), and third grade Chebyshev polynomial for the background. The fit the two line-shapes for probes passing and failing the muon selection is performed simultaneously, constraining the shapes to be equal in the two data-sets, for each bin of the probe η and p_T.

The combined trigger and offline reconstruction efficiency for a single muon is measured on data and MC and is defined as:

$$\epsilon(\mu) = \epsilon_{\text{track}} \cdot \epsilon_{\text{MuId} \mid \text{track}} \cdot \epsilon_{\text{trig} \mid \text{MuId}} \tag{A.7}$$

where ϵ_{track} is the tracking efficiency, $\epsilon_{\text{MuId} \mid \text{track}}$ is the muon identification in the muon systems for a tracker-reconstructed muon, and $\epsilon_{\text{trig} \mid \text{MuId}}$ is the probability for an offline reconstructed muon to have also fired the trigger. The measured efficiencies are found to be symmetric in the two halves of the detector within the statistical uncertainties, in agreement with the expectations, so for the final results the two regions have been combined and the result is reported as a function of $|\eta|$ instead of η.

A.3.1 Tracking efficiency

By itself, the tracking efficiency ϵ(track) is not a relative efficiency and thus can't be directly measured using tag and probe. Anyway, by assuming that the muon reconstructions in the tracker and in the muon system are independent, ϵ(track) can be estimated as ϵ(track|sta), the probability that a inner tracker track can be found and associated to a given standalone muon probe. The latter efficiency can be measured with the T&P.

In order to perform the measurement, events have been selected from the HLT L1DoubleMuOpen trigger path (which does not use the inner tracker), and the following definitions are used:

- *silicon track*: a track from the `generalTracks` collection. A kinematic preselection is applied to discard tracks which are by far too soft to reach the muon system ($p_T < 2$ GeV/c for $|\eta| < 1.0$, $p < 2$GeV/c otherwise).
- *tag*: a global muon with $p_T > 2.6$ GeV/c, associated to one of the two legs of a HLT L1DoubleMuOpen trigger ($\Delta R \leq 0.3$ between the L1 position and the extrapolated crossing of the tracker track of the global muon with the second muon station).
- *probe*: any stand-alone muon except those with no valid hits at all[1].
- *passing probe*: those standalone muons which can be matched to at least one silicon track (or tight silicon track) by comparing the two track directions at the point of closest approach to the beam line; the matching is defined by $|\delta\eta| < 0.2$ and $\Delta R < 0.5$.

[1] A muon with no valid hits is a set of segments in the muon stations which are loosely compatible with a track hypothesis but which are not fitted using the Kalman filter like other muons

The statistical separation between the signal and the non-resonant background is achieved by performing a fit of the (tag+passing probe) and (tag+failing probe) line-shapes. The signal is modelled as a double Gaussian, and the background as a third order Chebyshev polynomial.

The measurement of the tracking efficiency based on the matching between the two sub-detectors presents two complications: the possibilities that the track is successfully reconstructed in the inner tracker but not associated to the standalone muon, and the possibility that the standalone muon is associated to a spurious tracker track when the correct one is not reconstructed. The former possibility can lead to an underestimation of the efficiency, and can be mitigated by choosing very loose matching criteria; the latter possibility leads to an overestimation of the efficiency, and becomes larger if the matching criteria is made looser. The two effects have to be under control in order to measure the tracking efficiency to the percent accuracy, or if large deviations between simulations and real data are expected.

The measured efficiency ϵ can be expressed in terms of the true tracking efficiency ϵ_T, matching efficiency ϵ_M and the probability of spurious matches, hereafter referred to as "fake rate", ϵ_F as

$$\epsilon = \epsilon_T \epsilon_M \ + \ (1 - \epsilon_T \epsilon_M)\epsilon_F \tag{A.8}$$

As it will be explained later, ϵ_F can be measured on data. Once ϵ_F is known, one can invert the relation and obtain

$$\epsilon_T \epsilon_M = \frac{\epsilon - \epsilon_F}{1 - \epsilon_F} = 1 - \frac{1 - \epsilon}{1 - \epsilon_F} \tag{A.9}$$

that is, the true inefficiency is equal to the measured inefficiency scaled up by a factor $1/(1 - \epsilon_F)$. One can also compute the uncertainty on the corrected efficiency

$$\sigma(\epsilon_M \epsilon_T) = \frac{1}{1 - \epsilon_F}\,\sigma(\epsilon) \ \oplus \ \frac{1 - \epsilon}{(1 - \epsilon_F)^2}\,\sigma(\epsilon_F) \tag{A.10}$$

The effect of non-negligible ϵ_F is therefore to decrease the sensitivity of the measurement, as expected, but contribution of the uncertainty on ϵ_F to the precision of the measurement is small because of the suppression factor $(1 - \epsilon) \ll 1$.

Extracting ϵ_T from $\epsilon_M \epsilon_T$ can be more problematic. The value of ϵ_M can only be extracted from simulation, not from data, and it is sensitive to the tails of the standalone muon resolution. There is no suppression factor reducing the contribution of $\sigma(\epsilon_M)$ so any small uncertainty on ϵ_M propagates directly to ϵ_T

$$\sigma(\epsilon_M) = \frac{1}{\epsilon_M}\,\sigma(\epsilon_M \epsilon_T) \ \oplus \ \frac{\epsilon_T}{\epsilon_M^2}\,\sigma(\epsilon_M) \tag{A.11}$$

However, the matching efficiency cannot be above 100%, so any measurement of the efficiency giving a confidence interval $\epsilon_M \epsilon_T \in [\epsilon_{low}, \epsilon_{high}]$ can be translated conservatively in

a larger confidence interval for ϵ_T, $\epsilon_T \in [\epsilon_{low}, 100\%]$. This is usually enough, as the ϵ_T is expected to be anyway very close to 100%. Also, the matching efficiency cancels out at least partially when computing the ratio of the tracking efficiencies between data and simulations.

As explained above, the measured tracking efficiency is overestimated because a probe can be matched also to another track in the event, as the matching criteria is very loose. The probability of spurious matches can be measured directly on data in a simple way: before the matching between probes and tracker tracks, one can remove those tracks that combined with the tag give an invariant mass near the J/Ψ peak. The "tracking efficiency" measured with under this circumstances is an estimate of the probability of fake rate. For

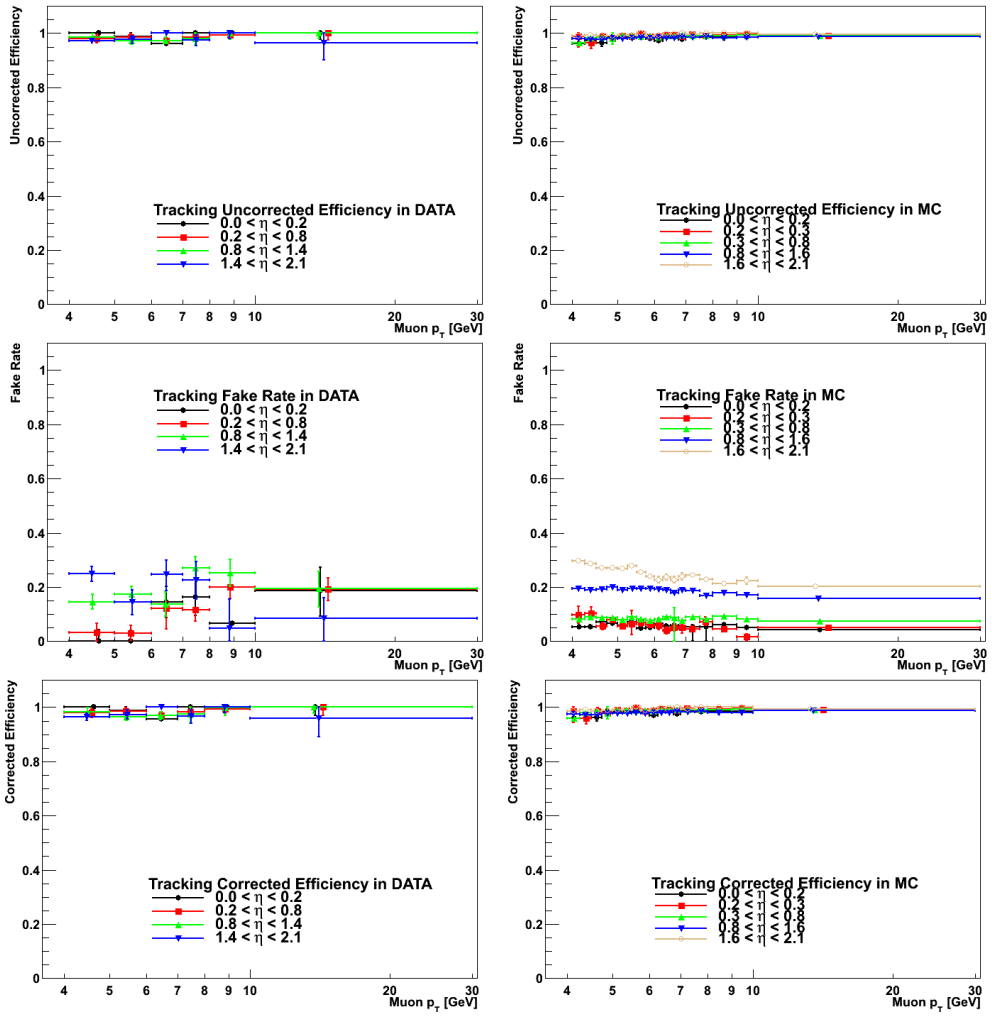

Figure A.1: Results of the T&P fit for the tracking efficiency in data (left) and simulation (right). Top: uncorrected efficiencies. Middle: fake rate. Right: corrected efficiencies.

this measurement a mass window [2.85, 3.25] GeV was used, which contains $\sim$ 99.5% of

the J/Ψ events[2]. One can compute a conservative estimate by removing only the track that gives the best mass value (which might not be the muon track).

From physics reasoning and simulation studies, the tracking efficiency for muons is not expected to depend on p_T in the energy range relevant for this measurement [156]. The uncorrected results of the T&P fit are shown in the left part of Fig. A.1 as a function of the probe η and p_T; in data, the number of probe muons from J/Ψ after background subtraction in the different $|\eta|$ bins is between 100 (in the barrel for high p_T muons) and 1800 (in the endcap for low p_T muons).
The same figure contains the measured fake rate using the definition above. An increase of the fake match probability with $|\eta|$ is expected, as it's related to the increase in the rate of hadrons above the momentum threshold used. The trend is observed in data and is more clearly visible in simulation with finer binning.

The corrected efficiencies are obtained according to equations (A.9), (A.10) using the estimate of the probability of fake matches.
The results are plotted in Fig. A.1. The results are compatible with 98-100% in both data and simulation. In the endcaps, a slightly smaller efficiency is observed in data (although with poor statistical significance given the large error bars), at least part of which could be due to a higher matching inefficiency in data vs simulations.
The tracking efficiency is displayed as a function of p_T and η is reported in Fig. A.2.

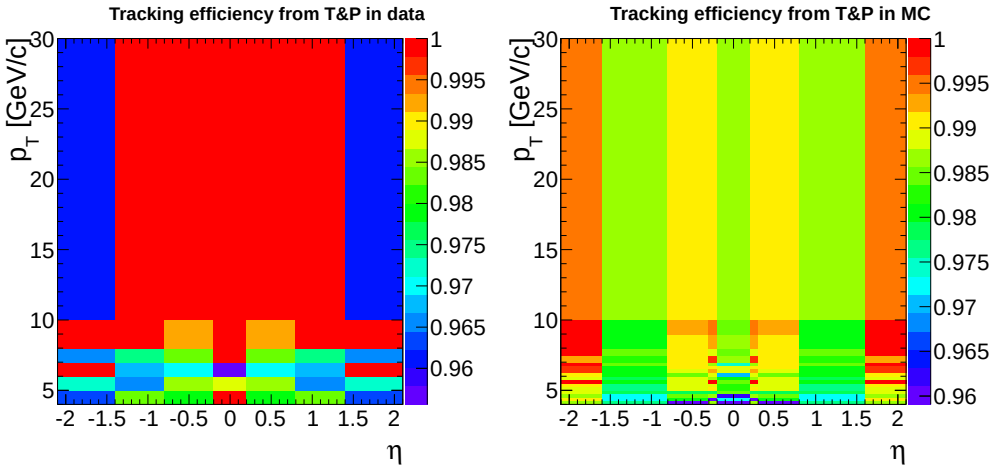

Figure A.2: Corrected tracking efficiencies as a function of η^μ and p_T^μ obtained in the data (left) and simulation (right).

[2]Estimated on simulated J/Ψ's; the di-muon mass resolution in data and simulation agree very well, as described in [69]

A.3.2 Muon identification efficiency

Given the existence of a tracker track, the combined muon reconstruction and identification efficiencies of the selection algorithm can be measured. The complete list of requirements for the muon selection is reported in Section 5.2. It involves both the inner and outer muon tracks, thus exploiting different parts of the detector, (the inner tracker and the muon chambers, respectively).

Two different steps are needed compute the overall efficiency of the selection, one for each sub-detector involved. In the first case (inner track) the probe are all the muons associated to L2 trigger muons, which does not require any tracker information. When considering the outer track, instead, the probes are defined as the passing probes of the previous step, associated to the Track leg of a MuX_TrackY trigger path (X=5 GeV, Y=3,5 GeV). The tag muons are defined as before.

The results of the T&P fits are shown in the left part of Fig. A.3 as a function of the probe η and p_T; in data, the number of probe muons from J/Ψ after background subtraction in the different $|\eta|$ bins is between 100 (in the $0.2 < |\eta| < 0.3$ range for low p_T muons, due to the inefficient wheels' overlap region as described in Section 2.3.3) and 1800 in both cases.

It can be noted that the inner track quality requirements have little impact on the efficiency, which is comparable with the simple tracking efficiency discussed in the previous paragraph. The outer muon quality selection has instead a sizeable effect, with low p_T muons having efficiency as low as $\sim 20\%$. The efficiency plateau is reached for muons with $p_T > 6$ GeV. While for the inner tracker efficiency there are no main differences between different rapidity regions, for the muon related part an inefficiency region is clearly visible in the range $0.2 < |\eta| < 0.3$ especially for low p_T muons, due to the CMS wheels overlap.

A discrepancy is observed between data and simulation, with the former being more efficient up to $\sim 40\%$ in the central rapidity region for low p_T muons. Its origin can be explained by considering the propagation of the tracker track to the muon chambers. The inner muon track, reconstructed in the silicon tracker, is propagated to the muon stations, and a search for the nearest muon segment reconstructed in each station is performed. For each segment found, the normalized residuals (pulls) for position and direction are calculated; the pull is defined as the difference between the position (or direction) of the matched segment and the position (or direction) of the extrapolated track, divided by their combined uncertainty. The track and the segment are considered to be matched if the distance between them in local x is less than 3 cm or if the value of the pull for local x is less than 4. The distribution of distance in local x position between the measured muon segment and the inner track extrapolation has been compared between data and simulation, for successful track to-segment matches. The general trend is well reproduced by the Monte Carlo simulation, although the increase of the width seems a bit larger in the simulation. The widths of the pull distributions in the simulation are about 10% larger than in the data, causing therefore a loss of efficiency.

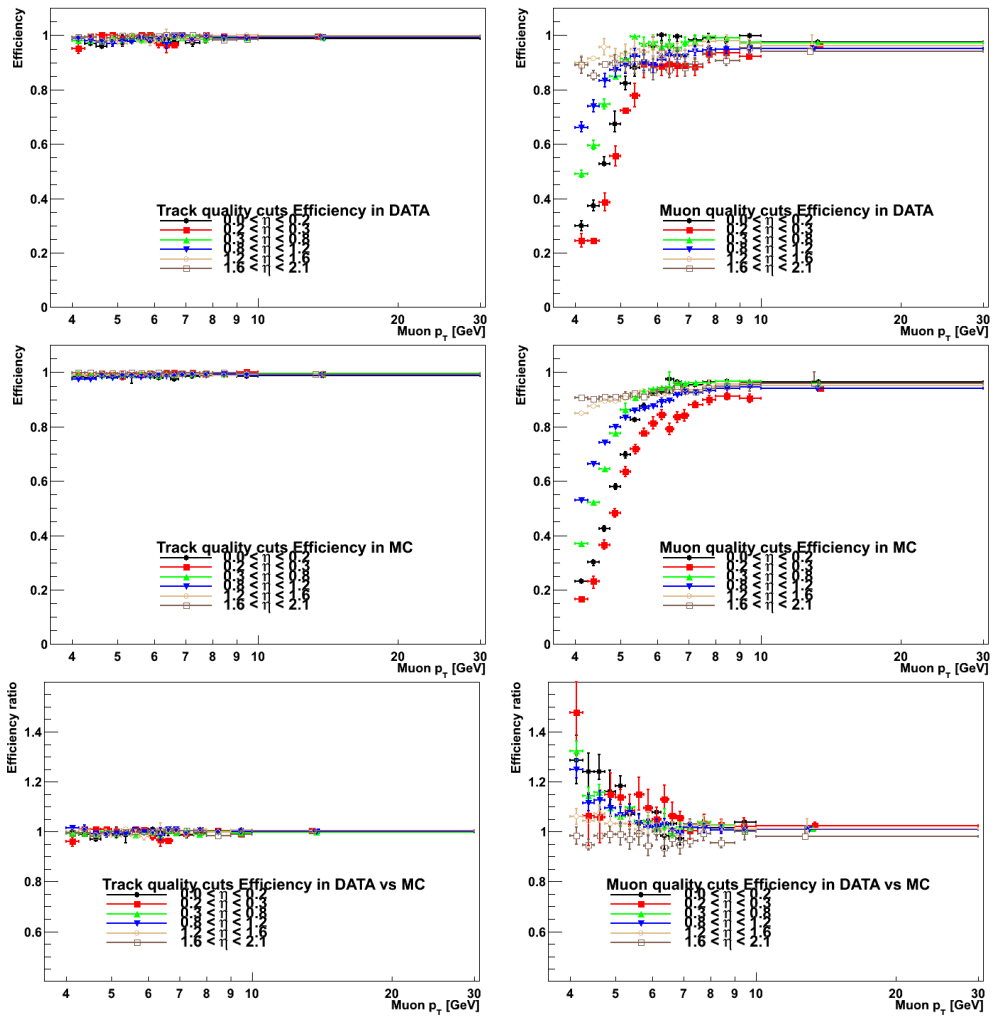

Figure A.3: Results of the T&P fit for the efficiencies of the quality requirements for the muon inner (left) and outer (right) track in data (top) and simulation (middle). The ratio between data and simulation is also shows (bottom).

This difference is reflected in the scaling factor $\epsilon^{\text{data}}_{\text{MuSel}}/\epsilon^{\text{MC}}_{\text{MuSel}} = 1.073 \pm 0.054$ for $p_T > 4$ GeV and 1.041 ± 0.047 for $p_T > 6$ GeV introduced in Section 5.5.
The efficiencies combined for the two steps are furthermore displayed as a function of p_T and η in Fig. A.4.

A.3.3 Trigger efficiency

The CMS trigger system consists of two basic stages, the hardware-based L1 Trigger and the software-based High-Level Trigger (HLT or L3), as described in Section 2.3.5.

In the muon HLT, first a L1 trigger object is used as a seed to reconstruct a standalone-

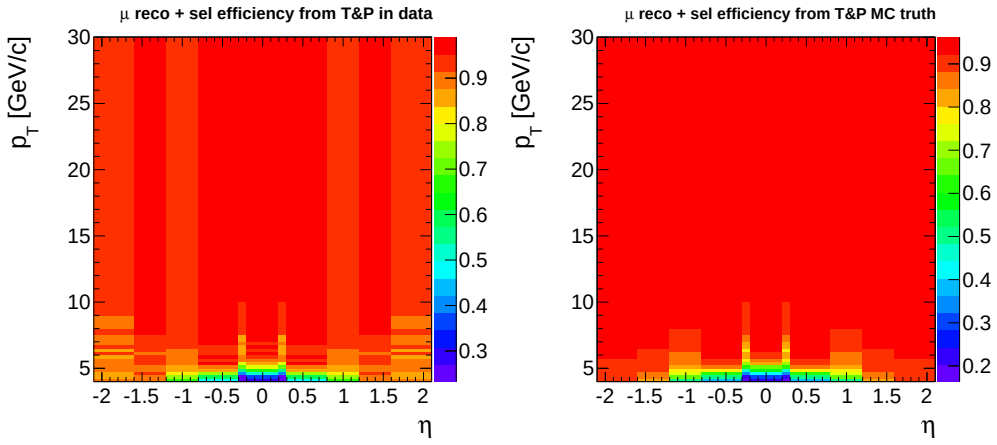

Figure A.4: Efficiencies of the combined muon selection requirements as a function of η^{μ} and p_T^{μ} obtained in the data (left) and simulation (right).

muon track in the muon system, leading to an improved p_T estimate. At this point, p_T threshold filters are applied to the standalone (also called L2) muon. Then seeds in the silicon tracker are generated in the region around the extrapolated L2 muon, and tracker tracks are reconstructed. If a successful match is made between a tracker track and the L2 muon, a global fit combining tracker and muon hits is performed, yielding a L3 muon track on which the final p_T requirements are applied.

The J/$\psi \to \mu^+\mu^-$ events collected by the specialized track-plus-muon triggers were used. Several instances of the muon-plus-track trigger have been deployed, with different thresholds on the p_T of the tracker track.

To evaluate the trigger efficiency, trigger objects must be matched to the muons reconstructed offline. L1 muon trigger candidates are matched to offline muons by position, extrapolating a muon's tracker track to the muon system. HLT muons are matched to the offline-reconstructed muons by direction at the vertex. HLT-only efficiencies are computed matching the probe with the L1 candidate and requiring it to be also matched with the HLT candidate.

The trigger is designed such as in most of the cases L1 and L2 efficiencies can be grouped and evaluated in one step, starting from a muon passing all the quality criteria defined in the analysis. It has been observer that there is a dependence in the L1+L2 efficiency due to the proximity of the muons at the arrival to the first muon station up to ~ 120 cm, as showed in Fig. A.5. However the fraction of selected di-muons closer than this distance and in the sample selected in the analysis is negligible (mostly due to the invariant mass cut $M > 5$ GeV), as showed in the top part of Fig. A.6. To estimate the contamination in the worst case scenario contamination the relative distance of the selected muons with the closest muon (the latter can be any muon in the collection, not just a selected one) has

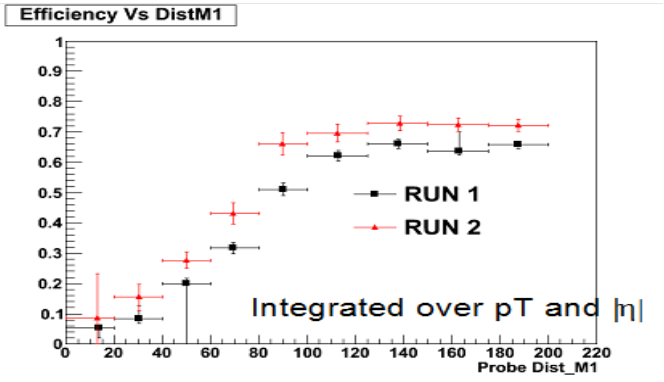

Figure A.5: L1 and L2 trigger efficiency as a function of the di-muon relative distance at Muon Station 1 arrival.

been computed, as reported in the bottom part of Fig. A.6. The amount of dimuons below 120 cm is evaluated to be 0.4% of the total in both data and simulation. For this reason the procedure can be considered safe, and no additional systematic uncertainty is added to the efficiency calculation.
The HLT trigger used in the analysis and called HLT_DoubleMu3_v2 and requires two L3 muons with $p_T > 3$ GeV. The use of T&P method implies that the two legs of the trigger can be factorized as the product of the single muon L3 trigger efficiency.

The results for the L1+L2 (for muons with relative distance > 120 cm at the Muon Station 1 arrival) and L3 trigger efficiency are shown in Fig. A.7 for data and simulation. In data, the number of probe muons from J/Ψ after background subtraction in the different $|\eta|$ bins is between 100 (in the $0.2 < |\eta| < 0.3$ range for low p_T muons, due to the inefficient CMS wheels overlap region as described in Section 2.3.3) and 4500 for the L1+L2 case and 50 to 600 in the L3 evaluation. Also for the trigger an inefficiency region is clearly visible in the range $0.2 < |\eta| < 0.3$ especially for L1+L2 low p_T muons, due to the overlap of the CMS wheels, Out of this region, the L1+L2 trigger efficiencies for low p_T muons are $> 90\%$, while for L3 trigger are $\sim 80\%$. The efficiency plateau is reached for muons with $p_T > 6$ GeV. The trigger efficiencies combined for the two steps are displayed as a function of p_T and η in Fig. A.8.

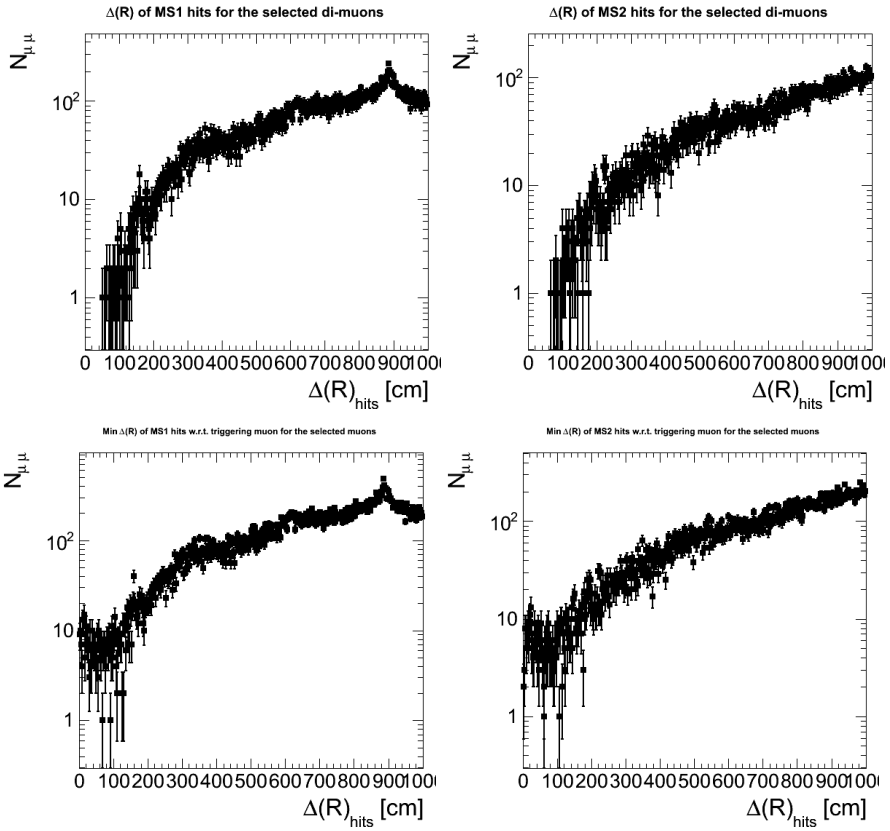

Figure A.6: Top: distribution of relative distance between the selected di-muon at Muon Station 1 (left) and 2 (right) for data. The fraction of di-muons below 120 cm is found to be completely negligible. Bottom: distribution of the closest distance between a selected muon and the closest muon (selected or not) at Muon Station 1 (left) and 2 (right) for data. The fraction of di-muons below 120 cm is found to be 0.4% in all the cases.

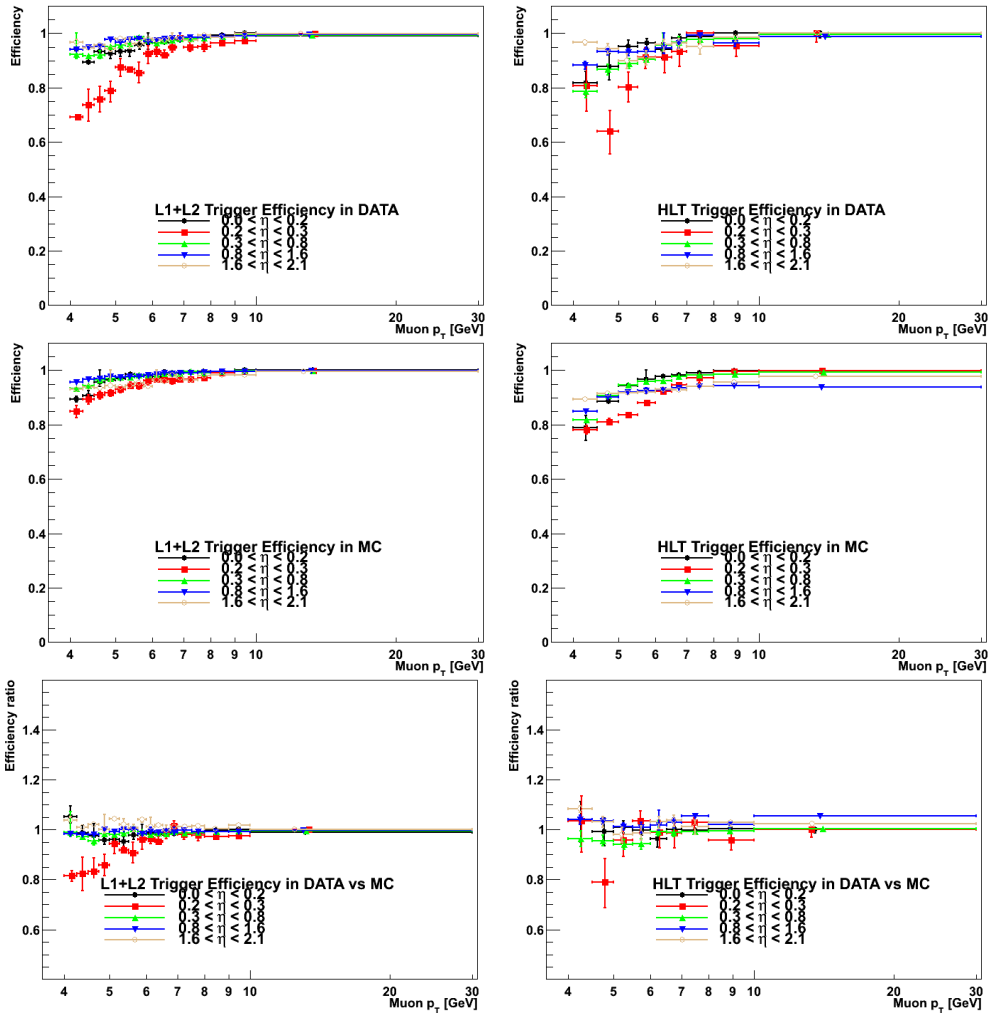

Figure A.7: Results of the T&P fit for the L1+L2 (left, for muons with relative distance > 120 cm at the Muon Station 1 arrival) and L3 trigger (right) efficiencies in data (top) and simulation (middle). The ratio between data and simulation is also shows (bottom).

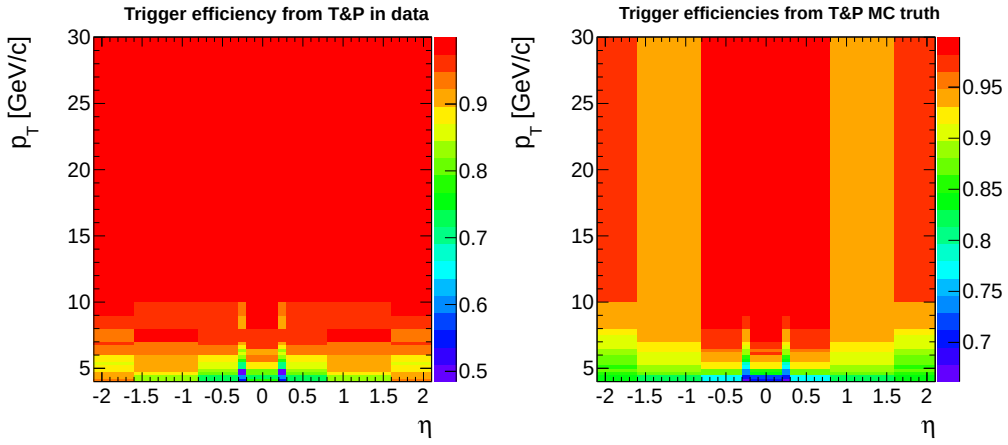

Figure A.8: Efficiencies of the combined trigger selection requirements as a function of η^{μ} and p_T^{μ} obtained in the data (left) and simulation (right).

A.3.4 Tag & Probe scaling factors

Once the T&P efficiencies are computed in data and simulation, one has to rely on MC prediction for the p_T and η distribution of the muons coming from b quarks. The single-particle factorization and T&P themselves do not introduce any sizeable bias, as observed in simulation and reported in the previous section. On the other hand, results in data and simulation can behave differently, due to imperfect description of the experimental apparatus details (especially concerning material budget) and trigger or reconstruction conditions.

Table A.2 shows the scaling factors obtained for muons with $p_T^{\mu} > 4$ GeV using the different single−particle efficiencies discussed above (namely MCTruthBB, $\mathrm{TP_{MCTruth}}$, $\mathrm{TP_{MC}}$, $\mathrm{TP_{Data}}$) when applied to the same signal (p_T, η) distribution. The second column reportas the scaling factor for the events remaining after applying the muon selection, the event selection (di-μ invariant mass cut, only two muons in the event associated the same vertex, ...) and the trigger requirements.

The table shows that $\mathrm{SF}_{MCTruth}$ is different from 1 in both muon selection and trigger steps; in particular the efficiencies obtained with T&P are slightly overestimated (2.6%) in the muon selection step while are underestimated (2%) in the trigger step. One important thing is that SF_{MC} is compatible with $\mathrm{SF}_{MCTruth}$, meaning that there is no bias at reconstruction level. As we said, SF_{Data} can be in principle different from SF_{MC} due to the different conditions in MC and Data but this does not represent a major issue.

Table A.2 shows also the scaling factors obtained for muons with $p_T^{\mu} > 6$ GeV. In this case they are closer to 1, as data and simulation tend to be in better agreement at higher p_T.

	Generated events	$MuSel$	$EvSel$	Trg
$p_T^\mu > 4$ GeV				
$SF_{MCTruthBB}$	-	$0.997^{+0.022}_{-0.035}$	-	$1.019^{+0.012}_{-0.027}$
$SF_{TP-MCTruth}$	-	$1.023^{+0.013}_{-0.014}$	-	$0.977^{+0.005}_{-0.006}$
SF_{TP-MC}	-	$1.032^{+0.017}_{-0.015}$	-	$0.979^{+0.010}_{-0.008}$
$SF_{TP-Data}$	-	$1.101^{+0.056}_{-0.075}$	-	$0.982^{+0.025}_{-0.028}$
$p_T^\mu > 6$ GeV				
$SF_{MCTruthBB}$	-	$1.020^{+0.027}_{-0.064}$	-	$1.000^{+0.017}_{-0.046}$
$SF_{TP-MCTruth}$	-	$1.017^{+0.010}_{-0.010}$	-	$0.987^{+0.004}_{-0.005}$
SF_{TP-MC}	-	$1.029^{+0.013}_{-0.018}$	-	$0.992^{+0.008}_{-0.006}$
$SF_{TP-Data}$	-	$1.041^{+0.036}_{-0.047}$	-	$1.006^{+0.022}_{-0.023}$

Table A.2: Number of events contained in the generated MC sample and in each of the selection steps together with the respective scaling factors obtained using the single-particle MCTruthBB efficiencies muons with $p_T^\mu > 4$ GeV and $p_T^\mu > 6$ GeV.

Appendix B

Generated (p_T, η) distributions in PYTHIA and MC@NLO

In principle, the Monte Carlo MC@NLO could be used to provide an alternative parametrization of the kinematical properties of the signal events with respect to PYTHIA. A comparison of the generated p_T and η distribution between two different PYTHIA tunes (Z2, D6T) and MC@NLO shows an harder p_T spectrum and a strange behavior of the MC@NLO η distribution for the leading p_T muons, as showed in Figs. B.1, B.2 (left column contain the distribution with different MC, the right column the ratio between PYTHIA Z2 and MC@NLO).

The strange behavior of the MC@NLO η distribution for the leading p_T has been studied as a function of the muon p_T and found to be more pronounced at higher p_T, as can be seen in Fig. B.3. Regular behavior is observed for the second leading p_T muons.

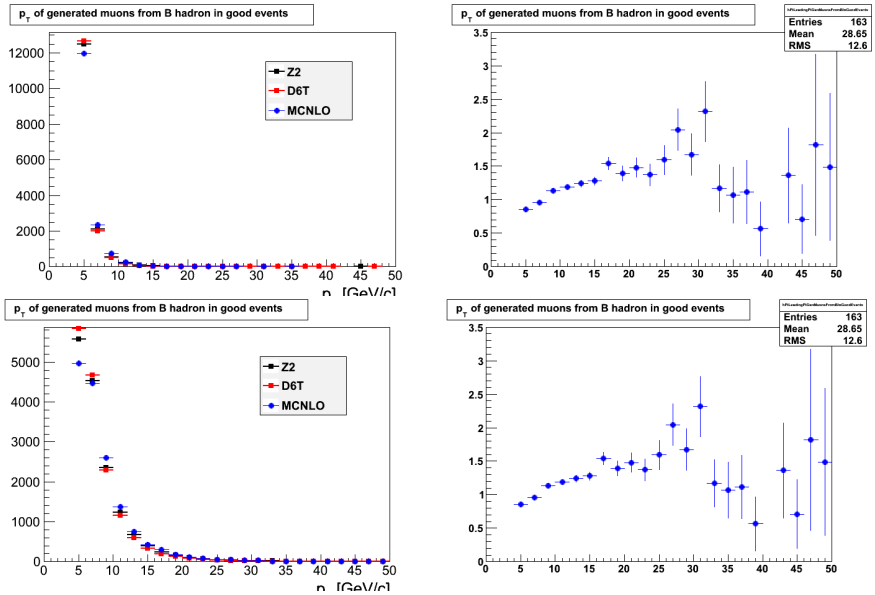

Figure B.1: Generated (p_T, η) distribution of signal muons divided by leading p_T and second leading p_T inside the same event. Left column contain the distribution for PYTHIA and MC@NLO, the right column the ratio between PYTHIA Z2 and MC@NLO. First row: p_T of the leading p_T muons. Second row: p_T of the second leading p_T muons.

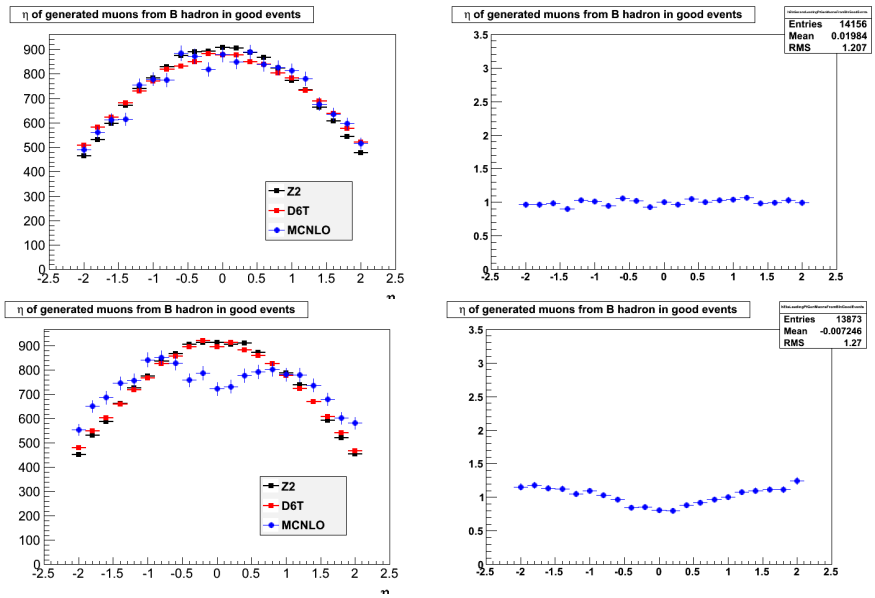

Figure B.2: Generated (p_T, η) distribution of signal muons divided by leading p_T and second leading p_T inside the same event. Left column contain the distribution for PYTHIA and MC@NLO, the right column the ratio between PYTHIA Z2 and MC@NLO. Third row: η of the leading p_T muons. Second row: η of the second leading p_T muons.

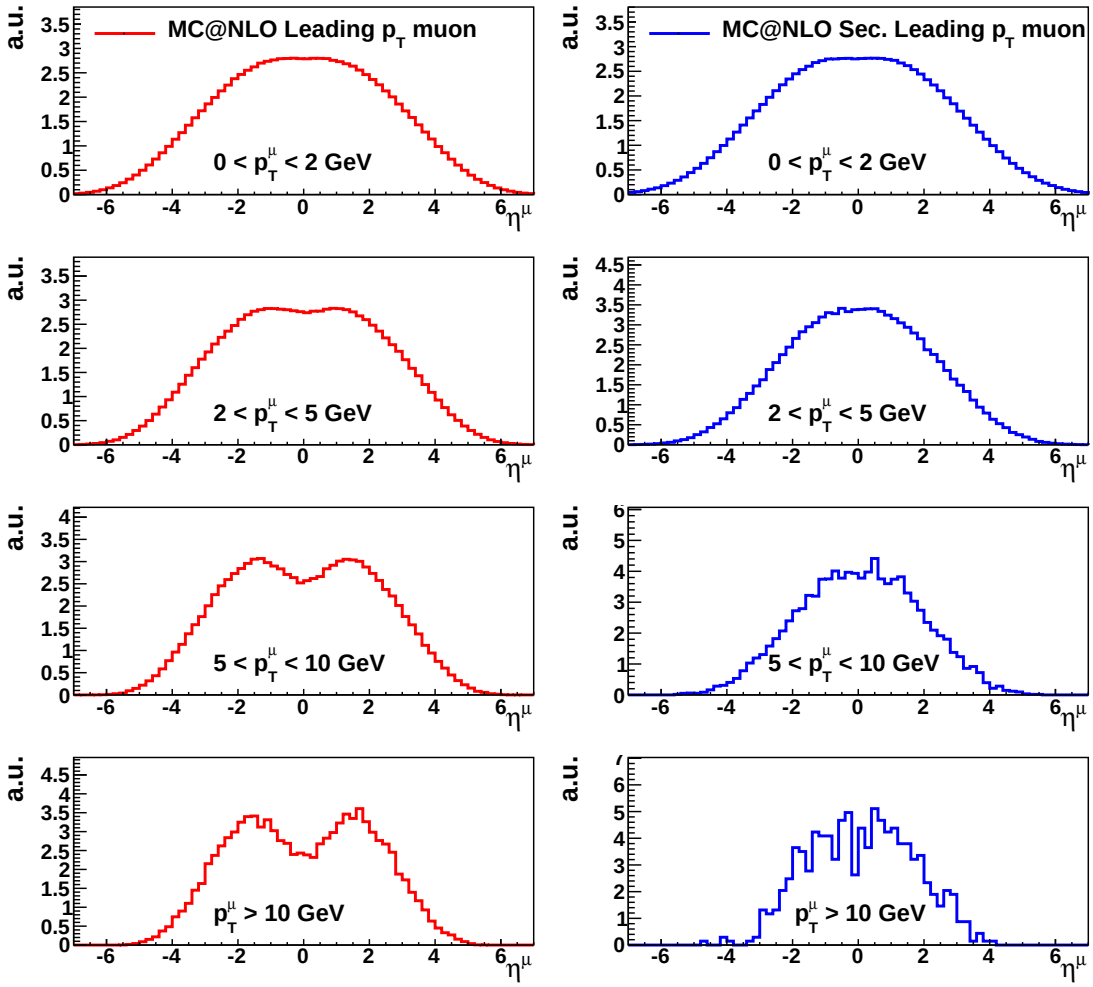

Figure B.3: Generated η distribution of leading (left) and second leading p_T (right) muons in signal events in MC@NLO as a function of increasing p_T (from top to bottom).

Bibliography

[1] M. L. Mangano, *"The saga of bottom production in $p\bar{p}$ collisions"*, *AIP Conf. Proc.* **753** (2005) 247–260. [doi:10.1063/1.1896706].

[2] A. Carlson, J. Hooper, and D. King, *"LXIII. Nuclear transmutations produced by cosmic-ray particles of great energy.Part V. The neutral mesons"*, *Philosophical Magazine Series 7* **41** (1950), no. 318 701–724. [http://www.tandfonline.com/doi/abs/10.1080/14786445008561001].

[3] JADE Collaboration, *"Upper limit on beauty lifetime and lower limit on weak mixing angles"*, *Physics Letters B* **114** (1982), no. 1 71–75. [doi:10.1016/0370-2693(82)90018-1].

[4] MAC Collaboration, *"Lifetime of Particles Containing b Quarks"*, *Phys. Rev. Lett.* **51** (Sep, 1983) 1022–1025. [doi:10.1103/PhysRevLett.51.1022].

[5] ALEPH Collaboration, *"The lifetimes of B states in Z decays"*, *Nuclear Physics B - Proceedings Supplements* **27** (1992), no. 0 152 – 157. [doi:10.1016/0920-5632(92)90045-T].

[6] H1 Collaboration, *"Measurement of beauty production at HERA using events with muons and jets"*, *The European Physical Journal C - Particles and Fields* **41** (2005) 453–467. [doi:10.1140/epjc/s2005-02267-0].

[7] CDF Collaboration, *"Measurement of $b\bar{b}$ production correlations, $B^0\overline{B}^0$ mixing, and a limit on ϵ_B in $p\overline{p}$ collisions at $\sqrt{s} = 1.8$ TeV"*, *Phys. Rev. D* **55** (Mar, 1997) 2546–2558. [doi:10.1103/PhysRevD.55.2546].

[8] S. L. Glashow, *"Partial-symmetries of weak interactions"*, *Nuclear Physics* **22** (1961), no. 4 579–588. [doi:10.1016/0029-5582(61)90469-2].

[9] A. Salam and J. Ward, *"Electromagnetic and weak interactions"*, *Physics Letters* **13** (1964), no. 2 168–171. [doi:10.1016/0031-9163(64)90711-5].

[10] S. Weinberg, *"A Model of Leptons"*, *Phys. Rev. Lett.* **19** (Nov, 1967) 1264–1266. [doi:10.1103/PhysRevLett.19.1264].

[11] S. Weinberg, *"Effects of a neutral intermediate boson in semileptonic processes"*, *Phys. Rev.* **D5** (1972) 1412–1417. [doi:10.1103/PhysRevD.5.1412].

[12] D. J. Gross and F. Wilczek, *"Asymptotically Free Gauge Theories. 1"*, *Phys. Rev.* **D8** (1973) 3633–3652. [doi:10.1103/PhysRevD.8.3633].

[13] D. J. Gross and F. Wilczek, *"Asymptotically Free Gauge Theories. 2"*, *Phys. Rev.* **D9** (1974) 980–993. [doi:10.1103/PhysRevD.9.980].

[14] H. D. Politzer, *"Asymptotic freedom: An approach to strong interactions"*, *Physics Reports* **14** (1974), no. 4 129–180. [doi:10.1016/0370-1573(74)90014-3].

[15] M. Peskin and D. Schroeder, *"Introduction to quantum field theory"*. Advanced Book Program. Addison-Wesley Pub. Co., 1995.

[16] C. N. Yang and R. L. Mills, *"Conservation of Isotopic Spin and Isotopic Gauge Invariance"*, *Phys. Rev.* **96** (Oct, 1954) 191–195. [doi:10.1103/PhysRev.96.191].

[17] UA1 Collaboration, G. A. et al., *"Experimental observation of isolated large transverse energy electrons with associated missing energy at s=540 GeV"*, *Physics Letters B* **122** (1983), no. 1 103–116. [doi:10.1016/0370-2693(83)91177-2].

[18] UA1 Collaboration, G. A. et al., *"Experimental observation of lepton pairs of invariant mass around 95 GeV/c2 at the CERN SPS collider"*, *Physics Letters B* **126** (1983), no. 5 398–410. [doi:10.1016/0370-2693(83)90188-0].

[19] UA2 Collaboration, M. B. et al., *"Observation of single isolated electrons of high transverse momentum in events with missing transverse energy at the CERN pp collider"*, *Physics Letters B* **122** (1983), no. 5-6 476–485. [doi:10.1016/0370-2693(83)91605-2].

[20] UA2 Collaboration, P. B. et al., *"Evidence for $Z^0 \to e^+e^-$ at the CERN pp collider"*, *Physics Letters B* **129** (1983), no. 1-2 130–140. [doi:10.1016/0370-2693(83)90744-X].

[21] S. L. Glashow, J. Iliopoulos, and L. Maiani, *"Weak Interactions with Lepton-Hadron Symmetry"*, *Phys. Rev. D* **2** (Oct, 1970) 1285–1292. [doi:10.1103/PhysRevD.2.1285].

[22] CDF Collaboration, *"Observation of Top Quark Production in $\overline{p}p$ Collisions with the Collider Detector at Fermilab"*, *Phys. Rev. Lett.* **74** (Apr, 1995) 2626–2631. [doi:10.1103/PhysRevLett.74.2626].

[23] DØ Collaboration, *"Observation of the Top Quark"*, *Phys. Rev. Lett.* **74** (1995) 2632. [doi:10.1103/PhysRevLett.74.2632].

[24] M. Gell-Mann, *"A schematic model of baryons and mesons"*, *Physics Letters* **8** (1964), no. 3 214–215. [doi:10.1016/S0031-9163(64)92001-3].

[25] T. D. Lee and C. N. Yang, *"Question of Parity Conservation in Weak Interactions"*, *Phys. Rev.* **104** (Oct, 1956) 254–258. [doi:10.1103/PhysRev.104.254].

[26] C. S. Wu, E. Ambler, R. W. Hayward, D. D. Hoppes, and R. P. Hudson, *"Experimental Test of Parity Conservation in Beta Decay"*, *Phys. Rev.* **105** (Feb, 1957) 1413–1415. [doi:10.1103/PhysRev.105.1413].

[27] LEP Collaboration, *"LEP Electroweak Working Group"*. [http://lepewwg.web.cern.ch/LEPEWWG/].

[28] Tevatron Collaboration, *"Tevatron Electroweak Working Group"*. [http://tevewwg.fnal.gov/].

[29] P. Higgs, *"Broken symmetries, massless particlees and gauge fields"*, *Physics Letters* **12** (1964), no. 2 132–133. [doi:10.1016/0031-9163(64)91136-9].

[30] P. W. Higgs, *"Broken Symmetries and the Masses of Gauge Bosons"*, *Phys. Rev. Lett.* **13** (Oct, 1964) 508–509. [doi:10.1103/PhysRevLett.13.508].

[31] P. W. Higgs, *"Spontaneous Symmetry Breakdown without Massless Bosons"*, *Phys. Rev.* **145** (May, 1966) 1156–1163. [doi:10.1103/PhysRev.145.1156].

[32] F. Englert and R. Brout, *"Broken Symmetry and the Mass of Gauge Vector Mesons"*, *Phys. Rev. Lett.* **13** (Aug, 1964) 321–323. [doi:10.1103/PhysRevLett.13.321].

[33] L. Alvarez-Gaume and J. Ellis, *"Eyes on a prize particle"*, *Nat. Phys.* **7** (2011), no. 1 2–3. [doi:10.1038/nphys1874].

[34] J. Goldstone, *"Field theories with « Superconductor » solutions"*, *Il Nuovo Cimento (1955-1965)* **19** (1961) 154–164. [doi:10.1007/BF02812722].

[35] Y. Nambu and G. Jona-Lasinio, *"Dynamical Model of Elementary Particles Based on an Analogy with Superconductivity. I"*, *Phys. Rev.* **122** (Apr, 1961) 345–358. [doi:10.1103/PhysRev.122.345].

[36] Y. Nambu and G. Jona-Lasinio, *"Dynamical Model of Elementary Particles Based on an Analogy with Superconductivity. II"*, *Phys. Rev.* **124** (Oct, 1961) 246–254. [doi:10.1103/PhysRev.124.246].

[37] J. Goldstone, A. Salam, and S. Weinberg, *"Broken Symmetries"*, *Phys. Rev.* **127** (Aug, 1962) 965–970. [doi:10.1103/PhysRev.127.965].

[38] N. Cabibbo, *"Unitary Symmetry and Leptonic Decays"*, *Phys. Rev. Lett.* **10** (Jun, 1963) 531–533. [doi:10.1103/PhysRevLett.10.531].

[39] M. Kobayashi and T. Maskawa, *"CP-Violation in the Renormalizable Theory of Weak Interaction"*, *Progress of Theoretical Physics* **49** (1973), no. 2 652–657. [doi:10.1143/PTP.49.652].

[40] C. Giunti, *"Neutrino flavour states and the quantum theory of neutrino oscillations"*, *Journal of Physics G: Nuclear and Particle Physics* **34** (2007), no. 2 R93. [doi:10.1088/0954-3899/34/2/R02].

[41] U. Dore and D. Orestano, *"Experimental results on neutrino oscillations"*, *Reports on Progress in Physics* **71** (2008), no. 10 106201. [doi:10.1088/0034-4885/71/10/106201].

[42] G. Bertone, D. Hooper, and J. Silk, *"Particle dark matter: evidence, candidates and constraints"*, *Physics Reports* **405** (2005), no. 5-6 279–390. [doi:10.1016/j.physrep.2004.08.031].

[43] Abdelhak and Djouadi, *"The anatomy of electroweak symmetry breaking Tome II: The Higgs bosons in the Minimal Supersymmetric Model"*, *Physics Reports* **459** (2008), no. 1-6 1–241. [doi:10.1016/j.physrep.2007.10.005].

[44] E. . Bruning *et al.*, *"LHC design report. Vol. I: The LHC main ring"*. CERN-2004-003-V-1, [http://lhc.web.cern.ch/lhc/LHC-DesignReport.html].

[45] ATLAS Collaboration, *"The ATLAS Experiment at the CERN Large Hadron Collider"*, *JINST* **3** (2008) S08003. [doi:10.1088/1748-0221/3/08/S08003].

[46] CMS Collaboration, *"The CMS Experiment at the CERN LHC"*, *JINST* **3** (2008) S08004. [doi:10.1088/1748-0221/3/08/S08004].

[47] LHCb Collaboration, *"The LHCb Detector at the CERN LHC"*, *JINST* **3** (2008) S08005. [doi:10.1088/1748-0221/3/08/S08005].

[48] ALICE Collaboration, *"The ALICE Experiment at the CERN LHC"*, *JINST* **3** (2008) S08002. [doi:10.1088/1748-0221/3/08/S08002].

[49] CMS Collaboration, *"CMS Luminosity - Public Results"*. [https://twiki.cern.ch/twiki/bin/view/CMSPublic/LumiPublicResults].

[50] CMS Collaboration, *"CMS Physics Technical Design Report Volume I: Detector Performance and Software"*. Technical Design Report CMS Series. CERN, Geneva, CMS-TDR-008-1, 2006. [https://cdsweb.cern.ch/record/922757].

[51] CMS Collaboration, *"CMS physics Technical Design Report, Volume II: Physics Performance"*, vol. 34. 2007. [doi:10.1088/0954-3899/34/6/S01].

[52] CMS Collaboration, *"The CMS Magnet Project: Technical Design Report"*. Technical Design Report CMS Series. CERN, CMS-TDR-001, 1997. [https://cdsweb.cern.ch/record/331056].

[53] CERN, *"Document Server Photo Archive"*. [http://cdsweb.cern.ch/collection/Photos].

[54] CMS Collaboration, *"The CMS Tracker Project: Technical Design Report"*. Technical Design Report CMS Series. CERN, CMS-TDR-005, 1998. [https://cdsweb.cern.ch/record/368412].

[55] CMS Collaboration, *"Addendum to the CMS Tracker Technical Design Report"*. Technical Design Report CMS Series. CERN, CMS-TDR-005 Addendum 1, 2000. [https://cdsweb.cern.ch/record/490194].

[56] W. A. et al., *"Track reconstruction in the CMS tracker"*. CMS NOTE-2006/041, [https://cdsweb.cern.ch/record/934067].

[57] Pierre and Billoir, *"Progressive track recognition with a Kalman-like fitting procedure"*, *Computer Physics Communications* **57** (1989), no. 1-3 390–394. [doi:10.1016/0010-4655(89)90249-X].

[58] T. Speer, K. Prokofiev, R. Fruhwirth, W. Waltenberger, and R. Vanlear, *"Vertex Fitting in the CMS Tracker"*. CMS NOTE-2006/032, [https://cdsweb.cern.ch/record/927395].

[59] CMS Collaboration, *"The CMS Muon Project: Technical Design Report"*. Technical Design Report CMS Series. CERN, CMS-TDR-003, 1997. [https://cdsweb.cern.ch/record/343814].

[60] CMS Collaboration, *"The CMS Electromagnetic Calorimeter Project: Technical Design Report"*. Technical Design Report CMS Series. CERN, CMS-TDR-004, 1997. [https://cdsweb.cern.ch/record/349375].

[61] CMS Collaboration, *"The CMS Hadron Calorimeter Project: Technical Design Report"*. Technical Design Report CMS Series. CERN, CMS-TDR-002, 1997. [https://cdsweb.cern.ch/record/357153].

[62] CMS Collaboration, *"The CMS TriDAS Project: Technical Design Report, Volume 1 – The Trigger System"*. Technical Design Report CMS Series. CERN, CMS-TDR-006-1, 2000. [https://cdsweb.cern.ch/record/706847].

[63] CMS Collaboration, *"The CMS TriDAS Project: Technical Design Report, Volume 2 – Data Acquisition and High Level Trigger"*. Technical Design Report CMS Series. CERN, CMS-TDR-006-2, 2002. [https://cdsweb.cern.ch/record/578006].

[64] CMS Collaboration, *"Commissioning of the CMS experiment and the cosmic run at four tesla"*, *Journal of Instrumentation* **5** (2010), no. 03 T03001. [doi:10.1088/1748-0221/5/03/T03001].

[65] CMS Collaboration, *"CMS tracking performance results from early LHC operation"*, *The European Physical Journal C - Particles and Fields* **70** (2010) 1165–1192. [doi:10.1140/epjc/s10052-010-1491-3].

[66] CMS Collaboration, *"Tracking and Primary Vertex Results in First 7 TeV Collisions"*. CMS PAS TRK-10-005, [https://cdsweb.cern.ch/record/1279383].

[67] CMS Collaboration, *"Measurement of Tracking Efficiency"*. CMS PAS TRK-10-002, [https://cdsweb.cern.ch/record/1279139].

[68] CMS Collaboration, *"Performance of muon identification in pp collisions at $\sqrt{s}$=7 TeV"*. CMS PAS MUO-10-002, [https://cdsweb.cern.ch/record/1279140].

[69] CMS Collaboration, *"Measurement of Momentum Scale and Resolution using Low-mass Resonances and Cosmic Ray Muons"*. CMS PAS TRK-10-004, [https://cdsweb.cern.ch/record/1279137].

[70] CMS Collaboration, *"Electromagnetic calorimeter commissioning and first results with 7 TeV data"*. CMS PAS EGM-10-002, [http://cms-physics.web.cern.ch/cms-physics/public/EGM-10-002-pas.pdf].

[71] CMS Collaboration, *"Electromagnetic calorimeter calibration with 7 TeV data"*. CMS PAS EGM-10-003, [https://cdsweb.cern.ch/record/1279350].

[72] M. Cacciari, G. P. Salam, and G. Soyez, *"The anti-k_t jet clustering algorithm"*, *Journal of High Energy Physics* **2008** (2008), no. 04 063. [doi:10.1088/1126-6708/2008/04/063].

[73] CMS Collaboration, *"Commissioning of the Particle-Flow reconstruction in Minimum-Bias and Jet Events from pp Collisions at 7 TeV"*. CMS PAS PFT-10-002, [https://cdsweb.cern.ch/record/1279341].

[74] CMS Collaboration, *"Jet Performance in pp Collisions at $\sqrt{s} = 7$ TeV"*. CMS PAS JME-10-003, [https://cdsweb.cern.ch/record/1279362].

[75] CMS Collaboration, *"Jet Energy Corrections determination in pp Collisions at $\sqrt{s} = 7$ TeV"*. CMS PAS JME-10-010, [https://cdsweb.cern.ch/record/1308178].

[76] CMS Collaboration, *"Jet Energy Resolution in CMS at $\sqrt{s} = 7$ TeV"*. CMS PAS JME-10-014, [https://cdsweb.cern.ch/record/1339945].

[77] CMS Collaboration, *"First Measurement of Bose-Einstein Correlations in Proton-Proton Collisions at $\sqrt{s} = 0.9$ and 2.36 TeV at the LHC"*, *Phys. Rev. Lett.* **105** (Jul, 2010) 032001. [doi:10.1103/PhysRevLett.105.032001].

[78] CMS Collaboration, *"Measurement of Bose-Einstein correlations in pp collisions at "$\sqrt{s} = 0.9$" and 7 TeV"*, *Journal of High Energy Physics* **2011** (2011) 1–29. [doi:10.1007/JHEP05(2011)029].

[79] M. Gyulassy, S. K. Kauffmann, and L. W. Wilson, *"Pion interferometry of nuclear collisions. I. Theory"*, *Phys. Rev. C* **20** (Dec, 1979) 2267–2292. [doi:10.1103/PhysRevC.20.2267].

[80] E735 Collaboration, *"Study of source size in $p\overline{p}$ collisions at $\sqrt{s} = 1.8$ TeV using pion interferometry"*, *Phys. Rev. D* **48** (Sep, 1993) 1931–1942. [doi:10.1103/PhysRevD.48.1931].

[81] ALICE Collaboration, *"Two-pion Bose-Einstein correlations in pp collisions at $\sqrt{s} = 900$ GeV"*, *Phys. Rev. D* **82** (Sep, 2010) 052001. [doi:10.1103/PhysRevD.82.052001].

[82] T. Cs

[83] L3 Collaboration, *"Test of the τ-model of BoseEinstein correlations and reconstruction of the source function in hadronic Z-boson decay at LEP"*, *The European Physical Journal C - Particles and Fields* **71** (2011) 1–25. [doi:10.1140/epjc/s10052-011-1648-8].

[84] S. Bethke, *"The 2009 world average of α_s"*, *The European Physical Journal C - Particles and Fields* **64** (2009) 689–703. [doi:10.1140/epjc/s10052-009-1173-1].

[85] D. Duke and R. Roberts, *"Determinations of the QCD strong coupling α_s and the scale Λ_{QCD}"*, *Physics Reports* **120** (1985), no. 5-6 275–368. [doi:10.1016/0370-1573(85)90112-7].

[86] R. Ellis, H. Georgi, M. Machacek, H. Politzer, and G. G. Ross, *"Perturbation theory and the parton model in QCD"*, *Nuclear Physics B* **152** (1979), no. 2 285–329. [doi:10.1016/0550-3213(79)90105-6].

[87] J. C. Collins, D. E. Soper, and G. F. Sterman, *"Factorization of Hard Processes in QCD"*, *Adv. Ser. Direct. High Energy Phys.* **5** (1988) 1–91, [hep-ph/0409313].

[88] J. C. Collins and D. E. Soper, *"The Theorems of Perturbative QCD"*, *Ann. Rev. Nucl. Part. Sci.* **37** (1987) 383–409. [doi:10.1146/annurev.ns.37.120187.002123].

[89] J. C. Collins, D. E. Soper, and G. Sterman, *"Heavy particle production in high-energy hadron collisions"*, *Nuclear Physics B* **263** (1986), no. 1 37–60. [doi:10.1016/0550-3213(86)90026-X].

[90] V. N. Gribov and L. N. Lipatov, *"e^+e^- pair annihilation and deep inelastic ep scattering in perturbation theory"*, *Sov. J. Nucl. Phys.* **15** (1972) 675–684.

[91] V. N. Gribov and L. N. Lipatov, *"Deep inelastic ep scattering in perturbation theory"*, *Sov. J. Nucl. Phys.* **15** (1972) 438–450.

[92] G. Altarelli and G. Parisi, *"Asymptotic Freedom in Parton Language"*, *Nucl. Phys.* **B126** (1977) 298. [doi:10.1016/0550-3213(77)90384-4].

[93] Y. L. Dokshitzer, *"Calculation of the Structure Functions for Deep Inelastic Scattering and e^+e^- Annihilation by Perturbation Theory in Quantum Chromodynamics"*, *Sov. Phys. JETP* **46** (1977) 641–653.

[94] J. Pumplin *et al.*, *"New generation of parton distributions with uncertainties from global QCD analysis"*, *JHEP* **07** (2002) 012, [hep-ph/0201195].

[95] A. Martin, R. Roberts, W. Stirling, and R. Thorne, *"MRST2001: partons and α_s from precise deep inelastic scattering and Tevatron jet data"*, *The European Physical Journal C - Particles and Fields* **23** (2002) 73–87. [doi:10.1007/s100520100842].

[96] A. D. Martin, W. J. Stirling, R. S. Thorne, and G. Watt, *"Parton distributions for the LHC"*, *Eur. Phys. J.* **C63** (2009) 189–285. [doi:10.1140/epjc/s10052-009-1072-5].

[97] R. D. Ball, L. D. Debbio, S. Forte, A. Guffanti, J. I. Latorre, A. Piccione, J. Rojo, and M. Ubiali, *"A determination of parton distributions with faithful uncertainty estimation"*, *Nuclear Physics B* **809** (2009), no. 1-2 1–63. [doi:10.1016/j.nuclphysb.2008.09.037].

[98] R. D. Ball, L. D. Debbio, S. Forte, A. Guffanti, J. I. Latorre, A. Piccione, J. Rojo, and M. Ubiali, *"Erratum to: "A determination of parton distributions with faithful uncertainty estimation" [Nucl. Phys. B 809 (2009) 1-63]"*, *Nuclear Physics B* **816** (2009), no. 1-2 293. [doi:10.1016/j.nuclphysb.2009.02.027].

[99] HERA collaboration, *"Combined measurement and QCD analysis of the inclusive scattering cross sections at HERA"*, *Journal of High Energy Physics* **2010** (2010) 1–63. [doi:10.1007/JHEP01(2010)109].

[100] M. Glück, J. F. Owens, and E. Reya, *"Gluon contribution to hadronic J/ψ production"*, *Phys. Rev. D* **17** (May, 1978) 2324–2331. [doi:10.1103/PhysRevD.17.2324].

[101] B. Combridge, *"Associated production of heavy flavour states in pp and $p\bar{p}$ interactions: Some QCD estimates"*, *Nuclear Physics B* **151** (1979), no. 0 429–456. [doi:10.1016/0550-3213(79)90449-8].

[102] J. Babcock, D. Sivers, and S. Wolfram, *"Quantum-chromodynamic estimates for heavy-particle production"*, *Phys. Rev. D* **18** (Jul, 1978) 162–181. [doi:10.1103/PhysRevD.18.162].

[103] W. Beenakker, H. Kuijf, W. L. van Neerven, and J. Smith, *"QCD corrections to heavy-quark production in $p\overline{p}$ collisions"*, *Phys. Rev. D* **40** (Jul, 1989) 54–82. [doi:10.1103/PhysRevD.40.54].

[104] W. Beenakker, W. van Neerven, R. Meng, G. Schuler, and J. Smith, *"QCD corrections to heavy quark production in hadron hadron collisions"*, *Nucl. Phys.* **B351** (1991) 507. [doi:10.1016/S0550-3213(05)80032-X].

[105] R. M. Ralich, *"Study of b Quark Pair Production Mechanisms in pp Collisions with the CMS Experiment at LHC"*. PhD thesis, Florida Institute of Technology, 2009. [https://cdsweb.cern.ch/record/1311216/].

[106] P. Nason and C. Oleari, *"A phenomenological study of heavy-quark fragmentation functions in e^+e^- annihilation"*, *Nuclear Physics B* **565** (2000), no. 1-2 245–266. [doi:10.1016/S0550-3213(99)00673-2].

[107] C. Peterson, D. Schlatter, I. Schmitt, and P. M. Zerwas, *"Scaling violations in inclusive e^+e^- annihilation spectra"*, *Phys. Rev. D* **27** (Jan, 1983) 105–111. [doi:10.1103/PhysRevD.27.105].

[108] P. D. B. Collins and T. P. Spiller, *"The fragmentation of heavy quarks"*, *Journal of Physics G: Nuclear Physics* **11** (1985), no. 12 1289. [doi:10.1088/0305-4616/11/12/006].

[109] V. Kartvelishvili, A. Likhoded, and V. Petrov, *"On the fragmentation functions of heavy quarks into hadrons"*, *Physics Letters B* **78** (1978), no. 5 615–617. [doi:10.1016/0370-2693(78)90653-6].

[110] B. Andersson, G. Gustafson, and B. Söderberg, *"A general model for jet fragmentation"*, *Zeitschrift für Physik C Particles and Fields* **20** (1983) 317–329. [doi:10.1007/BF01407824].

[111] OPAL collaboration, *"A study of b quark fragmentation into B^0 and B^+ mesons at LEP"*, *Physics Letters B* **364** (1995), no. 2 93–106. [doi:10.1016/0370-2693(95)01293-7].

[112] Particle Data Group, *"Review of Particle Physics"*, *J. Phys. G* **37** (2010) 075021. [doi:10.1088/0954-3899/37/7A/075021].

[113] L. Ristori and G. Punzi, *"Triggering on Heavy Flavors at Hadron Colliders"*, *Annual Review of Nuclear and Particle Science* **60** (2010), no. 1 595–614. [doi:10.1146/annurev.nucl.012809.104501].

[114] Heavy Flavour Averaging Group (HFAG), *"Averages of b-hadron, c-hadron, and tau-lepton Properties"*, arXiv:1010.1589.

[115] T. Sjöstrand, S. Mrenna, and P. Skands, *"PYTHIA 6.4 physics and manual"*, *Journal of High Energy Physics* **2006** (2006), no. 05 026. [doi:10.1088/1126-6708/2006/05/026].

[116] S. Frixione and B. R. Webber, *"Matching NLO QCD computations and parton shower simulations"*, *Journal of High Energy Physics* **2002** (2002), no. 06 029. [doi:1126-6708/2002/i=06/a=029].

[117] J. Pumplin et al., *"New Generation of Parton Distributions with Uncertainties from Global QCD Analysis"*, *JHEP* **07** (2002) 012. [doi:10.1088/1126-6708/2002/07/012].

[118] R. Field, *"Early LHC Underlying Event Data - Findings and Surprises"*, arXiv:1010.3558.

[119] G. e. a. Corcella, *"HERWIG 6: an event generator for hadron emission reactions with interfering gluons (including supersymmetric processes)"*, *Journal of High Energy Physics* **2001** (2001), no. 01 010. [doi:1126-6708/2001/i=01/a=010].

[120] S. Frixione and M. L. Mangano, *"Heavy quark jets in hadronic collisions"*, *Nucl. Phys.* **B483** (1997) 321. [doi:10.1016/S0550-3213(96)00577-9].

[121] J. Campbell and R. K. Ellis, *"Radiative corrections to* $\mathrm{Zb\bar{b}}$ *production"*, *Phys. Rev. D* **62** (Oct, 2000) 114012. [doi:10.1103/PhysRevD.62.114012].

[122] A. Banfi, G. P. Salam, and G. Zanderighi, *"Accurate QCD predictions for heavy-quark jets at the Tevatron and LHC"*, *Journal of High Energy Physics* **2007** (2007), no. 07 026. [doi:10.1088/1126-6708/2007/07/026].

[123] P. Nason, S. Dawson, and R. Ellis, *"The Total Cross-Section for the Production of Heavy Quarks in Hadronic Collisions"*, *Nucl. Phys.* **B303** (1988) 607. [doi:10.1016/0550-3213(88)90422-1].

[124] J. C. Collins and R. Ellis, *"Heavy quark production in very high-energy hadron collisions"*, *Nucl. Phys.* **B360** (1991) 3. [doi:10.1016/0550-3213(91)90288-9].

[125] P. Nason, S. Dawson, and R. Ellis, *"The One Particle Inclusive Differential Cross-Section for Heavy Quark Production in Hadronic Collisions"*, *Nucl. Phys.* **B327** (1989) 49. [doi:10.1016/0550-3213(89)90286-1].

[126] P. and Nason, *"Heavy quark production"*, *Nuclear Physics B - Proceedings Supplements* **7** (1989), no. 2 46–59. [doi:10.1016/0920-5632(89)90585-9].

[127] S. Frixione, M. L. Mangano, P. Nason, and G. Ridolfi, *"Heavy quark production"*, *Adv. Ser. Direct. High Energy Phys.* **15** (1998) 609–706, [hep-ph/9702287].

[128] S. Catani, M. Ciafaloni, and F. Hautmann, *"High-energy factorization and small-x heavy flavor production"*, *Nucl. Phys.* **B366** (1991) 135. [doi:10.1016/0550-3213(91)90055-3].

[129] M. Cacciari and M. Greco, *"Large p_T hadroproduction of heavy quarks"*, *Nucl. Phys.* **B421** (1994) 530. [doi:10.1016/0550-3213(94)90515-0].

[130] DØ collaboration, B. Abbott *et al.*, *"The $b\bar{b}$ production cross section and angular correlations in $p\bar{p}$ collisions at $\sqrt{s} = 1.8$ Tev"*, *Phys. Lett.* **B487** (2000) 264. [doi:10.1016/S0370-2693(00)00844-3].

[131] CDF Collaboration, *"Measurement of correlated $b\bar{b}$ production in $p\bar{p}$ collisions at $\sqrt{s}$ =1960 GeV"*, *Phys. Rev. D* **77** (Apr, 2008) 072004. [doi:10.1103/PhysRevD.77.072004].

[132] CMS Collaboration, *"Inclusive b-hadron production cross section with muons in pp collisions at $\sqrt{s}$ =7 TeV"*, *JHEP* **03** (2011) 090. [doi:10.1007/JHEP03(2011)090].

[133] CMS Collaboration, *"Inclusive b-jet production in pp collisions at $\sqrt{s}$ =7 TeV"*. CMS PAS BPH-10-009, [https://cdsweb.cern.ch/record/1280454].

[134] G. e. a. Aad, *"Measurement of the inclusive and dijet cross-sections of b-jets in pp collisions at $\sqrt{s} = 7$ TeV with the ATLAS detector"*, *The European Physical Journal C - Particles and Fields* **71** (2011) 1–22. [doi:10.1140/epjc/s10052-011-1846-4].

[135] LHCb Collaboration, *"Measurement of $\sigma_{pp\to b\bar{b}X}$ at $\sqrt{s}$ =7 TeV in the forward region"*, *Phys. Lett. B* **694** (2010), no. 3 209 – 216. [doi:10.1016/j.physletb.2010.10.010].

[136] CMS Collaboration, *"Measurement of $B\overline{B}$ angular correlations based on secondary vertex reconstruction at $\sqrt{s} = 7$ TeV"*, *Journal of High Energy Physics* **2011** (2011) 1–35. [doi:10.1007/JHEP03(2011)136].

[137] CMS Collaboration, *Measurement of the B^+ Production Cross Section in pp Collisions at $\sqrt{s} = 7$* TeV, *Phys. Rev. Lett.* **106** (Mar, 2011) 112001. [doi:10.1103/PhysRevLett.106.112001].

[138] CMS Collaboration, *"Measurement of the B^0 Production Cross Section in pp Collisions at $\sqrt{s} = 7$* TeV*"*, *Phys. Rev. Lett.* **106** (Jun, 2011) 252001. [doi:10.1103/PhysRevLett.106.252001].

[139] CMS Collaboration, *Measurement of the B_s^0 Production Cross Section with $B_s^0 \to J/\psi\phi$ Decays in pp Collisions at $\sqrt{s}$=7* TeV, *Phys. Rev. D* **84** (Sep, 2011) 052008. [doi:10.1103/PhysRevD.84.052008].

[140] CMS Collaboration, *"Commissioning of b-jet identification with pp collisions at $\sqrt(s) = 7$ TeV"*. CMS PAS BTV-10-001, [https://cdsweb.cern.ch/record/1279144].

[141] CMS Collaboration, *"Measurement of the Inclusive Jet Cross Section in pp Collisions at $\sqrt{s} = 7$ TeV"*, *Phys. Rev. Lett.* **107** (Sep, 2011) 132001. [doi:10.1103/PhysRevLett.107.132001].

[142] J. Alwall, P. Demin, S. de Visscher, R. Frederix, M. Herquet, F. Maltoni, T. Plehn, D. L. Rainwater, and T. Stelzer, *"MadGraph/MadEvent v4: the new web generation"*, *Journal of High Energy Physics* **2007** (2007), no. 09 028. [doi:10.1088/1126-6708/2007/09/028].

[143] H. e. a. Jung, *"The CCFM Monte Carlo generator CASCADE Version 2.2.03"*, *The European Physical Journal C - Particles and Fields* **70** (2010) 1237–1249. [doi:10.1140/epjc/s10052-010-1507-z].

[144] A. Banfi, G. Salam, and G. Zanderighi, *"Infrared-safe definition of jet flavour"*, *The European Physical Journal C - Particles and Fields* **47** (2006) 113–124. [doi:10.1140/epjc/s2006-02552-4].

[145] A. Banfi, G. Salam, and G. Zanderighi, *"Infrared-safe definition of jet flavour"*, *The European Physical Journal C - Particles and Fields* **47** (2006) 113–124. [doi:10.1140/epjc/s2006-02552-4].

[146] S. A. *etal*, *"Geant4 – a simulation toolkit"*, *Nuclear Instruments and Methods in Physics Research Section A: Accelerators, Spectrometers, Detectors and Associated Equipment* **506** (2003), no. 3 250–303. [doi:10.1016/S0168-9002(03)01368-8].

[147] Belle Collaboration, *"Charm hadrons from fragmentation and B decays in e^+e^- annihilation at $\sqrt{s} = 10.6$ GeV"*, *Phys. Rev. D* **73** (Feb, 2006) 032002. [doi:10.1103/PhysRevD.73.032002].

[148] CLEO Collaboration, *"Charm meson spectra in e^+e^- annihilation at 10.5 GeV center of mass energy"*, *Phys. Rev. D* **70** (Dec, 2004) 112001. [doi:10.1103/PhysRevD.70.112001].

[149] G. Abbiendi et al., *"Measurement of the production rate of charm quark pairs from gluons in hadronic Z^0 decays"*, *The European Physical Journal C - Particles and Fields* **13** (2000) 1–13. [doi:10.1007/s100520000260].

[150] R. B. et al, *"A measurement of the gluon splitting rate into $b\bar{b}$ pairs in hadronic Z decays"*, *Physics Letters B* **434** (1998), no. 3-4 437–450. [doi:10.1016/S0370-2693(98)00850-8].

[151] P. A. et al, *"Measurement of the multiplicity of gluons splitting to bottom quark pairs in hadronic Z0 decays"*, *Physics Letters B* **405** (1997), no. 1-2 202–214. [doi:10.1016/S0370-2693(97)00608-4].

[152] CMS Collaboration, *"Absolute luminosity normalization"*. CMS DP-2011-002, [https://cdsweb.cern.ch/record/1335668].

[153] A. Martin, W. Stirling, R. Thorne, and G. Watt, *"Parton distributions for the LHC"*, *The European Physical Journal C - Particles and Fields* **63** (2009) 189–285. [doi:10.1140/epjc/s10052-009-1072-5].

[154] CMS Collaboration, *"Inclusive total and differential production cross section of J/ψ and b-hadron production in pp collisions at $\sqrt{s} = 7$ TeV with the CMS experiment"*. CMS AN 2010-138.

[155] M. Oreglia, *"A study of the reactions psi-prime to gamma gamma psi"*. PhD thesis, Stanford University, 1980. SLAC-0236, [http://www.slac.stanford.edu/pubs/slacreports/slac-r-236.html].

[156] B. Mangano, *"CMS track reconstruction performance and latest results with cosmic muons."*, *PoS* **VERTEX 2008** (Dec, 2008) 015. [http://cdsweb.cern.ch/record/1167885/].

Acknowledgements

I would like to thank all the people who gave their contribution to the work I reported. They deserve a public acknowledgment, besides the private ones I have already made or planned, whether they revised my progress, showed me their interest on the subject, pointed me to the right source, shared the easiest and hardest times in all the places I have been during my graduate school, helped me with technicalities, sent me useful information or documents, provided friendship, made me laugh at the right time or just dropped by and said "hello". Thank you, everyone ...

Padova, February 2012